

**CHANNEL ESTIMATION FOR OFDM
SYSTEMS WITH TRANSMITTER DIVERSITY**

Igor A. Tolochko

Doctor of Philosophy

2005

Channel Estimation for OFDM
Systems with Transmitter Diversity

by
Igor A. Tolochko

Doctor of Philosophy

Centre for Telecommunications and Micro-Electronics



August 2005

DECLARATION

I, Igor A. Tolochko, hereby declare that this thesis contains no material, which has been accepted for the award of any other degree or diploma in any university. Further to the best of my knowledge and belief, this thesis contains no material previously published or written by another person except where due reference is made in the text of the thesis.

Igor A. Tolochko _____ 21st August 2005

Contents

Abstract	ix
Acknowledgements	xi
Author's Publications	xiii
Abbreviations	xv
List of Figures	xvii
List of Tables	xxi
Mathematical Notations	xxiii
1 Introduction	1
1.1 Motivations for the Research	2
1.2 Organization of the Thesis	3
1.3 Contributions of the Research	4
2 OFDM and Transmitter Diversity	7
2.1 Discrete-Time OFDM	8
2.1.1 Discrete-Time Model	8
2.1.2 Dispersive Wireless Channels	11
2.1.3 Detection Methods	14
2.1.4 OFDM-based WLANs	15
2.2 Time and Frequency Domain Correlation	16
2.2.1 Indoor Wireless Channel Models	17
2.2.2 Time Domain Correlation	17

2.2.3	Frequency Domain Correlation	18
2.2.4	Correlation Properties in HIPERLAN/2 Channels	19
2.3	Transmitter Diversity in OFDM-based WLANs	21
2.3.1	OFDM WLANs and Transmitter Diversity	21
2.3.2	Pilot Symbol Structures	23
2.4	Summary	25
3	Estimation of Channel Statistics in MISO OFDM	27
3.1	Coarse Channel Estimation	27
3.2	SNR Estimation	30
3.2.1	SNR Estimation Methods in MISO OFDM	30
3.2.2	Numerical Results	35
3.3	Maximum Excess Delay Estimation	39
3.3.1	Estimation Method in MISO OFDM	39
3.3.2	Numerical Results	40
3.4	R.M.S. Delay Spread Estimation	43
3.4.1	Estimation Method in MISO OFDM	43
3.4.2	Numerical Results	44
3.4.3	Alternative Techniques for Delay Spread Estimation	45
3.5	Summary	46
4	Channel Estimation in WLANs with Transmitter Diversity	47
4.1	Temporal Approach	48
4.1.1	Full Complexity Algorithm	48
4.1.2	Reduced Complexity Algorithm	50
4.2	Frequency Domain Approach	52
4.3	Comparison of the Channel Estimation Methods	54
4.3.1	Leakage Problem	54
4.3.2	Null Subcarriers	57
4.3.3	Complexity Analysis	58
4.4	Numerical Results	59
4.5	Summary	63

5	LMMSE Channel Estimation in WLANs with Transmitter Diversity	65
5.1	Real Time LMMSE Channel Estimation	66
5.1.1	Processing Model	66
5.1.2	An MSE Goal	67
5.1.3	Numerical Results	68
5.2	LMMSE Channel Estimation in MISO WLANs	78
5.2.1	Low-Rank Approximations	79
5.2.2	Complexity Analysis	81
5.2.3	Numerical Results	83
5.3	Summary	88
6	Sparse Approximations of the LMMSE Channel Estimation	91
6.1	Introduction	91
6.2	Sparse Approximations of the Fixed Weighting Matrix	92
6.2.1	LMMSE by SWC Channel Estimation	92
6.2.2	LMMSE by SWC Complexity	94
6.2.3	MSE Mismatch	94
6.3	Numerical Results	95
6.4	Summary	99
7	Low Complexity LMMSE Channel Estimation	101
7.1	Introduction	101
7.2	Low Complexity LMMSE Channel Estimation	102
7.2.1	Approximating the Exponential Power Delay Profile as Uniform	103
7.2.2	Sparse Approximations	107
7.3	Numerical Results	108
7.4	Summary	112
8	Conclusions	113
8.1	Thesis Summary	113
8.2	Future Work	115
	Bibliography	117

Abstract

Orthogonal Frequency-Division Multiplexing (OFDM) is now regarded as a feasible alternative to the conventional single carrier modulation techniques for high data rate communication systems, mainly because of its inherent equalisation simplicity. Transmitter diversity can effectively combat multipath channel impairments due to the dispersive wireless channel that can cause deep fades in some subchannels. The combination of the two techniques, OFDM and transmitter diversity, can further enhance the data rates in a frequency-selective fading environment. However, this enhancement requires accurate and computationally efficient channel state information when coherent detection is involved. A good choice for high accuracy channel estimation is the linear minimum mean-squared error (LMMSE) technique, but it requires a large number of processing operations. In this thesis, a deep and thorough study is carried out, based on the mathematical analysis and simulations in MATLAB, to find new and effective channel estimation methods for OFDM in a transmit diversity environment. As a result, three novel LMMSE based channel estimation algorithms are evaluated: real time LMMSE, LMMSE by significant weight catching (SWC) and low complexity LMMSE with power delay profile approximation as uniform. The new techniques and their combinations can significantly reduce the full LMMSE processor complexity, by 50% or more, when the estimation accuracy loss remains within 1 – 2 dB over a wide range of channel delay spreads and signal-to-noise ratios (SNR). To further enhance the channel estimator performance, pilot symbol structures are investigated and methods for statistical parameter estimation in real time are also presented.

Acknowledgements

I am sincerely indebted to my project supervisor, Prof. Mike Faulkner, for his continuous guidance, valuable advice, immense effort, and hours and hours of thoughtful discussions throughout my research at Victoria University.

During my research project, I have had the opportunity to work with and learn from a number of people to whom I would like to express my appreciation. These are Dr. Peter Olanders and Prof. Svante Signell, who introduced me to various aspects of multiple-input multiple-output systems during my employment at Ericsson Radio Systems AB, Sweden.

I would like to thank Ericsson Australia for its continuous support of this project during my employment with the company. I am also grateful to Mr. Andras Toth, Ericsson AB, Sweden, for his effort and support of my research.

I thank my colleagues for their help and cooperation. My deep appreciation to all administrative and technical staff at Victoria University for their support.

I would like to acknowledge Victoria University, the Government of Australia and the Australian Telecommunications Cooperative Research Centre for offering me scholarships, without which completion of this research would not have been viable.

Finally, I am deeply grateful to my wife Olga and my son Oleg for their continuous support and patience throughout this very time-consuming project.

Author's Publications

To a large extent of this research project has been published or has been submitted for publication. The detailed list is presented below. Publications, which are not directly reflecting the contents of this thesis, have also been included in the list.

- A. I. Tolochko and M. Faulkner, "Channel Estimation in Wireless LANs with Transmitter Diversity", *J. Wireless Pers. Commun.*, 31(1-2), pp. 63 – 75, 2004.
- B. I. Tolochko and M. Faulkner, "Sparse Approximations of the LMMSE Channel Estimation in OFDM with Transmitter Diversity", *J. Wireless Pers. Commun.*, Under the 2nd revision.
- C. I. Tolochko and M. Faulkner, "Real Time LMMSE Channel Estimation for Wireless OFDM Systems with Transmitter Diversity", In Proc. *IEEE 56th Vehicular Technology Conference*, Vancouver, Canada, pp. 1555 – 1559, Sept. 2002.
- D. I. Tolochko and M. Faulkner, "Channel Estimation Algorithm Analysis in Wireless LANs with Transmitter Diversity", in *Australian Telecommunications Networks and Applications Conference*, Melbourne, Australia, Dec. 2003.
- E. I. Tolochko, M. Pereira and M. Faulkner, "SNR Estimation in Wireless LANs with Transmitter Diversity", in the *3rd ATcerc Telecommunications and Networking Conference*, Melbourne, Australia, Dec. 2003.
- F. I. Tolochko and M. Faulkner, "Low Complexity LMMSE Channel Estimation in OFDM Systems with Transmitter Diversity", In preparation.

- G. K. Wang, M. Faulkner, J. Singh and I. Tolochko, "Timing Synchronisation for 802.11a WLANs under Multipath Channels", in *Australian Telecommunications Networks and Applications Conference*, Melbourne, Australia, Dec. 2003.
- H. K. Wang, M. Faulkner, J. Singh and I. Tolochko, "A Synchronization Scheme for OFDM-WLANs", in the *3rd ATcrC Telecommunications and Networking Conference*, Melbourne, Australia, Dec. 2003.

Selected parts from the listed above publications have also been included in the following items:

- I. M. Faulkner and I. Tolochko, "Channel Estimation for OFDM Systems", patent application No. 80786231/004579922, filed with Freehills, IP Australia, Dec. 2003.
- J. I. Tolochko and M. Faulkner, "Low Overhead Pilot Structures", Doc.: IEEE 802.11-04-0020-00-000n, submission to 802.11 TGn (standardization committee for Wireless LANs), Jan. 2004.

Abbreviations

AGC	automatic gain control;
AoA	angle-of-arrival;
AoD	angle-of-departure;
AS	angular spread;
BER	bit-error-rate;
BPSK	binary phase shift keying;
CFR	channel frequency response;
CIR	channel impulse response;
CP	cyclic prefix;
DAB	digital audio broadcasting;
DFT	discrete Fourier transform;
DMT	discrete multitone;
DVB	digital video broadcasting;
FFT	fast Fourier transform;
HT	hilly terrain;
ICI	inter-carrier interference;
IDFT	inverse DFT;
IFFT	inverse FFT;
i.i.d.	independent identically distributed;
ISI	inter-symbol interference;
LOS	line-of-sight;
LS	least-squares;
LMMSE	linear minimum mean-square error;

LMMSE/SU	LMMSE with shifted uniform approximation;
LMMSE/U	LMMSE with uniform approximation;
LUT	look-up-table;
MCM	multi-carrier modulation;
MSE	mean square error;
MIMO	multiple-input multiple-output;
MISO	multiple-input single-output;
NLOS	non-line-of-sight;
OFDM	orthogonal frequency-division multiplexing;
PSK	phase shift keying;
P/S	parallel to serial;
QAM	quadrature amplitude modulation;
r.m.s.	root-mean square;
SISO	single-input single-output;
SNR	signal-to-noise ratio;
S/P	serial to parallel;
STC	space-time coding;
SVD	singular value decomposition;
SWC	significant weight catching;
TU	typical urban;
WLANs	wireless local area networks;
WSS	wide-sense stationary.

List of Figures

2.1	Discrete-Time SISO OFDM model.	8
2.2	The leakage of a unity gain path zero due to non-sample spaced channel, $K = 64$	12
2.3	OFDM packet structure in the IEEE 802.11a WLAN.	15
2.4	Frequency domain correlation in 802.11a for HIPERLAN/2 channels.	20
2.5	MISO OFDM Discrete-Time Model.	21
2.6	A time orthogonal long sequence in MISO OFDM.	23
2.7	Frequency orthogonal long sequences in MISO OFDM.	24
3.1	Generalised block diagram of the MISO OFDM receiver using a Bayesian type channel estimator with interleaved subcarriers in the frequency domain.	30
3.2	DFT-based noise variance estimation in MISO OFDM using non-repeated pilot symbols interleaved in the frequency domain.	32
3.3	Observed CIR of HIPERLAN/2 channel A in a 2×1 scheme using one interleaved pilot symbol in the frequency domain: (a) a noiseless random realisation; (b) a cyclic shift of the CIR for $\beta = 2$ samples.	34
3.4	Coarse noise variance estimation in a 2×1 OFDM for sample-spaced 2-ray channel and HIPERLAN/2 channel A.	36
3.5	Coarse noise variance estimation in a 2×1 OFDM for HIPERLAN/2 channel C.	38
3.6	Maximum excess delay estimation for channel A (actual $\tau_x = 390$ ns or 7.8 samples) in a 2×1 MISO OFDM.	41
3.7	Maximum excess delay estimation for channel C (actual $\tau_x = 1050$ ns or 21 samples) in a 2×1 MISO OFDM.	42

3.8	R.M.S. delay spread estimation for channel A (actual $\tau_{rms} = 50$ ns or 1 sample) in a 2×1 MISO OFDM.	44
3.9	R.M.S. delay spread estimation for channel C (actual $\tau_x = 150$ ns or 3 samples) in a 2×1 MISO OFDM.	45
4.1	Significant tap catching technique in 64-subcarrier OFDM: (a) observed CIR of noiseless HIPERLAN/2 channel A; (b) 5 significant taps out the first L_0	50
4.2	The leakage of a unity gain path zero due to non-sample spaced channel, $K = 64$ and $\beta = 4$	52
4.3	MSE vs CIR window size for a 2-ray channel in 64-subcarrier OFDM.	56
4.4	MSE performance of three channel estimation algorithms in HIPERLAN/2 channel A.	61
4.5	MSE performance of three channel estimation algorithms in HIPERLAN/2 channel C.	62
4.6	MSE performance of three channel estimation algorithms in a sample-spaced equal power 2-ray channel with $\tau_{rms} = 50$ ns.	63
5.1	A simplified model for a real time LMMSE channel estimation in MISO OFDM.	66
5.2	MSE degradation of data due to channel estimation error.	68
5.3	Effect of τ_{rms} selection on channel estimation error in HIPERLAN/2 channel A ($\tau_{rms} = 50$ ns) with 2×1 diversity scheme.	69
5.4	Effect of τ_{rms} selection on channel estimation error in HIPERLAN/2 channel C ($\tau_{rms} = 150$ ns) with 2×1 diversity scheme.	70
5.5	Effect of SNR selection on channel estimation error in HIPERLAN/2 channel A ($\tau_{rms} = 50$ ns) with 2×1 diversity scheme.	71
5.6	Effect of SNR selection on channel estimation error in HIPERLAN/2 channel C ($\tau_{rms} = 150$ ns) with 2×1 diversity scheme.	72
5.7	Effect of interpolation errors in channel A at SNR = 40 dB.	73
5.8	Effect of interpolation errors in channel C at SNR = 40 dB.	74
5.9	Real time LMMSE channel estimator.	75

5.10	Real time LMMSE processor performance in a 2×1 802.11a for channels A, B and C. Perfect knowledge for SNR and τ_{rms} is assumed.	76
5.11	Real time LMMSE processor performance in a 2×1 802.11a for channels A, B and C. Measured threshold levels for SNR and τ_{rms}	77
5.12	2×1 Alamouti STC OFDM.	77
5.13	BER for a 2×1 Alamouti STC in channel B.	78
5.14	Relative channel power $\Sigma(k)/E\{ H(k) ^2\}$ of the singular value coefficients in an OFDM system with $K = 64$ and $L = 32$ for various τ_{rms}	81
5.15	LMMSE channel estimation MSE in a 4×1 diversity scheme for HIPERLAN/2 channel B ($\tau_{rms} = 100$ ns, $\tau_x = 730$ ns).	84
5.16	LMMSE channel estimation MSE in a 4×1 diversity scheme for HIPERLAN/2 channel C ($\tau_{rms} = 150$ ns, $\tau_x = 1050$ ns).	85
5.17	Low rank- \mathbb{R} and LMMSE channel estimation MSE of the <i>modified-1</i> scheme in a 2×1 diversity system for channels A ($\tau_{rms} = 50$ ns, $\tau_x = 390$ ns) and B ($\tau_{rms} = 100$ ns, $\tau_x = 730$ ns).	87
6.1	Normalized weight energy of arbitrary chosen rows from the LMMSE fixed weighting matrix generated for 64-subcarrier OFDM.	93
6.2	MSE performance of the sparse approximations at SNR = 20 dB for a different number of complex multiplications: (a) in a 2×1 scheme in channels A, B and C; (b) in a $Q \times 1$ scheme in channel B.	97
6.3	LMMSE and the sparse approximations for channel B: (a) MSE performance in a 2×1 scheme; (b) BER performance in a 2×1 Alamouti scheme for BPSK.	98
6.4	Real time LMMSE by SWC for a 2×1 802.11a in channel B.	99
7.1	Frequency domain correlation in 802.11a using the uniform power delay profile.	104
7.2	Observed CIR of HIPERLAN/2 channel C obtained by means of a 64-subcarrier IFFT: (a) a random noiseless realization; (b) the CIR positioned symmetrically around the time origin using a cyclic shift of $L_0/2 = 11$	105

7.3	Flowchat of the LMMSE channel estimation with the shifted uniform power delay profile approximation.	107
7.4	A modified block diagram of the MISO receiver using the shifted uniform power delay profile approximation.	108
7.5	The MSE performance of the four different LMMSE processing methods in a 2×1 scheme for channels A and C.	109
7.6	The MSE and BER performances of the LMMSE, LMMSE/SU and LMMSE by SWC in a 2×1 scheme for channel B.	110
7.7	The MSE performance of the SWC technique applied to LMMSE and LMMSE/SU for a different number of required real multiplications at SNR = 20 dB: (a) in a 2×1 scheme for channels A and C; (b) in a $Q \times 1$ scheme for channel B.	111

List of Tables

2.1	Physical layer parameters for OFDM-based WLANs	16
2.2	HIPERLAN/2 Channel Models	17
4.1	Channel Estimation Complexity for a 2×1 Diversity Scheme	58
5.1	Switching Parameters	74
5.2	LMMSE Complexity in MISO OFDM for one Transmit Antenna . . .	82
5.3	Maximum SNR Range for the LMMSE with 802.11a Pilot Symbol Overhead	86
5.4	Maximum SNR Range for the LMMSE with Pilot Symbol Overhead of $16 \mu s$	86

Mathematical Notations

A	constant;
A_j	antenna j ;
α_m	complex gain of the m th path;
α_μ	complex gain of the μ th path;
$\arg \max\{\cdot\}$	argument that maximises;
b	integer;
β	CP window extension operator;
C	speed of light;
$\mathbb{C}(\cdot)$	cost function;
$(\cdot)^*$	complex conjugate;
$\text{diag}(\cdot)$	diagonal matrix;
$\delta(\cdot)$	Dirac delta function;
Δf	subcarrier spacing;
e	interference term due to ISI and ICI;
E	energy;
E_b	energy per bit;
$E\{\cdot\}$	expectation;
$(\cdot)_e$	exponential power delay profile;
$(\cdot)^H$	Hermitian transpose;
η	interference power due to ISI and ICI;
η_μ	interference power due to μ th path;
f	continuous frequency;
f_s	sampling frequency;

$\mathbf{F}[\cdot]$	Fourier matrix;
$\mathfrak{F}(\cdot)$	Fourier transform;
f_c	carrier frequency;
f_D	maximum Doppler frequency;
g_m	m th sample-spaced tap;
Γ	number of strongest weights from \mathbf{W} ;
γ	varying column number corresponding to \mathbf{w} ;
h	channel impulse response;
\mathbf{h}	noiseless CIR vector;
$\tilde{\mathbf{h}}$	stacked vector of CIR estimates;
\tilde{h}	channel impulse response estimation;
H	channel frequency response;
\mathbf{H}	true with no mismatch frequency domain attenuation vector;
\mathbb{H}	intermediate channel estimation vector using LMMSE by SVD;
\check{H}	rotated \hat{H} through a phase shift;
$\hat{\mathbf{H}}$	fine estimation vector of vector \mathbf{H} ;
$\tilde{\mathbf{H}}$	LS estimation vector in SISO OFDM;
H_μ	DFT of the observed CIR tail taps;
i	discrete-time instant;
i'	time domain correlation matrix row number;
\mathbf{I}	identity matrix;
j	transmit antenna number;
$(\cdot)_j$	transmit antenna j ;
j'	transmit antenna number;
$J_0(\cdot)$	the zeroth order Bessel function;
K	number of subcarriers;
k	subcarrier number;
k'	frequency domain correlation matrix row number;
κ	subcarrier number used in the reduced complexity temporal channel estimation;
L	CP length;
l	discrete-time sample;

L_0	discrete-time delay of the power delay profile;
M	actual number of CIR taps;
M'	number of taps within the CP length;
m	CIR tap number;
$\max(\cdot)$	function that maximises;
μ	tail tap number outside the CP length;
n	channel noise;
\mathbf{n}	noise vector;
N_{cm}	number of complex multipliers;
N_0	noise variance;
\hat{N}_0	estimation of noise variance;
\bar{P}	LS estimation at one subcarrier of a single OFDM pilot symbol;
$\bar{\mathbf{P}}$	LS estimation vector of a single OFDM pilot symbol;
\bar{p}'	CIR tap after the windowing;
$\bar{\mathbf{p}}'$	CIR vector after the windowing;
\bar{P}'	CFR tap after filtering by the CIR windowing;
$\bar{\mathbf{P}}'$	CFR vector after filtering by the CIR windowing;
\check{P}	rotated \bar{P} through a phase shift;
$\tilde{\mathbf{P}}$	LS estimation vector of two repeated OFDM pilot symbols;
Ψ	auto-covariance matrix of the estimation error;
ψ	channel estimation error vector;
Q	transmit diversity order;
\mathbf{Q}	correlation matrix for temporal channel estimation;
r	frequency domain correlation coefficient;
\mathbf{R}	frequency domain correlation matrix;
\mathbb{R}	rank of matrix;
r_H	channel correlation function;
r_t	time domain correlation coefficient;
ρ	multipath power threshold level;
s	variable used in the reduced complexity temporal channel estimation;

S	number of independent pilot symbols, each preceded with a CP;
SNR	SNR value used for the LMMSE smoothing matrix calculation;
\widetilde{SNR}	true with no mismatch SNR;
ΔSNR	mismatch SNR parameter;
$(\cdot)_s$	shifted uniform power delay profile;
σ_x^2	variance of data symbols;
Σ	diagonal matrix with the singular values;
$\text{sinc}(\cdot)$	sinc function, $\frac{\sin(x)}{x}$;
t	continuous time;
T_f	OFDM symbol time interval;
T_s	sampling rate;
τ	channel multipath delay;
τ_m	delay for the m th path;
τ_{rms}	r.m.s. delay spread;
$\hat{\tau}_{rms}$	r.m.s. delay spread estimation;
$\tilde{\tau}_{rms}$	true with no mismatch r.m.s. delay spread;
$\Delta\tau_{rms}$	mismatch r.m.s. delay spread parameter;
τ_x	maximum excess delay of the channel power delay profile;
$\hat{\tau}_x$	maximum excess delay of the channel power delay profile estimation;
θ	power delay profile;
$\text{trace}[\cdot]$	trace of matrix;
u	variable used in the reduced complexity temporal channel estimation;
\mathbf{U}	unitary matrix;
$(\cdot)_u$	uniform power delay profile;
v	mobile terminal speed;
\mathbf{V}	unitary matrix;
w	weight from the fixed weighting matrix, \mathbf{W} ;
\mathbf{w}	row vector of \mathbf{W} ;
\mathbf{W}	fixed weighting matrix;
\mathbf{W}^1	matrix with the first set of coefficients for \mathbf{W} approximated by SVD;
\mathbf{W}^2	matrix with the second set of coefficients for \mathbf{W} approximated by SVD;

W_K	DFT operator, $\exp(-j2\pi/K)$;
x	data or pilot symbol;
\mathbf{x}	data or pilot symbol vector;
\mathbf{X}	diagonal matrix containing the transmitted pilot points, $x(k)$;
\hat{x}	estimation of data or pilot symbol;
y	OFDM demodulator output data;
\mathbf{y}	OFDM demodulator output data vector;
$\tilde{\mathbf{y}}$	averaged received vector;
\mathbf{z}	correlation vector used in temporal channel estimation;
\approx	approximately equal;
\cup	union;
\in	belong to;
$ \cdot $	magnitude of a scalar;
\triangleq	equal by definition;
$(\cdot \cdot)$	conditioning for probabilities.

Chapter 1

Introduction

The main goals in developing the next generation of wireless communication systems are for delivering multimedia services such as voice, data and image in local coverage networks. These will be a complement to the existing wide area coverage systems, for example to the third generation of mobile communications. In order to provide these services, a high data rate and high quality digital communication system is required in a restricted bandwidth. A major limiting factor is, however, the multipath propagation phenomenon. It causes frequency-selective fading due to different echoes of transmitted symbols overlapping at the receiving end, which can lead to the bit-error-rate (BER) degradation. One way to effectively combat the multipath channel impairments and still provide high-data rates in a limited bandwidth is use of an orthogonal frequency-division multiplexing (OFDM) modulation method and multiple antennas at the transmitting end.

OFDM is an attractive multi-carrier modulation (MCM) technique because of its high spectral efficiency and simple single-tap equaliser structure, as it splits the entire bandwidth into a number of overlapping narrow band subchannels requiring lower symbol rates. Furthermore, the inter-symbol interference (ISI) and inter-carrier interference (ICI) can be easily eliminated by inserting a cyclic prefix (CP) in front of each transmitted OFDM block. OFDM can be implemented using a coherent or non-coherent detection technique. A coherent detection method generally provides the SNR gain over the non-coherent method as the former modulation technique uses channel state information. This implies, however, a more complex receiver as the channel state information is generally obtained using channel esti-

mation.

Transmitter diversity can effectively combat multipath channel impairments due to the dispersive wireless channel that can cause deep fades in some subchannels. This is generally achieved by separating transmit antennas far enough so that to make zero or very low correlation between the transmission paths. The combination of the two techniques, OFDM and transmitter diversity, can further enhance the data rates in a frequency-selective fading environment. However, this enhancement requires accurate and computationally efficient channel estimation methods.

1.1 Motivations for the Research

Channel state information in coherent OFDM-based wireless communication systems can be obtained by sending pilot symbols from the transmitter to the receiver. By introducing transmit diversity, the required pilot symbol overhead can cause a significant signalling overhead and therefore a capacity loss in the system. One possible way of this signalling reduction is to simply transmit pilot symbols on the interleaved subcarriers in the frequency domain. At the receiving end, the channel estimator can identify the channel characteristics in the non-measured subchannels by interpolating the different subsets of measured subchannels from the specified antenna. This approach introduces, however, an evident interpolation error in a dispersive wireless channel, which can degrade the channel estimation accuracy, especially if the number of used transmit antennas is large. The linear minimum mean-squared error (LMMSE) estimator, which takes advantage of the correlation between subcarriers, can significantly improve the estimator accuracy, but it requires a large number of processing operations. In addition, the complexity of the LMMSE forces practical systems to preprocess the fixed weighting matrix using a single set of expected values for signal-to-noise ratio (SNR) and root-mean square (r.m.s.) delay spread (the latter variable is only used for channels with an exponentially decaying power delay profile). This can cause estimator performance loss in a different multipath channel environment.

The above concerns are addressed in this thesis. The motivation for the research work is to develop high accuracy, low complexity and low pilot symbol overhead

channel estimation algorithms for OFDM systems with transmitter diversity.

1.2 Organization of the Thesis

Chapter 2 introduces the discrete-time OFDM system using coherent detection. Basic OFDM parameters are presented and specifically the channel estimation problem is stated. Further, impairments of the ISI and ICI due to a fading multipath channel are covered. Particularly, the non-sample spaced channel problem is outlined using indoor channel models, and channel estimation degradation due to the leakage of the observed channel impulse response (CIR) is discussed. Time and frequency domain correlation is presented for modern OFDM-based wireless local area networks (WLANs) and the channel estimation problem in a transmit diversity environment is also introduced. Finally, the advantages and disadvantages for a number of different pilot symbol structures are discussed within the 802.11a framework.

Chapter 3 presents the estimation of channel statistics for OFDM systems with transmit diversity in an indoor, rich scattering channel environment. Specifically, the coarse channel estimation is analysed for various pilot symbol structures. Techniques for the parameter estimation are evaluated in the presence of the CIR power leakage and null-guard tones presence (that are generally used in OFDM-based WLANs). Numerical results are also presented.

Chapter 4 compares three channel estimation algorithms in WLANs with transmit diversity. Two algorithms use a temporal approach (often called discrete Fourier transform (DFT) based) for channel estimation and the third algorithm uses a frequency domain approach. The algorithms are analysed in an indoor rich scattering HIPERLAN/2 channels. The impact of CIR power leakage and null-guard tones presence on channel estimation accuracy is thoroughly investigated for the three channel estimation techniques. A mathematical analysis and numerical results are presented.

Chapter 5 introduces an enhanced LMMSE channel estimation algorithm for WLANs with transmitter diversity. Based on the initial parameter estimates that are obtained in real time, the evaluated algorithm can significantly improve the LMMSE channel estimation accuracy. The edge error problem is also highlighted

when interleaved subcarriers are used for channel estimation. Numerical results are presented.

Chapter 6 investigates two sparse approximation techniques for the LMMSE channel estimation in OFDM with transmit diversity. A well known technique, channel estimation by singular value decomposition (SVD), is analysed for various transmit diversities, r.m.s. delay spreads and SNRs. Due to limited performance of the optimal low rank approximation in channels with large delay spreads, a novel sparse approximation method is evaluated. This is accomplished by applying a significant weight catching (SWC) technique to the LMMSE fixed weighting matrix.

Chapter 7 describes a low complexity LMMSE channel estimation algorithm in a transmit diversity environment. A novel LMMSE channel estimation method reduces the complex fixed weighting matrix to all real values. This is accomplished by approximating a power delay profile, generally exponential in wireless channels, as uniform followed by positioning the CIR symmetrically around the time origin using a cyclic shift. Numerical results are presented.

Chapter 8 concludes the thesis and highlights possible future work. A combination of the real time LMMSE, LMMSE with a power delay profile approximated as uniform and SWC technique can significantly reduce the computational complexity of the full LMMSE processor (by more than 75% in a 2×1 diversity scheme). Despite this, the estimation accuracy loss remains within 1 – 2 dB over a wide range of channel delay spreads and SNRs.

1.3 Contributions of the Research

The main contribution of this thesis is a deep and thorough study of channel estimation problems in OFDM systems with transmitter diversity. As a result, a number of novel LMMSE-based channel estimation algorithms and combinations are proposed. Another contribution of the thesis is an investigation into the pilot symbol structures of modern OFDM-based WLANs and their analysis in an indoor rich scattering channel environment. In addition, this thesis presents techniques for the estimation of channel statistics for OFDM systems in a transmit diversity environment. These contributions are summarised in detail below.

- * Chapter 3 develops various techniques for the SNR, maximum excess delay and r.m.s. delay spread of the power delay profile estimation in a transmit diversity environment, based on the coarse (least-squares (LS)) channel estimation. The mathematical expressions are derived and where necessary, the corresponding block diagrams are presented. The receiver can use the initial parameters to further improve, for example, a channel estimation quality.
- * Chapter 4 compares temporal and frequency domain channel estimation methods in a transmit diversity environment. It concludes that the temporal channel estimation technique performs worse than the frequency domain method, because of two limiting factors. These are the leakage problem in non-sample spaced channels, which causes energy loss with CIR windowing, and the null-guard tones (often used in WLANs), which can lead to an accuracy loss in the CIR measurement when DFT processing is involved. The frequency domain approach is inherently robust to these two effects since an additional transformation to the time domain is not necessary.
- * Chapter 5 proposes an enhanced channel estimation algorithm that obtains near LMMSE performance in a transmit diversity environment. This is achieved by selecting an appropriate set of the fixed weighting matrix coefficients pre-calculated in advance and stored in a number of look-up-tables (LUT). An appropriate LUT can be selected in real time to perform fine filtering of the initial LS observation. The selection criterion is based on SNR and r.m.s. delay spread of the power delay profile values that are obtained from the LS estimation. LMMSE channel estimation performance and complexity are also investigated for various transmit diversity orders. The bounds of the estimator's tolerable performance are also discussed.
- * Chapter 6 proposes a simplified LMMSE channel estimation algorithm in a transmit diversity environment by applying the SWC technique to the LMMSE fixed weighting matrix. The LMMSE by SWC can reduce the computational complexity of the full LMMSE processor by more than 50% and it outperforms the LMMSE by SVD over a wide range of channel delay spreads and SNRs. The MSE analysis for the LMMSE by SWC technique is presented. A tolerable

mismatch of the initial parameter estimates is also investigated for the 802.11a system in HIPERLAN/2 channels.

- * Chapter 7 proposes a low complexity LMMSE channel estimation algorithm that derives an all real valued fixed weighting matrix in OFDM systems with transmit diversity. This is accomplished by approximating a power delay profile, generally exponential in wireless channels, as uniform followed by positioning the CIR symmetrically around the time origin using a cyclic shift. The novel algorithm reduces computational complexity of the optimal LMMSE processor (using an exponential power delay profile) by 50% in terms of required multiplications, when the loss of estimation accuracy remains within 1 – 2 dB over a wide range of channel delay spreads and SNRs in a 2×1 diversity scheme. The mathematical expressions are derived and a flowchat of the algorithm is presented.

Chapter 2

OFDM and Transmitter Diversity

This chapter introduces OFDM in a single-input single-output (SISO) environment and its extension in a transmit diversity or multiple-input single-output (MISO) environment. OFDM is a high spectral efficiency type of MCM transmission system, where the available spectrum is divided into a number of narrow band subchannels [1]-[8]. This allows for individually modulating each subcarrier and then transmitting the entire OFDM blocks at a significantly lower rate than in a single-carrier system. OFDM parameters are generally chosen such that each subchannel experiences flat fading, because the bandwidth of the modulated subcarrier becomes narrow compared with the coherence bandwidth of the dispersive channel. To eliminate the multipath channel impairments, a simple single-tap equaliser is required to adjust distorted magnitude and phase in each subcarrier. The high spectral efficiency in OFDM is achieved by finding frequencies that are orthogonal, which means that they are perpendicular in a mathematical sense, allowing spectrum in each subchannel to overlap another without interfering with it. The orthogonality between the nearby subcarriers and the ISI between the consecutive OFDM symbols can be completely maintained by a CP.

OFDM was first presented in 1966 [9], but the concept for the MCM system goes back to the early 1950s [1]. In 1971 the discrete-time OFDM was introduced using an efficient fast Fourier transform (FFT) technique at both transmitter and receiver [10]. The ISI and ICI problems, due to a dispersive channel, were solved using the CP extension of the OFDM symbols in 1980 [11].

OFDM has many applications in wired and wireless environments today [4].

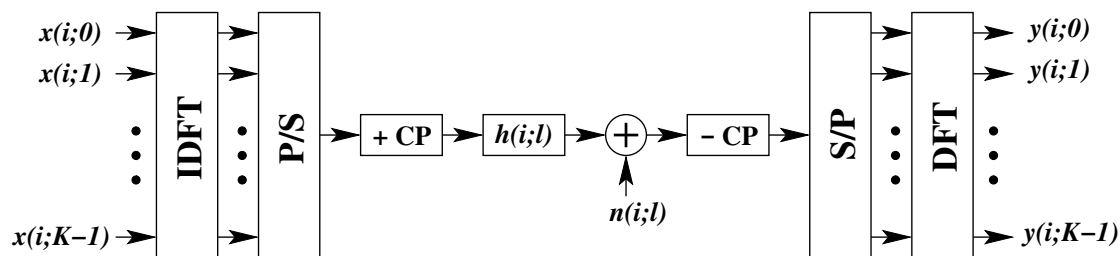


Figure 2.1: Discrete-Time SISO OFDM model.

These are discrete multitone (DMT) systems, digital audio broadcasting (DAB), digital video broadcasting (DVB) and WLANs. An extension to modern SISO WLANs introducing multiple antennas at both transmitter and receiver is also in its standardisation phase [12].

2.1 Discrete-Time OFDM

The first OFDM transceivers were implemented as continuous-time systems using a filter-bank implementation of the OFDM modem [5]. However, for a large number of subchannels the continuous-time concept becomes impractical in terms of cost and complexity. Suggested in 1971, the discrete-time implementation of the OFDM has replaced the modulation and demodulation by the inverse DFT (IDFT) and DFT respectively and since then the digital concept has been used in modern OFDM-based systems [10].

2.1.1 Discrete-Time Model

A block diagram for a discrete-time SISO OFDM model is presented in Fig. 2.1. The model can be partitioned into three subblocks: K -subcarrier OFDM modulator, physical channel and K -subcarrier OFDM demodulator.

- **OFDM modulator**

The data symbols, $x(i;k)$, at discrete-time instant i of an OFDM block are individually modulated on K subcarriers by the IDFT using some conventional types of phase shift keying (PSK) or quadrature amplitude modulation (QAM) constellation. After the IDFT transformation, the complex baseband OFDM signal in the time domain is given by

$$x(i; l) = \frac{1}{K} \sum_{k=0}^{K-1} x(i; k) e^{j2\pi kl/K}, \quad (2.1)$$

where l is the discrete-time sample and k denotes the subcarrier number out of $k = 0, 1, \dots, K - 1$.

Before sending the time domain OFDM symbol through the physical channel, the symbol is converted from parallel to serial (P/S) form and extended with a CP of length L (shown by the “+ CP” block in the figure). The CP extension is accomplished by inserting the last L samples of the OFDM symbol in front of it.

- **Channel**

The complex baseband multipath channel, at arbitrary time t , can be described by the M -tap CIR as follows [13]

$$h(t; \tau) = \sum_{m=0}^{M-1} \alpha_m(t) \delta(\tau - \tau_m), \quad (2.2)$$

where t represents the time variations of the channel due to motion and τ denotes the channel multipath delay at a fixed time instant, t . τ_m is the delay for the m th path, where $m = 0, 1, \dots, M - 1$. $\alpha_m(t)$ is the corresponding complex gain with a power delay profile, $\theta(\tau_m)$, and $\delta(\cdot)$ is the Dirac delta function. The path gains, $\alpha_m(t)$, are independent wide-sense stationary (WSS) narrowband complex Gaussian processes [14]. The power delay profile, $\theta(\tau_m)$, is generally modelled as exponential or uniform and will be discussed in the following sections.

From Equation 2.2, the channel frequency response (CFR) of the multipath channel at time t can be given by [15]

$$H(t; f) \triangleq \int_{-\infty}^{\infty} h(t; \tau) e^{-j2\pi f\tau} d\tau = \sum_{m=0}^{M-1} \alpha_m(t) e^{-j2\pi f\tau_m}, \quad (2.3)$$

where f is the continuous frequency.

For the CIR that is confined to the CP length and sample-spaced timing,

the discrete-time CFR at the k th tone of one OFDM block can be expressed as [16]

$$H(i; k) \triangleq H(iT_f; k\Delta f) = \sum_{l=0}^{L_0-1} h(i; l)W_K^{kl}, \quad (2.4)$$

where T_f and Δf are the OFDM symbol time interval and subcarrier spacing respectively. L_0 is the discrete-time delay of the power delay profile. $h(i; l) \triangleq h(iT_f, lT_s)$ is the discrete-time CIR, where $T_s = 1/(K\Delta f)$ is the sampling rate, and $W_K \triangleq \exp(-j2\pi/K)$.

The multipath channel is assumed to be slowly fading so that it remains constant over one OFDM symbol interval. In the packet type OFDM systems, such as IEEE 802.11a, the multipath channel can be considered constant even over the packet length, as the packet length is chosen short enough to make this assumption viable [4]. This simplifies the OFDM receiver complexity as the channel tracking in the time domain can be avoided.

The channel noise, $n(i; l)$, is assumed to be the independent identically distributed (i.i.d.), additive complex Gaussian with zero mean and variance N_0 .

- **OFDM demodulator**

After the CP is removed (shown by the “– CP” block in Fig. 2.1) in the demodulator, the received signal is converted from serial to parallel (S/P) form and then demodulated back to the frequency domain by the DFT. When the CIR is confined to the CP length and also when a perfect time and frequency synchronisation exists in the OFDM transceiver, the input-output description is given by

$$y(i; k) = H(i; k)x(i; k) + n(i; k), \quad (2.5)$$

where $n(i; k)$ is the additive complex Gaussian noise with zero mean and variance N_0 , given by the DFT of the time domain i.i.d. noise vector, $\mathbf{n}(i) = [n(i; 0), n(i; 1), \dots, n(i; K - 1)]$, of $n(i; l)$ terms [17].

2.1.2 Dispersive Wireless Channels

In the previous section, the multipath propagation was assumed to be a sample-spaced channel. Also, it was confined to the CP length. However, these two assumptions do not always exist in realistic situations, as it has been reported in literature. Both effects can cause OFDM performance degradation, such as BER performance loss due to the poor channel estimation quality. The channel estimation accuracy can become poor because of the non-sample spaced channels or the increased interference power due to the long echoes in the channels exceeding the CP length. These are summarized below.

- **Non-sample spaced channels**

Generally, the channel paths are non-sample spaced that causes energy smearing across the entire OFDM block [17]-[20]. This can result in poor channel estimation quality especially when using a temporal estimation method (often referred to as the DFT-based method).

The energy smearing can be described by the discrete-time CIR obtained via the IDFT transformation of the CFR, $H(t; f)$, defined by Equation (2.3). Then, the observed impulse response at sample l can be expressed by [17], [19]

$$h(l) = \sum_{m=0}^{M-1} \alpha_m g_m(l), \quad (2.6)$$

where $g_m(l)$ is given by

$$g_m(l) = \begin{cases} \delta(l - \tau_m), & \text{if } \tau_m \text{ is an integer;} \\ \frac{\sin(\pi(l - \tau_m))}{K \sin(\pi(l - \tau_m)/K)} e^{j(K-1)\pi(l - \tau_m)/K} & \text{otherwise.} \end{cases} \quad (2.7)$$

If delay τ_m is an integer, then all the energy from the multipath complex gain, α_m , is mapped to $g_m(l)$ tap. Otherwise, if τ_m is not an integer, its energy will leak to all taps. The latter is illustrated in Fig. 2.2 for a unity gain path zero, which is lying in delay interval ($0 < \tau_m < 1$).

After the inverse FFT (IFFT), the path energy becomes distributed over the sample-spaced taps $l = [0, 1, \dots, K - 1]$. Most of the energy is kept

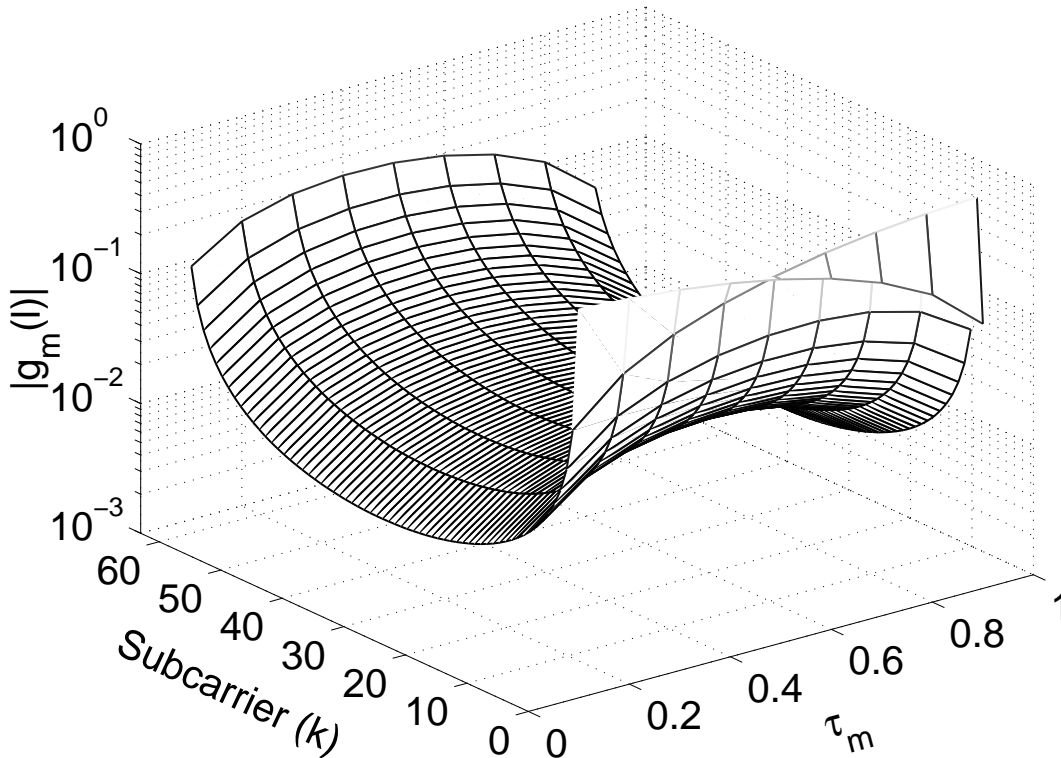


Figure 2.2: The leakage of a unity gain path zero due to non-sample spaced channel, $K = 64$.

in the neighbourhood of the original tap location. The energy smearing is maximum across all taps, when τ_m is right in the middle of the two adjacent sample-spaced taps.

- **Impairments due to the CIR exceeding the CP length**

OFDM is generally implemented using the CP extension. In practice, CP cannot be long enough for the complete elimination of interblock interference. When this occurs, additional sources of interference arise, caused by the ISI term from the preceding symbol and ICI term from the present symbol [21]-[27].

Each of these two terms can be modelled as an additional source of uncorrelated additive complex Gaussian noise, with zero mean and combined variance of the CIR taps that exceed the CP length [23], [24], [27].

Under this assumption, the complex baseband CIR of a wireless multipath channel, given by Equation (2.2) and can be written as [28]

$$h(t; \tau) = \sum_{m=0}^{M'-1} \alpha_m(t) \delta(\tau - \tau_m) + \sum_{\mu=M'}^{M-1} \alpha_\mu(t) \delta(\tau - \tau_\mu), \quad (2.8)$$

where M' denotes the number of channel taps that are within the CP lengths. μ is the tail tap number, out of the remaining, $(M - M')$, CIR samples that are outside the CP length.

For a unit variance symbol, $x(i; k)$, sent through a fading channel with the CIR power normalised to unity, the interference power due to ISI and ICI in the k th subcarrier, caused by the μ th path, can be given by the variance, $\eta_\mu(i; k)$, as follows [23]

$$\eta_\mu(i; k) = 2|\alpha_\mu(t)|^2. \quad (2.9)$$

Thus, the frequency domain input-output description of the received signal, $y(i; k)$, given by Equation (2.5), can be written as

$$y(i; k) = H(i; k)x(i; k) + n(i; k) + e(i; k), \quad (2.10)$$

where $e(i; k)$ is the interference term presented by the additive complex Gaussian noise with zero mean and variance of $\eta(i; k)$, given by

$$\eta(i; k) = \sum_{\mu=M'}^{M-1} \eta_\mu(i; k). \quad (2.11)$$

An alternative method to present the interference power, $\eta(i; k)$, has been evaluated in [27]. This method is based on the observations that the noise is predominantly affecting the low-frequency components in DMT systems. Accordingly, the ISI and ICI interference power, for the sample-spaced timing, is given by

$$\eta(i; k) = 2 \sum_{\mu=M'}^{M-1} |H_\mu(i; k)|^2, \quad (2.12)$$

where $H_\mu(i; k)$ is the DFT of the observed CIR tail taps, given by

$$H_{\mu}(i; k) = \sum_{\mu=M'}^{M-1} h(i; \mu) e^{-j2\pi\mu k/K}. \quad (2.13)$$

Generally, Equation (2.12) produces larger mean value of the estimated ISI and ICI error power than Equation (2.11), as a result of iterative accumulation of the interference component at lower frequency bins. In non-sample spaced channels, the noise variance estimation using Equation (2.12) can also be affected by the CIR smearing outside the CP length. The latter can cause further rising of the mean interference power.

The interference power causes an irreducible mean square error (MSE) floor for the OFDM data symbols and for channel estimation at high SNRs.

In the following, the interference power term will be modelled using Equation (2.11).

2.1.3 Detection Methods

In OFDM using PSK or QAM modulation, the phase and amplitude on each subcarrier are generally corrupted at the receiving end by frequency offset, imperfect time synchronisation and multipath channels. Two common techniques are widely used to demodulate these signals with distorted constellations: coherent and differential detection. Coherent demodulation requires knowledge of the transmitted carrier amplitude and phase, which can be obtained using channel estimation. This generally implies a more complex receiver. Differential detection requires no amplitude and no phase information in order to perform demodulation. Thus, the receiver can be much simpler and the pilot symbols can be omitted, at the price of a higher SNR, which has to be provided by greater transmission power [4], [29], [30].

Differential detection can be applied over the time domain, frequency domain or both. These imply, however, the use of differential encoding at the transmitting end. Time domain differential detection is mostly affected by the Doppler spread, especially in rapid dispersive fading channels. The performance of frequency domain differential detection mostly depends on the r.m.s. delay spread of the multipath channel power delay profile. Advanced topics on differential detection application in OFDM, such as coded modulation for noncoherent reception and two-dimensional

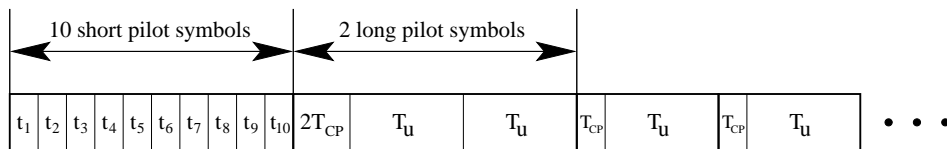


Figure 2.3: OFDM packet structure in the IEEE 802.11a WLAN.

demodulation, can be found for example in [31]-[34].

In general, the SNR after differential detection is approximately 3 dB worse than the input SNR [4]. The SNR performance loss due to non-coherent modulation makes the coherent detection more attractive and therefore a better choice for the modulation method in OFDM systems. In practice, coherent detection also has an SNR loss because of imperfect channel estimation and because a part of the signal power is spent on pilot symbols [4], [35]. These problems are addressed in the following chapters for OFDM-based WLANs using coherent detection and analysed in a transmit diversity environment.

2.1.4 OFDM-based WLANs

OFDM-based communication systems can be classified as continuous transmission systems, such as DAB [36] and DVB [37], and packet type communication systems, such as IEEE 802.11a [38] and ETSI BRAN HIPERLAN/2 [39]. The packet type systems have found their further extension in MIMO applications in recent years [12]. MIMO OFDM wireless links will provide high data rates in home and office environments, with peak rates up to 100 Mb/s [40].

IEEE 802.11a and HIPERLAN/2 can provide channel data rates up to 54 Mb/s (in a 20 MHz channel spacing) in the 5 GHz frequency band and they employ coherent detection [41]-[43]. The physical layer parameters for both standards are very similar and summarised in Table 2.1.

The OFDM data packet structure in the IEEE 802.11a WLAN is depicted in Fig. 2.3 [38].

Each data packet for transmission is preceded by a preamble that is used for synchronisation and channel estimation, Fig. 2.3. The preamble consists of 10 short and 2 long OFDM pilot symbols. The short symbols, t_i , are used for coarse time and frequency synchronisation. Two identical long pilot symbols, T_u , preceded by a double length CP, are used for fine synchronisation and channel estimation. The

Table 2.1: Physical layer parameters for OFDM-based WLANs

Parameter	Value
FFT size, K	64
Sampling rate, $f_s = 1/T_s$	20 MHz
Symbol part duration, T_u	$64T_s = 3.2 \mu s$
CP duration, T_{cp}	$16T_s = 0.8 \mu s$
Symbol interval, T_f	$T_{cp} + T_u = 4.0 \mu s$
Long training sequence CP duration, T_g	$2T_{cp} = 1.6 \mu s$
Long training sequence duration, T_{long}	$T_g + 2T_u = 8.0 \mu s$
Short training sequence duration, T_{short}	$10 \cdot 16T_s = 8.0 \mu s$
Total number of used subcarriers, K_{ts}	52
Subcarrier spacing, Δf	$1/T_u = 0.3125$ MHz
Used subcarriers, k	1, 2, ..., 26, 38, 39, ..., 63
Null-guard subcarriers, k	0, 27, 28, ..., 37

payload can vary from 1 to 4095 bytes and generally is chosen short enough to make the assumption that a multipath channel is constant during the time of the packet transmission [4]. This simplifies the receiver structure as the tracking of the packet in the time domain can be avoided.

Additionally, 12 subcarriers out of 64 available are set to zero, including zero frequency bin. The latter allows a direct conversion receiver structure implementation avoiding a direct current offset at the receiving end. The former 11 subcarriers are set to zero to meet the spectral channelisation requirement for the 802.11a system. These 12 subchannels are often called the null-guard subcarriers.

Further information on the 802.11a system can be found in [38].

2.2 Time and Frequency Domain Correlation

The OFDM modulation technique allows exploitation of both, the time and frequency domain correlations between the subchannels, which can be used to improve the channel estimation accuracy [44]. The time and frequency domain correlations are discussed in the following sections based on the physical layer parameters of IEEE 802.11a WLAN.

Table 2.2: HIPERLAN/2 Channel Models

Channel	r.m.s. delay spread	Max. excess delay	Environment
A	50 ns	390 ns	NLOS
B	100 ns	730 ns	NLOS
C	150 ns	1050 ns	NLOS
D	140 ns	1050 ns	LOS
E	250 ns	1760 ns	NLOS

2.2.1 Indoor Wireless Channel Models

WLANs have been deployed in a wide range of indoor environments, such as offices, industrial buildings, exhibition halls and homes [41]. Five channel models – A, B, C, D and E – have been specifically developed to represent this environmental diversity [45]. They are summarised in Table 2.2.

The channels are non-sample spaced with an exponentially decaying power delay profile. They are modelled as 18-tap delay lines in non-line-of-sight (NLOS) and line-of-sight (LOS) condition. Each tap undergoes independent Rayleigh (NLOS condition) or Rician (LOS condition) fading with a corresponding mean average power. The maximum specified terminal speed is 3 m/s [45].

With multiple antenna technologies being considered as a viable solution for the next generation of WLANs, a set of channel models for indoor MIMO WLAN systems has been recently proposed in [46]. Some of these models are extensions to the existing HIPERLAN/2 channels. The newly developed multiple antenna channels are based on the cluster approach introduced in [47]. Angular spread (AS), angle-of-arrival (AoA) and angle-of-departure (AoD) parameters are assigned to each tap and cluster. Also, antenna correlation is used to realistically describe the transmitting and receiving ends in MIMO WLANs [48]-[51].

2.2.2 Time Domain Correlation

The multipath channel environment causes time and frequency selective fading. This is often described by the time domain and frequency domain correlation functions [52]-[55]. The time domain correlation function shows the correlation between the channel responses of two symbols that are $(i' - i)$ symbols apart. The frequency domain correlation function shows the correlation between the channel responses of

two subcarriers that are $(k' - k)$ subcarriers apart.

For the total average power of the CIR normalised to unity, the channel correlation function of the CFR, $r_H(i' - i, k' - k)$, can be separated into the multiplication of a time domain correlation, $r_t(i' - i)$, and a frequency domain correlation, $r(k' - k)$, defined by [15]

$$r_H(i' - i, k' - k) \triangleq E\{H(i', k')H(i, k)^H\} = r_t(i' - i)r(k' - k), \quad (2.14)$$

where i' and k' are corresponding indices to i and k respectively, indicating time or frequency separation and also denoting the correlation matrix row number. The superscript $(\cdot)^H$ denotes Hermitian transpose.

The time domain correlation of the channel is defined by the classical Doppler spectrum [45], given by the time domain correlation function

$$r_t(i' - i) = J_0(2\pi T_f f_D(i' - i)), \quad (2.15)$$

where $J_0(\cdot)$ is the zeroth order Bessel function of the first kind and f_D is a maximum Doppler frequency, given by

$$f_D = \frac{vf_c}{C}, \quad (2.16)$$

where v is the mobile terminal speed, f_c is the carrier frequency and C denotes speed of light.

In general, an OFDM receiver does not know the reference terminal speed, v , and also a maximum Doppler frequency, f_D . To generate the time domain correlation matrix, an expected value for f_D may be used (the worst case scenario) or alternatively velocity of a terminal can be measured in real time. The time domain correlation matrix should also be updated in real time. One possible method for velocity estimation in OFDM systems has been described in [56].

2.2.3 Frequency Domain Correlation

The frequency domain correlation of the channel is defined by the channel power delay profile [52]-[55]. The channel power delay profile is generally classified as

exponentially decaying or uniformly distributed (often called uniform) [44].

Based on indoor measurements in 5 GHz band, HIPERLAN/2 channel models specify the exponentially decaying power delay profile, given by [45], [57]

$$\theta_e(\tau_m) = Ae^{-\tau_m/\tau_{rms}}, \quad (2.17)$$

where the subscript $(\cdot)_e$ denotes exponential, A is a constant and τ_{rms} denotes the r.m.s. delay spread.

For uniformly and independently distributed delays τ_m over the CP length, L , the frequency domain correlation coefficients, $r(k' - k)$, of the matrix given by Equation (2.14) can be expressed by [57]

$$r(k' - k) = \int_0^L \theta(\tau_m) e^{-j2\pi\tau_m(k' - k)/K} d\tau_m. \quad (2.18)$$

After the integration over the given limits in Equation (2.18) for $\theta(\tau_m) = \theta_e(\tau_m)$, correlation coefficients $r_e(k' - k)$ for the exponential power delay profile, normalized to unity for all $k' = k$, are given by [57]

$$r_e(k' - k) = \frac{1 - e^{-L((1/\tau_{rms}) + j2\pi(k' - k)/K)}}{\tau_{rms} (1 - e^{-L/\tau_{rms}}) \left(\frac{1}{\tau_{rms}} + j2\pi \frac{k' - k}{K} \right)}. \quad (2.19)$$

From Equation (2.19) can be found the coherence bandwidth of the channel that is in strong relationship with the r.m.s. delay spread, τ_{rms} [13]. The coherence bandwidth determines the range of frequencies over which the channel can be considered flat.

Similar to the terminal velocity estimation, an OFDM receiver does not generally know the reference r.m.s. delay spread of the channel. To generate the frequency domain correlation matrix, an expected value for τ_{rms} may be used or alternatively the r.m.s. delay spread can be measured in real time. One estimation method of r.m.s. delay spread in MISO OFDM is evaluated in Chapter 3 [58].

2.2.4 Correlation Properties in HIPERLAN/2 Channels

HIPERLAN/2 channels have a τ_{rms} ranging between 50 ns and 250 ns and a mobile terminal speed ranging between 0 m/s and 3 m/s [45]. The time domain correlation

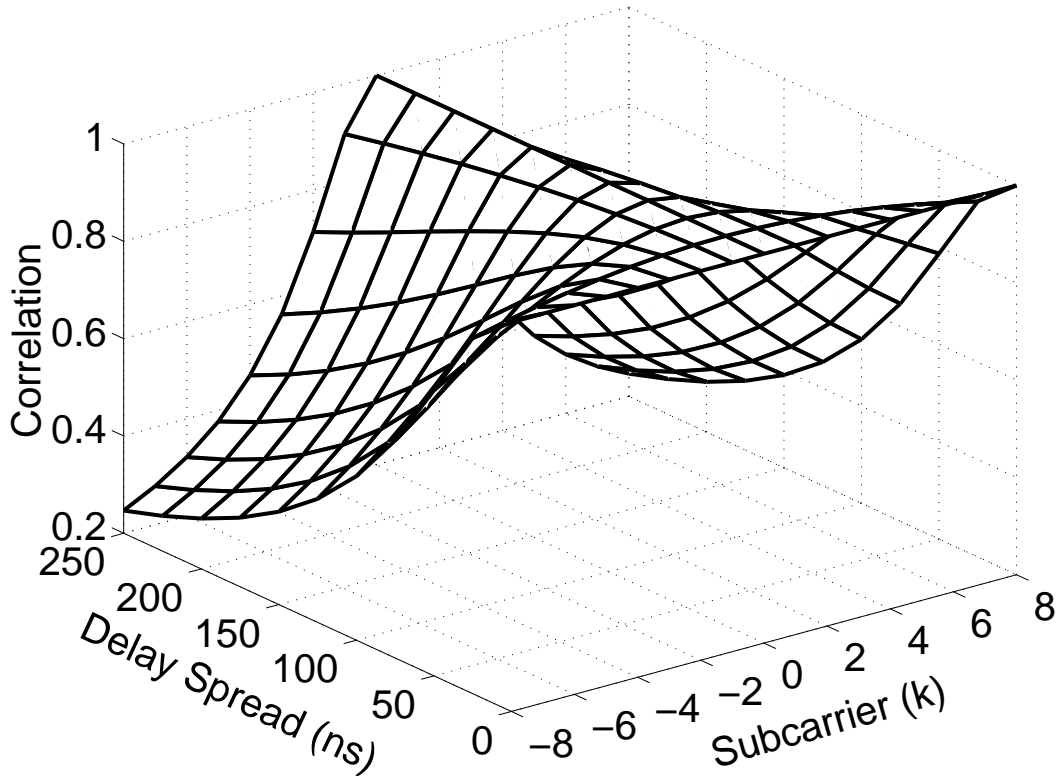


Figure 2.4: Frequency domain correlation in 802.11a for HIPERLAN/2 channels.

remains high for the two consecutive long OFDM pilot symbols (see Fig. 2.3), using the specified Jake's Doppler spectrum. For example, in a system with a carrier frequency $f_c = 5$ GHz and a terminal speed at 3 m/s, $f_D = 50$ Hz. Given a correlation function at $r_t(0) = 1$, it can be found from (2.15) that $r_t(1) = 0.9999996$ when $T_f = 4 \mu\text{s}$.

On the other hand, the frequency domain correlation for the exponential power delay profile depends on the r.m.s. delay spread of the multipath channel. This is shown in Fig. 2.4 for the first 9 subcarriers in a system with subcarrier spacing of $\Delta f = 312.5$ kHz when τ_{rms} is ranging between 0 ns and 250 ns [28]. As delay spread τ_{rms} of a multipath channel increases, the coherence bandwidth of the channel decreases, resulting in reduced correlation between the neighbouring subcarriers.

Thus for an 802.11a OFDM system in HIPERLAN/2 channel environment, the correlation function, $r_H(i' - i, k' - k)$, given by Equation (2.14) for different pilot symbols i and subcarriers k can be simplified to $r(k' - k)$ as follows [28]

$$r_H(i' - i, k' - k) = r_t(i' - i)r(k' - k) \approx r(k' - k), \quad (2.20)$$

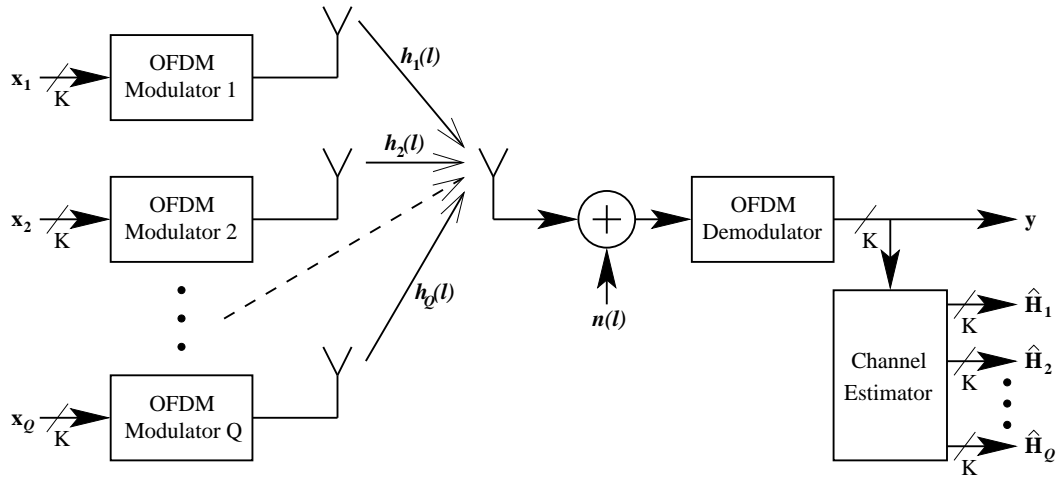


Figure 2.5: MISO OFDM Discrete-Time Model.

for $i = 0, 1$ and $k = 0, 1, \dots, K - 1$.

2.3 Transmitter Diversity in OFDM-based WLANs

Transmitter diversity is an effective way to mitigate multipath fading channels [59]-[65]. Its goal is to generate multiple versions of the same signal by making use of multiple antennas. Thus, even if some of the received versions of the signal are deeply faded, it is highly probable that not all copies experience these deep fades.

2.3.1 OFDM WLANs and Transmitter Diversity

The channel estimation problem in modern OFDM-based WLANs using multiple antennas (as a possible extension to existing standards) has been addressed in many publications in recent years, for example in [58], [66]-[70]. The received signal in the MISO OFDM system is formed as a superposition of the different signals simultaneously sent from all transmit antennas and therefore, this can affect channel estimation performance and its complexity.

A block diagram for coherent MISO OFDM with Q transmitters and 1 receiver is depicted in Fig. 2.5. The MISO scheme can provide a diversity order of $Q \times 1$, given that transmit antennas are separated far enough from each other so that the transmitted signals have zero or minimum cross-correlation.

As shown in Fig. 2.5, the Q transmit antennas $j = 1, 2, \dots, Q$ simultaneously send Q different OFDM symbols, x_j , each formed by K modulated subcarriers using

PSK or QAM constellation. The OFDM symbols, before the IDFT transformation, are defined as follows

$$\begin{aligned}
 \mathbf{x}_1 &\triangleq \{x_1(0), x_1(1), \dots, x_1(K-1)\} \\
 \mathbf{x}_2 &\triangleq \{x_2(0), x_2(1), \dots, x_2(K-1)\} \\
 &\vdots \\
 \mathbf{x}_Q &\triangleq \{x_Q(0), x_Q(1), \dots, x_Q(K-1)\},
 \end{aligned} \tag{2.21}$$

where $x_j(k)$ is an arbitrary complex number with zero mean and variance σ_x^2 . The time domain index, i , is omitted in Equation (2.21) for simplicity.

After the IDFT transformation and cyclic extension, each of these signals is sent through a multipath fading channel and each of them experiences an independent fading, $h_j(l)$. When the fading channel is confined to the CP length, the frequency domain input-output description for MISO OFDM can be given by

$$y(k) = \sum_{j=1}^Q H_j(k)x_j(k) + n(k), \tag{2.22}$$

where $H_j(k)$ is the channel frequency response corresponding to transmit antenna j .

The average SNR at the receiving end is defined by

$$SNR \triangleq \frac{E \left\{ \sum_{j=1}^Q |H_j(k)|^2 \right\}}{N_0}, \tag{2.23}$$

assuming unit variance, σ_x^2 , of data symbols.

After the DFT transformation in the OFDM demodulator, the received signal, \mathbf{y} , is passed to the channel estimator, where Q channel estimation vectors, $\hat{\mathbf{H}}_j$, are obtained. These vectors can further be used to equalise the following data from Q transmit antennas. The channel estimator can also evaluate some other channel statistics, such as the SNR estimation for example, that can be required to the receiver. These are discussed in the following chapters.

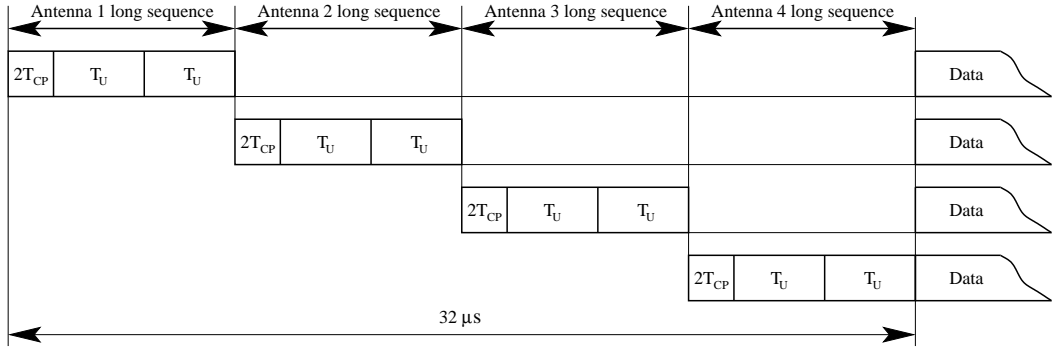


Figure 2.6: A time orthogonal long sequence in MISO OFDM.

2.3.2 Pilot Symbol Structures

One simple solution for a pilot symbol structure in MISO OFDM is to use an independent long pilot sequence for each antenna, while the rest of the antennas remain idle (also called a time orthogonal preamble) [66], [71]. This structure is presented in Fig. 2.6 for a 4×1 MISO scheme within the 802.11a framework. The time orthogonal structure Q times increases an overall preamble length ($4 \cdot 8 = 32 \mu\text{s}$ for $Q = 4$ in Fig. 2.6, refer to Table 2.1).

The above sequence may result in SNR and capacity loss, because a part of the signal power is spent on pilot symbols and because the effective preamble length is increased Q times (due to the idle periods) [4]. The idle periods may also give practical problems for the automatic gain control (AGC) unit in the receiver [67]. The advantage of this structure is that the channel estimation accuracy and complexity for each transmit antenna remains unchanged compared to a SISO OFDM.

An alternative method for the pilot symbol structure is a frequency orthogonal long sequence, where interleaved subchannels are used as an orthogonal set of signals to identify each of the transmitting paths [72]. The advantage of this approach is that the frequency domain interleaving allows maintaining the same pilot symbol overhead as specified for SISO OFDM. The disadvantage of the structure is that interpolation is required between the measured subcarriers to obtain channel estimation in the non-measured subchannels. This can degrade the channel estimation accuracy and generally, advanced signal processing techniques are required (such as for example LMMSE), to maintain an adequate performance of the estimator [4].

Fig. 2.7 presents three different subchannel interleaving structures for a $Q \times 1$ diversity scheme in the frequency domain, requiring an equal average power from

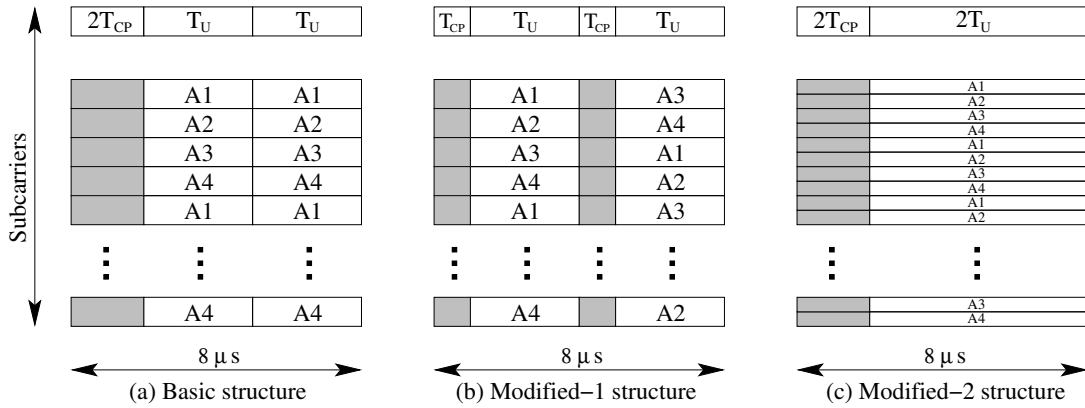


Figure 2.7: Frequency orthogonal long sequences in MISO OFDM.

each transmit antenna, A_j [28]. Fig. 2.7 depicts an example for $Q = 4$.

The binary phase shift keying (BPSK) modulated pilot tones are split into four interleaved subsets $\mathbf{x}_1(i)$, $\mathbf{x}_2(i)$, $\mathbf{x}_3(i)$ and $\mathbf{x}_4(i)$ (one subset for each antenna) within the time and frequency grids of the OFDM pilot symbols $\mathbf{x}(i)$. The channel characteristics can be identified in the non-measured subchannels, by interpolating between the different sets of measured subchannels from the specified transmit antenna.

The first two schemes form two consecutive OFDM pilot symbols, $\mathbf{x}_j(i)$, $i = (0, 1)$, for each antenna $j = (1, 2, \dots, 4)$. The third scheme forms only one pilot symbol, $\mathbf{x}_j(i)$, $i = 0$, for each antenna j . All three schemes have the same preamble length of $8 \mu\text{s}$.

The *basic* scheme, (a), consists of a standard pilot structure in which two long pilot symbols are preceded with a double length CP of 1600 ns, similar to 802.11a. The advantage of this structure is that the CP length remains unchanged as specified by 802.11a and therefore the *basic* scheme remains tolerant to the ISI and ICI in channels with long echoes. Its disadvantage is that the required interpolation can cause a significant estimation error in the non-measured subchannels and especially if the diversity order, Q , is high. The first modified scheme (*modified-1*), (b), splits the two repeated pilot symbols into two independent pilot symbols, each preceded with a single CP length of 800 ns. The *modified-1* scheme doubles the number of measured subcarriers at the expense of the shortened CP length. The double number of measured subchannels can improve the channel estimation performance when the interpolation process is involved [28]. The second modified scheme (*modified-2*), (c), transmits a single pilot symbol preceded by a CP of 1600 ns, over twice the number

of subchannels, but half the bandwidth of the first two schemes. The *modified-2* scheme utilizes the advantages of the two preceding schemes, but introduces a twofold increase of the FFT length, when calculating vector \mathbf{y} . Another disadvantage of this scheme is that it imposes some tighter requirements on the frequency offsets and phase noise due to the closer spacing between the subcarriers. Thus, this scheme presents rather a theoretical than practical interest that enables MSE performance comparison with two others consisting of an identical pilot symbol overhead. It should be also noted that the data following the training sequences in the *modified-2* scheme are sent on normal, K -subcarrier FFT, as specified by [38].

In the following chapters, these three structures will further be used and analysed (individually or jointly). Additionally, two more alternative methods will be compared to the *basic* pilot symbol scheme that allow simultaneous transmission of Q different pilot symbols from Q antennas. The latter two methods have been developed by other authors [16], [19].

2.4 Summary

In this chapter, the discrete-time coherent OFDM system was introduced. Basic OFDM parameters were presented within the 802.11a framework and specifically, channel estimation was discussed for packet type OFDM systems. The non-sample spaced channels, which can cause channel estimation degradation, were outlined. Due to power smearing, the observed CIR is no longer confined to the CP length. This can cause MSE degradation of a channel estimation technique using a temporal approach.

The impairments of the ISI and ICI in OFDM, caused by the fading multipath channel that exceeds the CP length, were also covered. The ISI and ICI can result in MSE degradation of both, data and channel estimation. Each of these two terms can be modelled as an additional source of uncorrelated additive complex Gaussian noise, with zero mean and combined variance of the CIR taps that exceed the CP length.

Time and frequency domain correlation was analysed for modern OFDM-based WLANs in indoor HIPERLAN/2 channel models. As r.m.s. delay spread of a fading

channel increases the coherence bandwidth of the channel decreases resulting in the interpolation performance degradation.

A channel estimation problem was also introduced in a transmit diversity environment. The advantages and disadvantages of a number of different pilot symbol structures were discussed within the 802.11a framework using time domain and frequency domain orthogonal training sequences. The later structure can cause increased estimator complexity, as the required interpolation forces using advanced processing techniques such as LMMSE for example. The former structure may lead to OFDM system capacity loss due to the increased pilot symbol overhead.

Chapter 3

Estimation of Channel Statistics in MISO OFDM

The Bayesian type estimators, such as for example LMMSE, exploit prior information of multipath channel statistics that give better performance of the channel estimation. These are generally the SNR, maximum excess delay of the power delay profile, r.m.s. delay spread and velocity of a terminal. The latter parameter estimation can be avoided in the packet type OFDM systems as the packet length is generally chosen short enough such that the time variations of the channel can be considered constant over the packet [4]. The former parameter estimations are evaluated in the following sections based on the initial, coarse channel estimation.

3.1 Coarse Channel Estimation

When pilot symbols are used, the coarse channel estimation in MISO OFDM can be obtained by multiplying the inverse of the diagonal matrix, containing training symbols $\mathbf{x}_j(i)$, by the received column vector, $\mathbf{y}(i)$, at a time instant, i . This technique is well known as least-squares (LS) channel estimation and its advantage is simplicity (one complex multiplication per one frequency bin is all what is required for channel estimation) [17]. A drawback of the LS estimation is its high MSE. Thus, frequency or time domain (or even both in doubly selective fading channels) post-filtering is generally needed in order to obtain fine channel estimation. Alternatively, more than one pilot symbol can be sent that will average out the channel noise from

the observed channel estimation vectors at the receiving end, as for example in the 802.11a system [38].

The latter approach can lead to a capacity and SNR loss in an OFDM system due to the increased pilot symbol overhead, the former approach can enlarge a computational complexity at the receiving end.

LS estimation in MISO OFDM is described below for pilot symbol structures presented in Fig. 2.7.

The Q transmit antennas $j = 1, 2, \dots, Q$ simultaneously send Q different OFDM pilot symbols. One or another structure (Fig. 2.7) is used to interleave K subcarriers in the frequency domain.

By letting K/Q be an integer, the *basic* pilot symbol scheme (Fig. 2.7(a)) is defined in vector notation as follows

$$\begin{aligned}
 \mathbf{x}_1(i) &\triangleq \{x_1(i;0), 0, \dots, 0, x_1(i;Q), 0, \dots, 0, x_1(i;K-Q), 0, \dots, 0\} \\
 \mathbf{x}_2(i) &\triangleq \{0, x_2(i;1), 0, \dots, 0, x_2(i;Q+1), 0, \dots, 0, x_2(i;K-Q+1), 0, \dots, 0\} \\
 &\vdots \\
 \mathbf{x}_Q(i) &\triangleq \{0, \dots, 0, x_Q(i;Q-1), 0, \dots, 0, x_Q(i;2Q-1), 0, \dots, 0, x_Q(i;K-1)\},
 \end{aligned} \tag{3.1}$$

where $x_j(i;k)$ is an arbitrary complex number with unit magnitude.

The LS estimation vector, $\tilde{\mathbf{P}}_j$, corresponding to antenna j of the two repeated symbols (Fig. 2.7(a)), can be obtained as follows [28]

$$\tilde{\mathbf{P}}_j = \frac{1}{2} \mathbf{X}_j^{-1} \sum_{i=0}^1 \mathbf{y}_j(i), \tag{3.2}$$

where $\mathbf{X}_j = \mathbf{X}_j(i)$, $i = (0, 1)$ is a diagonal matrix of size $K/Q \times K/Q$ that contains the non-zero pilot points, $x_j(i;k)$. For example, $\mathbf{X}_j(i)$ for $j = 1$ and $i = 0$ is given by

$$\mathbf{X}_1(0) = \begin{bmatrix} x_1(0;0) & 0 & \cdots & 0 \\ 0 & x_1(0;Q) & \cdots & 0 \\ \vdots & \vdots & \ddots & \vdots \\ 0 & 0 & \cdots & x_1(0;K-Q) \end{bmatrix}. \tag{3.3}$$

The input-output description for a sub-set of K/Q subcarrier symbols, corresponding to transmit antenna j and pilot symbol i , can be given by

$$y_j(i; k) = H_j(i; k)x_j(i; k) + n(i; k). \quad (3.4)$$

Furthermore, the average of the two repeated pilot symbols, as defined by Equation (3.2), produces 3 dB improvement of the noise performance.

In the *modified-1* scheme (Fig. 2.7(b)), the two independent pilot symbols correspond to one antenna j . Therefore, the LS estimation vector, $\tilde{\mathbf{P}}_j$, can be obtained by union between these two symbols as follows

$$\tilde{\mathbf{P}}_j = \bar{\mathbf{P}}_j(0) \cup \bar{\mathbf{P}}_j(1), \quad (3.5)$$

where $\bar{\mathbf{P}}_j(i)$ is the LS estimation vector at the non-zero pilot points of length K/Q that corresponds to the i th pilot from the j th transmitter. $\bar{\mathbf{P}}_j(i)$ is given by

$$\bar{\mathbf{P}}_j(i) = \mathbf{X}_j^{-1}(i)\mathbf{y}_j(i), \quad (3.6)$$

where $\mathbf{X}_j(0)$ is given by Equation (3.3).

$\mathbf{X}_j(1)$ is obtained by a cyclic shift of $\mathbf{x}_j(i)$ rows in Equation (3.1), such that a minimum distance is achieved between the subcarriers corresponding to each antenna j , after the union given by Equation (3.5). This is shown in Fig. 2.7(b) for MISO OFDM with $Q = 4$ transmit antennas.

The union operation in Equation (3.5) produces the LS vector of length $2K/Q$ compared to the average operation in Equation (3.2) that produces the LS vector of length K/Q . The double length estimation vector, $\tilde{\mathbf{P}}_j$, makes the *modified-1* structure a better choice compared to the *basic* structure especially when the interpolation process is necessary.

Equation (3.6) also represents the LS estimation vector, $\tilde{\mathbf{P}}_j = \bar{\mathbf{P}}_j(i)$, $i = 0$, of length $2K/Q$ for the *modified-2* pilot scheme that uses $2K$ subcarriers (in Fig. 2.7(c)). As in the *modified-1* pilot scheme, the closer spacing between the subcarriers makes the *modified-2* scheme better choice than the *basic* scheme when the interpolation process is required.

Some other channel parameters can be obtained from the LS estimation. These

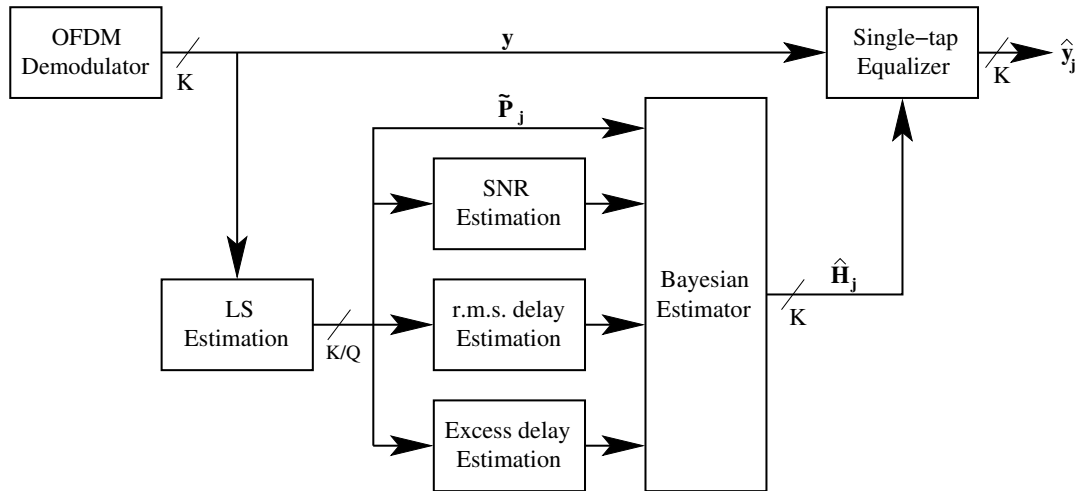


Figure 3.1: Generalised block diagram of the MISO OFDM receiver using a Bayesian type channel estimator with interleaved subcarriers in the frequency domain.

are shown in Fig. 3.1 where a generalised block diagram of the MISO OFDM receiver is presented. The parameter estimation will be discussed in the following sections.

3.2 SNR Estimation

SNR is an important system parameter that knowledge is often required in real time to optimise the performance of a communication system [73]-[77]. For example, the estimated SNR can be used to improve LMMSE channel estimation accuracy under real time conditions [58].

3.2.1 SNR Estimation Methods in MISO OFDM

This section presents two low-complexity SNR estimation algorithms for OFDM systems with transmitter diversity. The first algorithm is a frequency domain method that makes use of the two repeated symbols in the *basic* pilot structure (refer to Fig. 2.7(a)). The second algorithm is DFT-based that will be evaluated later in this section[78]. Both algorithms are studied in HIPERLAN/2 non-sample spaced channel environments [45].

If a multipath channel is non-sample spaced, it will produce smearing of the CIR when IDFT transformation is involved. This can cause degradation of the SNR estimation. It is shown that proper windowing of the measured CIR or alternatively a pre-advancement of the timing point [19] can effectively improve the SNR estimation quality in the DFT-based method.

In MISO OFDM, the average SNR at the receiving end is defined by Equation (2.23). With the total transmit power normalized to unity, it only requires estimating the noise variance, \hat{N}_0 , to obtain its reciprocal SNR estimation.

In an OFDM system with transmit diversity, an accurate estimation of the noise variance, \hat{N}_0 , can be given by [79]

$$\hat{N}_0 = \frac{1}{K} \sum_{k=0}^{K-1} \left| y(k) - \sum_{j=1}^Q \hat{H}_j(k) \hat{x}_j(k) \right|^2, \quad (3.7)$$

where $\hat{x}_j(k)$ is the filtered, channel distortion-free estimated signal at subcarrier k .

The noise variance estimation, \hat{N}_0 (and therefore the SNR estimation), in Equation (3.7) requires a prior knowledge of $\hat{H}_j(k)$ and $\hat{x}_j(k)$ values, which are generally not available before the fine channel estimation. This problem is investigated in Section 5.1, where the LMMSE channel estimator requires only a coarse SNR estimation for selecting between two groups of coefficients stored in LUTs [58].

In the following, two noise variance estimation methods are evaluated for the pilot symbol structures presented in Fig. 2.7.

The *basic* scheme, Fig. 2.7(a), uses two repeated symbols, $x_j(i; k)$, $i = (0, 1)$. Hence, the noise variance estimation at the receiving end is simply given by the MSE between the two repeated pilot symbols, $\mathbf{y}(i)$, as follows

$$\hat{N}_0 = \frac{1}{2K} \sum_{k=0}^{K-1} (|y(0; k) - y(1; k)|^2), \quad (3.8)$$

assuming that the channel noise vector, $\mathbf{n}(i)$, is i.i.d. complex zero mean Gaussian with variance N_0 (refer to Section 2.1.1) that affects each of the process $y(0; k)$ and $y(1; k)$ independently. Thus, the mean variance will result in double noise power, which should be scaled down by a factor of two (or -3 dB). The scale factor of 2 is included in Equation 3.8. The above method is called a frequency domain method as the SNR estimation processing is carried out solely in the frequency domain (refer to Equation (3.8)).

The *modified-1* and *modified-2* schemes use non-repeated pilot symbols for channel estimation as shown in Fig. 2.7(b) and Fig. 2.7(c). Hence, Equation (3.8) becomes unsuitable for these two schemes and an alternative noise variance estimation algorithm is required. This is evaluated below [78].

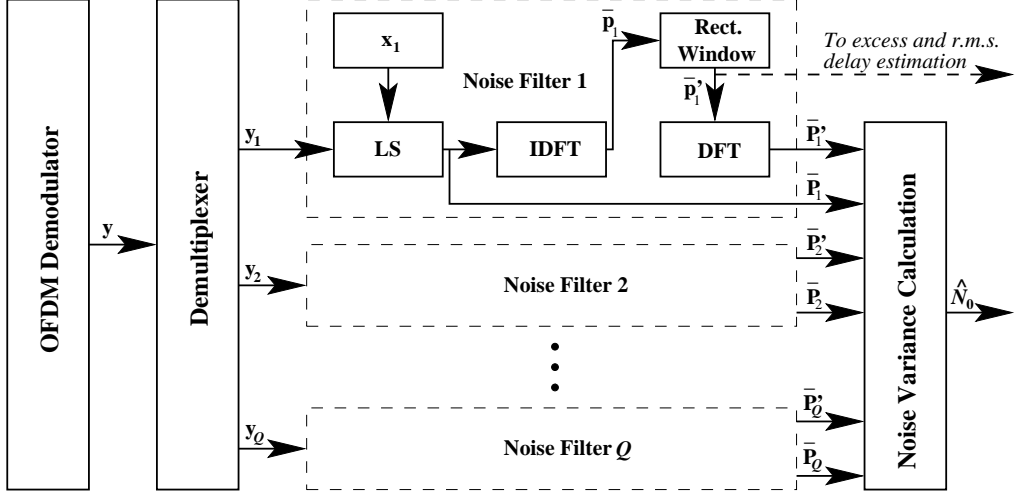


Figure 3.2: DFT-based noise variance estimation in MISO OFDM using non-repeated pilot symbols interleaved in the frequency domain.

A block diagram of the DFT-based noise variance estimation is presented in Fig. 3.2 for the non-repeated pilot symbol vectors, \mathbf{x}_j . The LS estimation is also included in the block diagram.

The pilot symbol, \mathbf{y} , from the MISO OFDM demodulator output is passed through the demultiplexer, which splits the pilot symbol into Q vectors, \mathbf{y}_j , each of length K/Q (Fig. 3.2). After the LS estimation of \mathbf{y}_j , given by Equation (3.6), a corresponding CIR is obtained from vector $\bar{\mathbf{P}}_j$ by means of the K/Q -point IDFT in the noise filter block. For $K/Q \geq L_0$, the observed CIR corresponding to transmit antenna j is given by [78]

$$\bar{\mathbf{p}}_j = \frac{Q}{K} \mathbf{F}^{-1} \bar{\mathbf{P}}_j, \quad (3.9)$$

where \mathbf{F} is the Fourier matrix, given by [80]

$$\mathbf{F} = \begin{bmatrix} 1 & 1 & \cdots & 1 \\ 1 & W_{K/Q}^{1 \cdot 1} & \cdots & W_{K/Q}^{1 \cdot (K/Q-1)} \\ 1 & W_{K/Q}^{2 \cdot 1} & \cdots & W_{K/Q}^{1 \cdot (K/Q-1)} \\ \vdots & \vdots & \ddots & \vdots \\ 1 & W_{K/Q}^{(K/Q-1) \cdot 1} & \cdots & W_{K/Q}^{(K/Q-1) \cdot (K/Q-1)} \end{bmatrix}. \quad (3.10)$$

After the IDFT transformation given by Equation (3.9), a filtering is performed of the noisy CIRs by passing the vectors, $\bar{\mathbf{p}}_j$, through a rectangular window such that

$$\bar{p}_j'(l) = \begin{cases} \bar{p}_j(l) & 0 \leq l < L_0, \\ 0 & \text{elsewhere.} \end{cases} \quad (3.11)$$

The windowing operation reduces the noise variance of the LS estimation vectors, $\bar{\mathbf{p}}_j$, each of length K/Q by a factor of QL_0/K [66].

The filtered channel estimation vectors, $\bar{\mathbf{P}}_j'$, are obtained by a reverse K/Q -length DFT transformation as follows

$$\bar{\mathbf{P}}_j' = \mathbf{F}\bar{\mathbf{p}}_j'. \quad (3.12)$$

With the appropriate scaling, the noise variance in MISO OFDM for non-repeated pilot symbols is found as an MSE between the filtered vectors, $\bar{\mathbf{P}}_j'$, and the noisy LS estimation vectors, $\bar{\mathbf{P}}_j$, given by [78]

$$\hat{N}_0 = \frac{1}{K - L_0} \sum_{k=0}^{K/Q-1} \sum_{j=1}^Q (|\bar{P}_j'(k) - \bar{P}_j(k)|^2). \quad (3.13)$$

If the MISO OFDM operates in a non-sample spaced channel environment, the leakage problem given by Equation (2.7) can reduce the quality of the noise variance estimation, \hat{N}_0 , due to the CIR power smearing. This is shown in Fig. 3.3 for one interleaved OFDM pilot symbol in the frequency domain with $T_s = 50$ ns, $K/2 = 32$ active subcarriers and $L_0 = 8$ samples. The symbol was sent in a 2×1 diversity scheme. A random noiseless realisation of HIPERLAN/2 channel A was generated with the total CIR power normalised to unity.

As most of the observed CIR power remains in the neighbourhood of the original pulse location, a simple windowing method can be used to improve the noise variance estimation quality [17]. This can be accomplished by including in Equation (3.11) the CIR taps that lie outside the first L_0 taps, exceeding a particular threshold level of the CIR power. This is shown in Fig. 3.3(a).

With this, Equation (3.11) can be rewritten as follows

$$\bar{p}_j'(l) = \begin{cases} \bar{p}_j(l) & 0 \leq l < L_0, \\ \bar{p}_j(l) & (K/Q - \beta) \leq l < K/Q, \\ 0 & \text{elsewhere,} \end{cases} \quad (3.14)$$

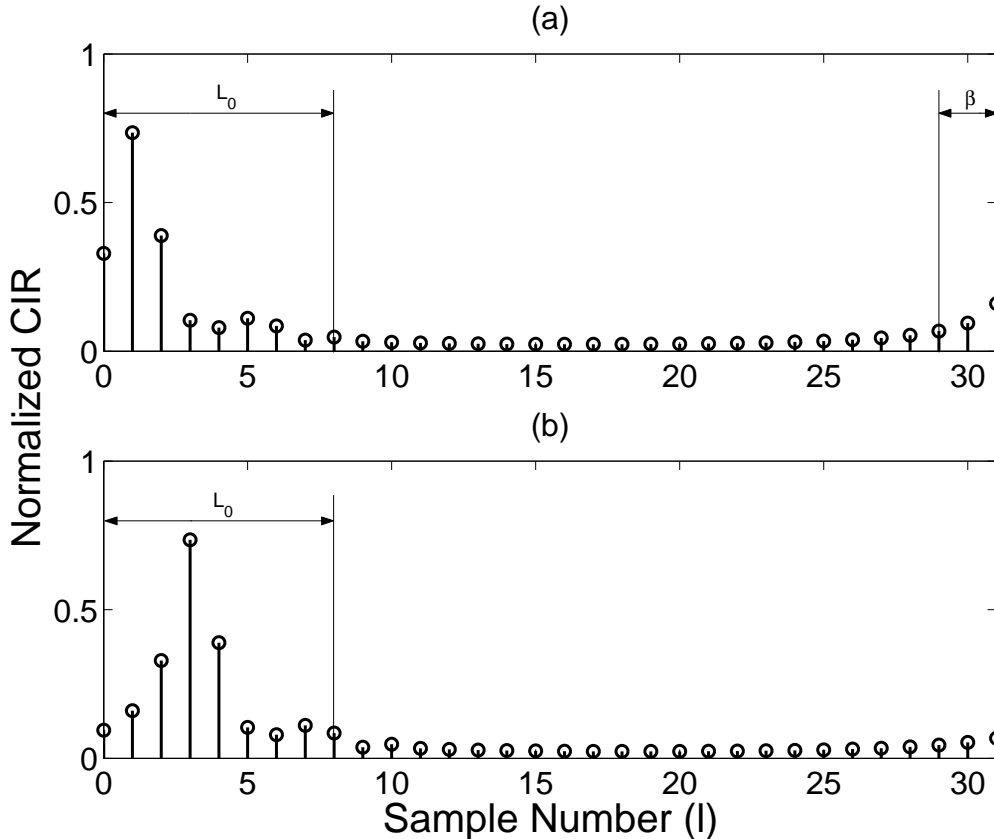


Figure 3.3: Observed CIR of HIPERLAN/2 channel A in a 2×1 scheme using one interleaved pilot symbol in the frequency domain: (a) a noiseless random realisation; (b) a cyclic shift of the CIR for $\beta = 2$ samples.

where β denotes the CP window extension operator.

Otherwise, a pre-advancement of the timing point or in other words a cyclic shift of the CIR for β samples can be used as shown in Fig. 3.3(b), where $\beta = 2$. The L_0 length can also be extended for β samples (not shown in the figure) [19].

Alternatively, the noise variance estimation can be obtained in the time domain by just summing energy of taps with the least significant power of the observed CIR, $\bar{\mathbf{p}}_j$. The advantage of this method is that in general it would require less processing operations compared to Equation (3.13) and especially in an OFDM system with the small number of subcarriers, operating in the large delay spread channels. Equation (3.13) requires K complex conjugate multiplications and Q K/Q -point DFTs to obtain vectors $\bar{\mathbf{P}}'_j$, whereas the alternative method would require $(K/Q - L_0)Q$ complex conjugate multiplications. On the other hand, the method given by Equation (3.13) makes use of the filtered LS estimation vectors that can be used as the fine channel estimates after simple linear interpolation of vectors $\bar{\mathbf{P}}'_j$, each of length

K/Q . This simplified channel estimation approach can be applied when advanced processing techniques such as LMMSE are not practical due to high implementation complexity. It should be also noted that the filtered CIR, $\bar{\mathbf{p}}'_j$, can further be used for the maximum excess and r.m.s. delay spread estimations (shown by a dotted arrow in Fig. 3.2).

The quality of the noise variance estimation can be further improved if more than one set of pilot symbols is available, as for example in an 802.11a OFDM system using two long pilot symbols for channel estimation. The improved noise variance estimation can be achieved by the union operation given by Equation (3.5) between the two independent pilot symbols, prior to the noise variance estimation using Equation (3.13). The union operation doubles the LS estimation vector $\bar{\mathbf{P}}_j$ length and therefore improves the quality of the CIR estimation (and also the noise variance estimation) by means of IDFT transformation.

3.2.2 Numerical Results

The coarse SNR estimation algorithms given by Equations (3.8) and (3.13) were simulated in the 802.11a framework for the *basic* (Fig. 2.7(a) for $Q = 2$) and *modified-1* (Fig. 2.7(b) for $Q = 2$) pilot symbol structures in a 2×1 diversity scheme. HIPERLAN/2 non-sample spaced channel A, C and an equal power 2-ray sample-spaced channel (for a reference) were used in simulations. The 2-ray channel was known to have $\tau_{rms} = 50$ ns and a maximum excess delay of the power delay profile, $\tau_x = 100$ ns.

In the *basic* pilot symbol structure, L_0 parameter was set equal to the CP length of $L_0 = L = 16$ samples. A perfect time and frequency synchronisation was assumed at the receiver and the total transmit power was normalized to unity.

The noise variance estimation at each SNR value was evaluated using 1000 trials of randomly generated channels. Two long OFDM pilot symbols were simultaneously sent from each of two transmit antennas through a fading multipath channel using one or another pilot symbol structure. A new channel was randomly generated for each pilot sequence, but the channel remained constant over the sequence.

Prior to the noise variance estimation in the *modified-1* pilot scheme by means of Equation (3.13), the union operation was accomplished between the two independent

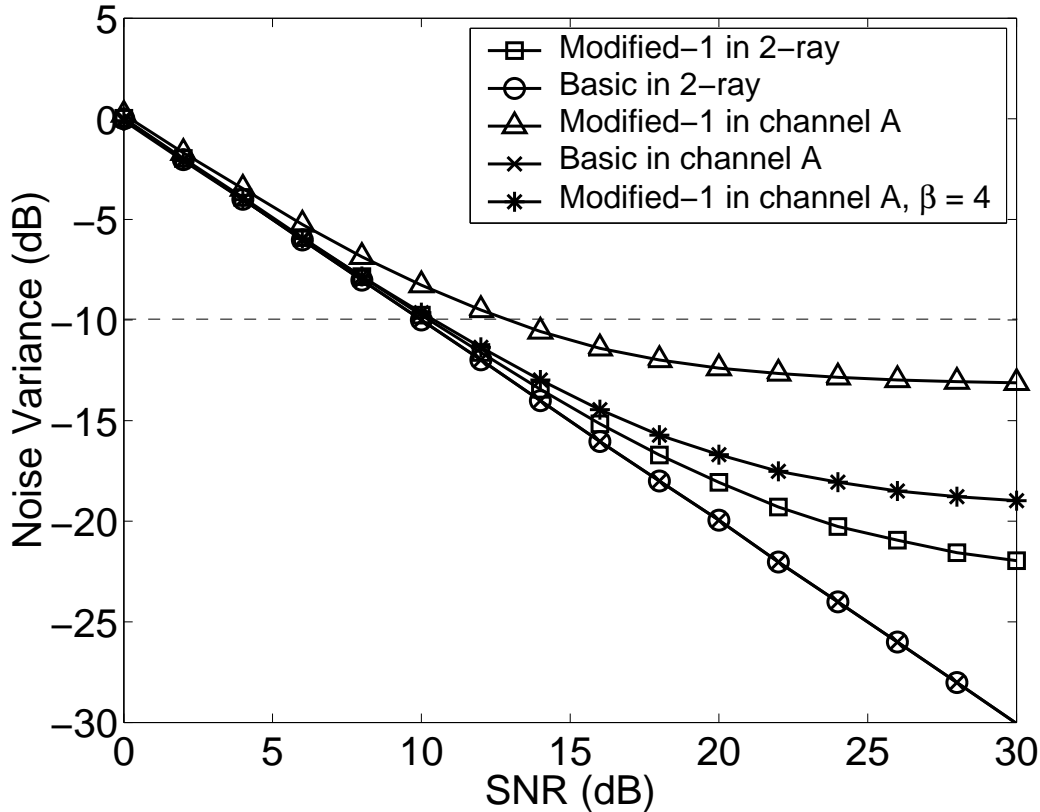


Figure 3.4: Coarse noise variance estimation in a 2×1 OFDM for sample-spaced 2-ray channel and HIPERLAN/2 channel A.

pilot symbols given by Equation (3.5). After the union, the null-guard tones (refer to Table 2.1) were set according to the average of adjacent measured subcarriers to prevent transient effect (the so called Gibb's phenomenon [30], [81]), when the IDFT operation was involved given by Equation (3.9). The tone allocation is given by

$$\tilde{P}(k) = \begin{cases} (\tilde{P}(1) + \tilde{P}(63))/2 & k = 0; \\ (\tilde{P}(26) + \tilde{P}(38))/2 & k = 27, 28, \dots, 37. \end{cases} \quad (3.15)$$

The frequency domain method in the *basic* pilot scheme provides almost perfect noise variance estimation (refer to Equation (3.8)) for both sample-spaced 2-ray channel and non-sample spaced channel A, as shown in Fig. 3.4. This is because the noise variance estimation was solely accomplished on the measured subchannels in the frequency domain that were actually used in the analysed OFDM system. No additional processing was involved, such as IDFT, that might degrade the noise variance estimation accuracy. Also, the CIR was confined to the CP length for both

2-ray and channel A, i.e. ISI and ICI error free.

In the *modified-1* pilot scheme, the tone allocation given by Equation (3.15) improves the quality of the CIR estimation by means of Equation (3.9) (and consequently the noise variance estimation). However, irrespective of these, an error floor at high SNRs still exists in the DFT-based method. This is shown in Fig. 3.4 for the 2-ray equal power sample spaced channel, with almost 8 dB performance loss at high SNRs compared with the ideal SNR knowledge (and also with the SNR estimation performance of the frequency domain method). The actual CIR of the sample-spaced channel cannot be accurately recovered by the IDFT transformation because the null-guard tones are filled in according to the average of adjacent frequency bin values. This is still poor approximation to the real channel, but is preferable to leaving the frequency bins at zero.

The effect of a non-sample spaced channel (HIPERLAN/2 channel A) on the noise variance estimation quality in the DFT-based method is also shown in Fig. 3.4. Due to the leakage problem given by Equation (2.7), a portion of the CIR power is lost by windowing given by Equation (3.11) (also refer to Fig. 3.3). Although the enhanced windowing given by Equation (3.14) effectively improves estimation accuracy by almost 6 dB at SNR = 30 dB for $\beta = 4$, the effects of null-guard tones and CIR power leakage result in an estimation error floor at high SNRs.

The same conclusion also holds for channel C as shown in Fig. 3.5. The frequency domain method (only possible in the *basic* scheme) obtains almost perfect noise variance estimation, since the frequency domain SNR estimation in the *basic* pilot scheme does not produce any interpolation errors and the CP length is long enough ($L = 32$ samples) to avoid the interference due to ISI and ICI.

On the contrary, the effects of null-guard tones and CIR power leakage result in the estimation error floor at high SNRs for the DFT-based method in the *modified-1* scheme. The benefit of the enhanced windowing given by Equation (3.14) is not as evident as it was in channel A (Fig. 3.4), because the longer delay spread reduces the coherence bandwidth making the simple approximation for the null bins (using Equation (3.15)) even less valuable. The achieved MSE gain of ‘*Modified-1* in channel C, $\beta = 4$ ’ curve over the ‘*Modified-1* in channel C’ in Fig. 3.5 is almost two times less than in channel A and about 3.5 dB at SNR = 30 dB.

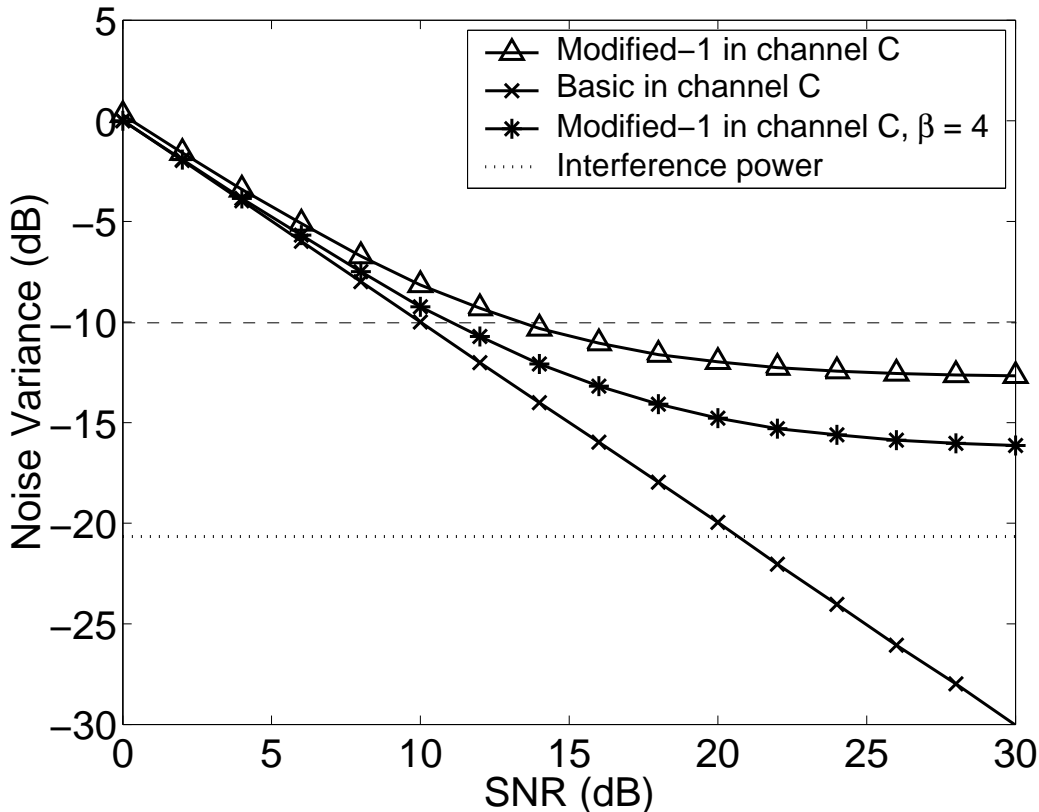


Figure 3.5: Coarse noise variance estimation in a 2×1 OFDM for HIPERLAN/2 channel C.

In addition, interference power is present in this scheme due to ISI and ICI, caused by the reduced CP length to 800 ns (note $\tau_x = 1050$ ns for channel C). Interference power is shown by the dotted line in Fig. 3.5. It was obtained by Equation (2.11), indicating that the interference error is well below the error floor of the noise variance estimation curves in the *modified-1* scheme. Thus, CIR power leakage and tone allocation by means of simple approximation (Equation (3.15)) dominate the error floor of the noise variance estimation in the *modified-1* pilot symbol structure.

Clearly, in realistic scenarios based on the 802.11a OFDM system parameters and HIPERLAN/2 channel models, the noise variance estimation given by Equation (3.13) gives poor performance at high SNRs and therefore the DFT-based method should be regarded as the coarse noise variance estimation technique.

However, in some applications, such as the real time LMMSE channel estimation evaluated in section 5.1, it is only required that the coarse SNR estimation defines a threshold level between the low and high SNRs. A typical threshold level would

be -10 dB and this is shown by the dashed line in Fig. 3.4 and Fig. 3.5. Both, the frequency based and DFT-based noise variance estimation algorithms are suitable for this kind of application.

3.3 Maximum Excess Delay Estimation

3.3.1 Estimation Method in MISO OFDM

The LMMSE channel estimation in MISO OFDM with interleaved subcarriers exploits correlation function of the multipath channel for filtering and interpolation between the measured subchannels to enhance the channel estimation accuracy in the non-measured subchannels. The correlation function requires prior knowledge of the maximum excess delay, τ_x , if the channel is with a uniform power delay profile or r.m.s. delay spread, τ_{rms} , if the channel is with an exponential power delay profile [82].

The maximum excess delay of the power delay profile is defined by the time delay during which multipath energy falls to ρ dB below the maximum of the power delay profile, and can be determined from $\theta(\tau_m)$ [13]. In OFDM systems, subchannels exhibit frequency nonselective or flat fading, as the maximum excess delay is less than the OFDM symbol duration ($\tau_x < T_f$). Thus, τ_x can be obtained by passing the observed CIR, given by Equation (2.6), through the predefined multipath power threshold level, ρ . The most significant tap delay at time delay $\tau_x \leq L$, corresponding to the multipath component that is above ρ , will indicate the estimated maximum excess delay, $\hat{\tau}_x$, given by [82]

$$\hat{\tau}_x^j = \arg \max_l \{10 \log_{10}(|h_j(l)|^2) > \rho\}. \quad (3.16)$$

where the superscript $(\cdot)^j$ denotes transmitter j and $h_j(l)$ is obtained by the IDFT transformation of $\tilde{\mathbf{P}}_j$, given by Equation (3.2) or Equation (3.5). Sample l varies from 0 to $L - 1$.

The multipath power threshold level, ρ , is used to differentiate received multipath components and thermal noise. If ρ is set too low, then the noise will be processed as multipath giving rise to the maximum excess delay estimation, $\hat{\tau}_x^j$ [13]. Conversely,

if ρ is set too high, the maximum excess delay will be underestimated.

3.3.2 Numerical Results

The maximum excess delay estimation given by Equation (3.16) was carried out in the 802.11a framework for a 2×1 diversity scheme in the *basic* (Fig. 2.7(a) for $Q = 2$) and *modified-1* (Fig. 2.7(b) for $Q = 2$) pilot symbol structures. HIPERLAN/2 non-sample spaced channel A and C were used in simulations.

In the *basic* pilot symbol structure, only the first 24 samples (out a possible $L = 32$) were used in Equation (3.16) in order to filter out the leakage components at the most significant taps of the observed CIR (refer to Fig. 3.3(a)). In the *modified-1* scheme, all 16 samples were used for the $\hat{\tau}_x^j$ estimation. A perfect time and frequency synchronisation and also a perfect knowledge of SNR was assumed at the receiving end in the simulations. The total transmit power was normalized to unity. The threshold level, ρ , was set to a fixed value of -24 dB ($-(\max(\text{SNR}) - 6)$ dB, for SNR varying from 0 to 30 dB) of the maximum peak in the normalised CIR. The threshold level of -24 dB was chosen to ensure a good estimation performance for high SNRs.

The maximum excess delay estimation at each SNR value was evaluated using 1000 trials of randomly generated channels. Two long OFDM pilot symbols were simultaneously sent from each of two transmit antennas through a fading multipath channel for one or another pilot symbol structure. A new channel was randomly generated for each pilot sequence, but the channel remained constant over the sequence.

The null-guard tones were set according to Equation (3.15) in the *modified-1* scheme and according to the following equations in the *basic* pilot scheme

$$\tilde{P}_1(k) = \begin{cases} (\tilde{P}_1(2) + \tilde{P}_1(62))/2 & k = 0; \\ (\tilde{P}_1(26) + \tilde{P}_1(38))/2 & k = 28, 30, \dots, 36, \end{cases} \quad (3.17)$$

and

$$\tilde{P}_2(k) = \begin{cases} (\tilde{P}_2(25) + \tilde{P}_2(39))/2 & k = 27, 29, \dots, 37, \end{cases} \quad (3.18)$$

corresponding to antenna $j = 1$ and $j = 2$.

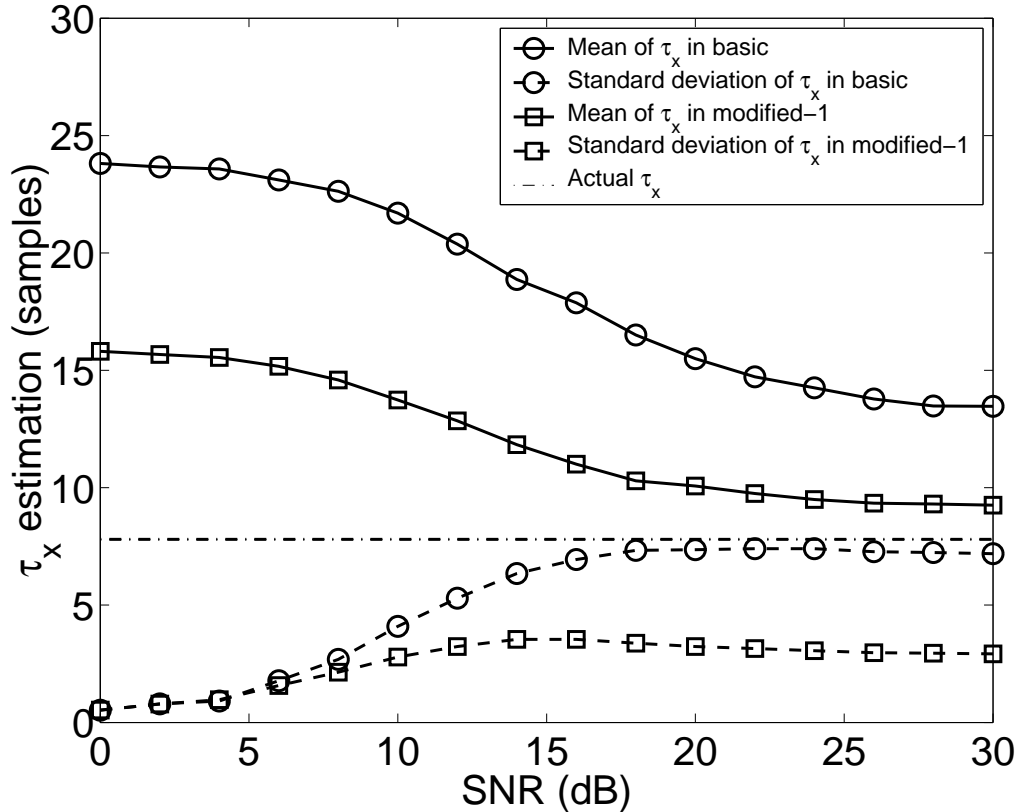


Figure 3.6: Maximum excess delay estimation for channel A (actual $\tau_x = 390$ ns or 7.8 samples) in a 2×1 MISO OFDM.

Results for mean and standard deviation of the maximum excess delay estimation, $\hat{\tau}_x$, in channel A are presented in Fig. 3.6.

As shown in Fig. 3.6, the mean maximum excess delay estimation using the *modified-1* scheme remains within 9–10 samples at high SNRs (≥ 20 dB), compared to the actual 7.8 samples for channel A (refer to Table 2.2). However, the standard deviation shows that the estimation error can vary up to 3 samples, with the worst variations evident at high SNRs. This is due to the leakage that affects the most significant taps within the CP window of the observed CIR. At low SNRs, the estimation error of τ_x can be as high as 100% (particularly at SNR = 0 dB), which is mainly because of the large presence of noise in the measured CIR.

In the *basic* pilot scheme, the estimation error of τ_x becomes greater compared to the *modified-1* scheme as a result of longer window size used in the former scheme with 24 samples. This causes more noise and more leakage presence in the mean and standard deviation estimation of the maximum excess delay and especially in channels with small delay spreads, as for example channel A. The estimation ac-

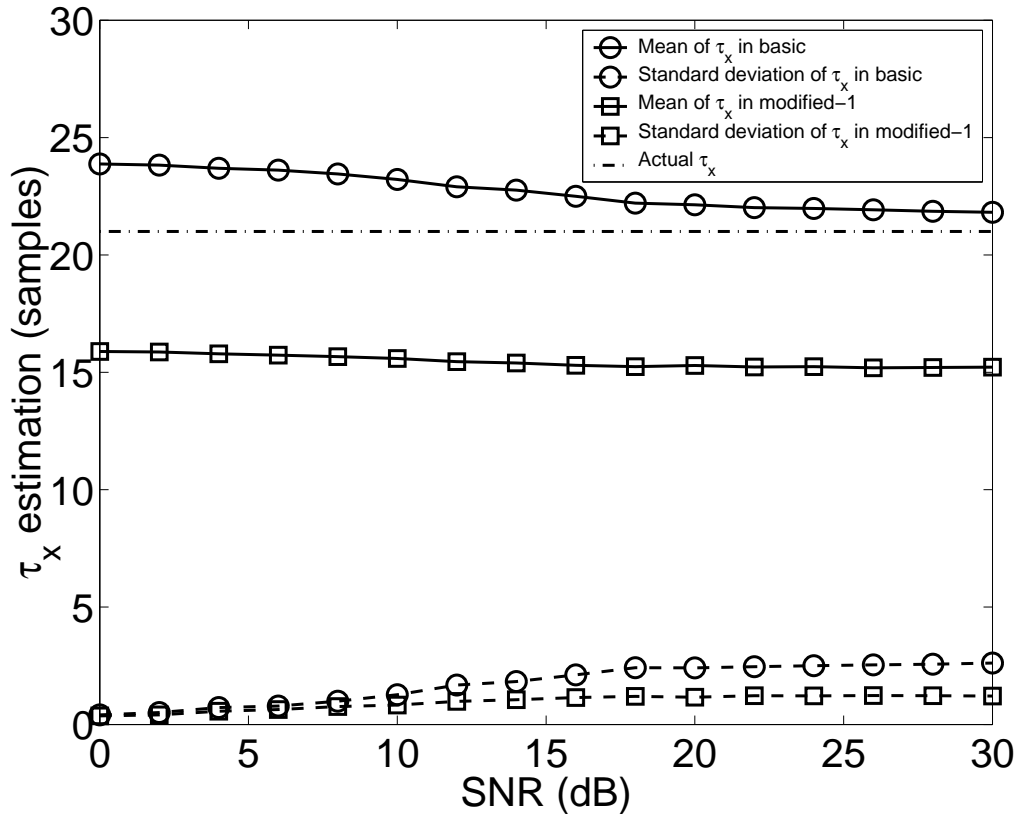


Figure 3.7: Maximum excess delay estimation for channel C (actual $\tau_x = 1050$ ns or 21 samples) in a 2×1 MISO OFDM.

curacy is also affected by a reduced IDFT size to 32 points compared to 64 in the *modified-1* scheme.

By contrast, when channel delay spread is large the *basic* scheme performs better compared to the *modified-1* scheme. This is shown in Fig. 3.7 for channel C with $\tau_x = 21$ samples (refer to Table 2.2). Thus, greater CP window in the *basic* scheme gives closer τ_x estimation accuracy (particularly at $\text{SNR} \geq 20$ dB with estimated $\tau_x \approx 22.5$ samples). The greater CP window size also causes more leakage presence at the most significant taps in the observed CIR, which explains larger standard error at high SNRs (approximately 2.5 samples compared to 1 sample in the *modified-1* scheme). However, the *modified-1* scheme underestimates the maximum excess delay due to the shortened CP length to 16 samples as shown in Fig. 3.7.

3.4 R.M.S. Delay Spread Estimation

3.4.1 Estimation Method in MISO OFDM

The maximum excess delay, τ_x , is not a complete characteristic of a multipath channel because different channels with the same τ_x can exhibit very different profiles of signal over the same delay span [52]. Often the multipath channel is characterised in terms of r.m.s. delay spread, τ_{rms} . The r.m.s. delay estimation can be used for correlation coefficient calculation (refer to Equation (2.19), when correlation properties of the multipath channel are necessary for channel estimation such as LMMSE algorithm for example.

The r.m.s. delay spread is the square root of the second central moment of the power delay profile and can be determined from $\theta(\tau_m)$ [13]. τ_{rms} estimation of the observed CIR, corresponding to transmit antenna j , can be expressed as

$$\hat{\tau}_{rms}^j = \sqrt{\frac{\sum_{l=0}^{\hat{\tau}_x^j-1} |h_j(l)|^2 l^2}{\sum_{l=0}^{\hat{\tau}_x^j-1} |h_j(l)|^2} - \left(\frac{\sum_{l=0}^{\hat{\tau}_x^j-1} |h_j(l)|^2 l}{\sum_{l=0}^{\hat{\tau}_x^j-1} |h_j(l)|^2} \right)^2}, \quad (3.19)$$

where the superscript $(\cdot)^j$ denotes transmitter j .

To improve the quality of $\hat{\tau}_{rms}^j$ estimation given by Equation (3.19), the multipath power components of the observed CIR, $|h_j(l)|^2$, can be initially passed through the predefined multipath power threshold level, ρ , such that

$$h_j(l) = \begin{cases} h_j(l) & 10 \log_{10}(|h_j(l)|^2) > \rho, \\ 0 & \text{otherwise,} \end{cases} \quad (3.20)$$

restricting the observed CIR, $h_j(l)$, to be within the CP length, L .

Similar to the maximum excess delay estimation, if the constant, ρ , is set too low, then the noise will be processed as multipath giving rise to the r.m.s. delay spread estimation, $\hat{\tau}_{rms}^j$ [13]. Conversely, if ρ is set too high, the r.m.s. delay spread will be underestimated.

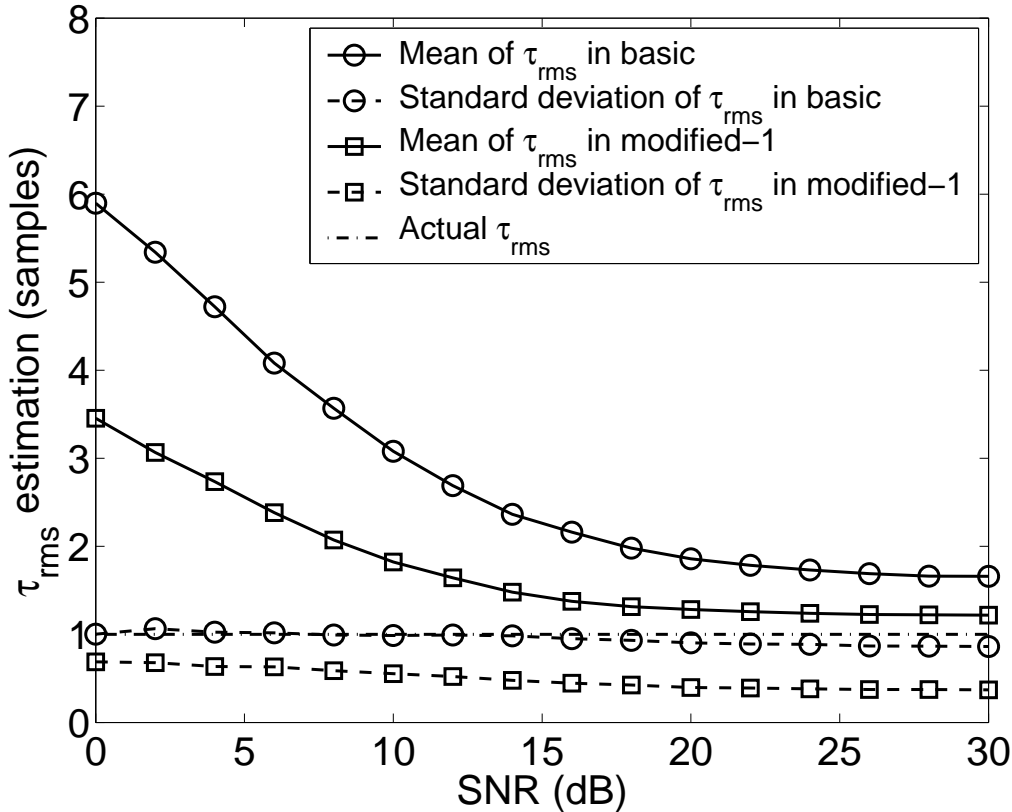


Figure 3.8: R.M.S. delay spread estimation for channel A (actual $\tau_{rms} = 50$ ns or 1 sample) in a 2×1 MISO OFDM.

3.4.2 Numerical Results

Simulations for $\hat{\tau}_{rms}$ estimation were carried out with the same parameters as for $\hat{\tau}_x$ estimation defined in Section 3.3. The results for channel A are presented in Fig. 3.8.

As shown in Fig. 3.8, the mean r.m.s. delay spread estimation using the *modified-1* scheme remains within 1.3 samples at high SNRs (≥ 20 dB), compared to the actual 1 sample for channel A (refer to Table 2.2). The standard deviation also shows a reasonable accuracy with the variation of 0.3 samples at high SNRs. The worst standard error is evident at low SNRs and is due to the poor noise conditions. This is also true for the mean r.m.s. delay spread estimation at low SNRs, when the estimation error of τ_{rms} can be as high as 3.5 samples (particularly at SNR = 0 dB).

Similar to τ_x estimation, the estimation error of τ_{rms} in the *basic* pilot scheme becomes greater compared to the *modified-1* scheme as a result of a relatively longer window size used in the former scheme. This causes more noise and more leakage

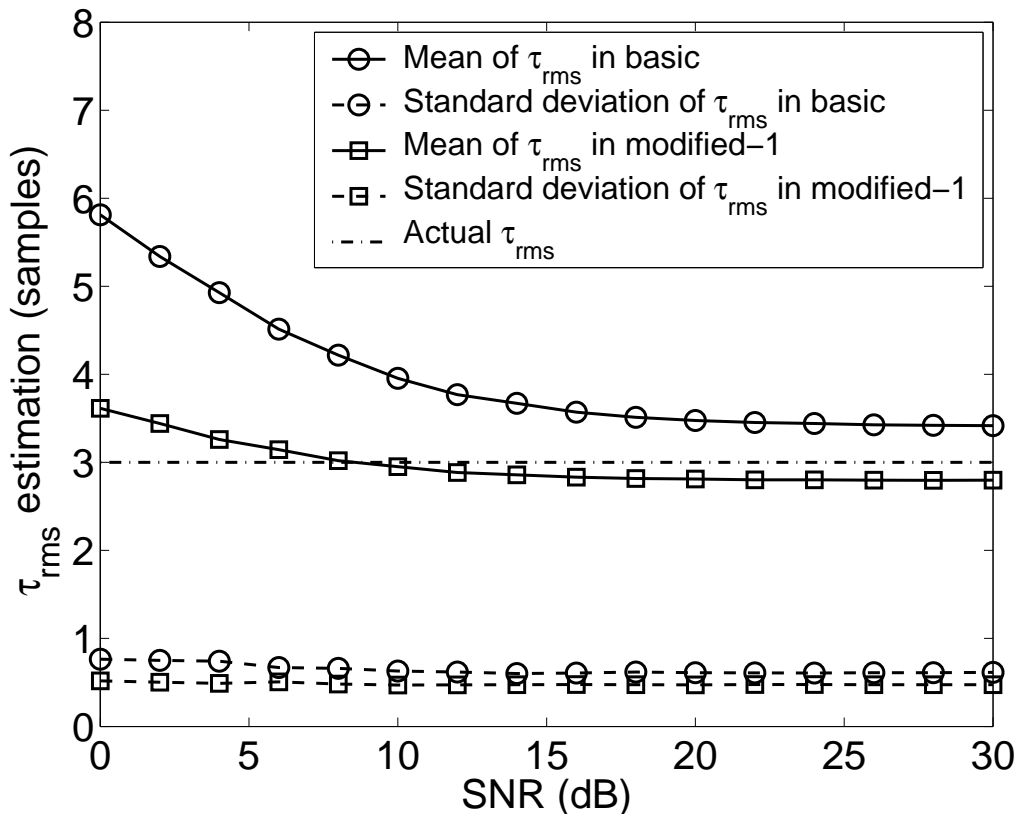


Figure 3.9: R.M.S. delay spread estimation for channel C (actual $\tau_x = 150$ ns or 3 samples) in a 2×1 MISO OFDM.

presence in the CIR and especially in channels with small delay spreads as in channel A. The estimation accuracy is also affected by a reduced IDFT size to 32 points compared to 64 in the *modified-1* scheme.

When channel delay spread is large, the *modified-1* scheme demonstrates an evident r.m.s. delay spread underestimation and especially at high SNRs. This is shown in Fig. 3.9 for channel C (with 2.8 samples at $\text{SNR} \geq 20$ dB compared with actual 3 samples). This scheme though produces better estimation accuracy compared to the *basic* scheme. Poorer estimation accuracy in the latter one can be explained by the CIR smearing in the longer CP window as a result of leakage and also due to poorer accuracy in the CIR measurement using the half size IDFT. In addition, the null-guard tones even further degrade the CIR measurement.

3.4.3 Alternative Techniques for Delay Spread Estimation

Some alternative techniques for delay spread estimation can be found in [83], [84]. Both these techniques have been developed for continuous OFDM systems and use

the correlation of the CP extension of the received OFDM symbols prior to the DFT transformation in the OFDM demodulator. The correlation methods generally produce a better performance and can be adapted to a packet type MISO OFDM. This is left for future work.

3.5 Summary

In this chapter, the estimation of channel statistics was presented for OFDM systems with transmitter diversity in HIPERLAN/2 channels. Specifically, coarse channel estimation was analysed for various pilot symbol structures in a transmit diversity environment. Closer spacing between the subcarriers produces less interpolation error and makes the *modified* schemes a better choice than the *basic* scheme, when postfiltering is required such as, for example, the LMMSE technique.

The SNR, maximum excess delay and r.m.s. delay spread of the power delay profile estimation algorithms were also evaluated in presence of the CIR leakage and null-guard tones (generally used in OFDM-based WLANs). These parameters were obtained from the LS estimation in real time. They can be used to further enhance the LMMSE estimation accuracy in a changing channel environment.

The frequency domain SNR estimation method in the *basic* pilot symbol structure is a better performing technique than the DFT-based approach in the *modified* schemes. This is because SNR estimation in the frequency domain is solely obtained from the subchannels that are actually used in OFDM system. The DFT-based method requiring transformation to the time domain is affected by the CIR smearing and null-guard tones. These two problems also affect the maximum excess delay and r.m.s. delay spread estimation as the IDFT transformation is necessary. If the multipath channel produces a CIR that is confined to the CP length, the *modified-1* scheme results in a better τ_x and τ_{rms} estimation quality due to the closer spacing between the subchannels and therefore higher accuracy of the CIR measurement. By contrast, in channels with long echoes the *basic* pilot structure (with the double length CP) produces higher accuracy of the CIR measurement than the *modified-1* scheme, particularly at high SNRs.

Chapter 4

Channel Estimation in WLANs with Transmitter Diversity

In this chapter, three channel estimation algorithms are compared in WLANs with transmitter diversity. Two algorithms use a temporal approach (often called DFT-based) and have been evaluated by other authors in outdoor channels, such as the 2-ray, typical urban (TU) and hilly terrain (HT) [16], [19]. The third algorithm is a frequency domain method and has been evaluated in previous work for a 7-path fading channel with an exponentially decaying power delay profile [58]. In the following sections, the MSE performance is analysed for these three algorithms in a 2×1 diversity scheme in an indoor environment (HIPERLAN/2 NLOS channel models A and C [45]). In addition, MSE performance is presented for a sample-spaced 2-ray channel for a reference. The CIR lies within the CP length for all the channel models. It is shown that the frequency domain method outperforms the temporal method in realistic scenarios based on HIPERLAN/2 non-sample spaced channels. The poorer performance of the temporal approach is due to the leakage problem, which causes energy loss with the CIR windowing. In addition, null-guard tones are often used in WLANs, which can lead to an accuracy loss in the CIR measurement, when DFT processing is involved. It can further degrade the channel estimation accuracy when a temporal method is used.

4.1 Temporal Approach

Two temporal channel estimation algorithms have been evaluated by other authors and can be briefly summarised as follows [16], [19].

4.1.1 Full Complexity Algorithm

Two transmit antennas, $j = 1, 2$, simultaneously send two different OFDM pilot symbols defined by Equation (2.21), with zero mean and variance $\sigma_x^2 = 1$. The temporal estimation of $h(l)$ is found by minimizing the following MSE cost function [16]

$$\mathbb{C} \left(\left\{ \tilde{h}_j(l); j = 1, 2 \right\} \right) = \sum_{k=0}^{K-1} \left| \left(y(k) - \sum_{j=1}^2 \sum_{l=0}^{L_0-1} \tilde{h}_j(l) W_K^{kl} x_j(k) \right) \right|^2. \quad (4.1)$$

The basic approach of the algorithm defines the entries to the stacked vector, \mathbf{z} , and partitioned matrix, \mathbb{Q} , such that

$$z_j(l) \triangleq \sum_{k=0}^{K-1} y(k) x_j^*(k) W_K^{-kl} \quad (4.2)$$

and

$$q_{jj'}(l) \triangleq \sum_{k=0}^{K-1} x_j(k) x_{j'}^*(k) W_K^{-kl}, \quad (4.3)$$

where $j' = 1, 2$ and also denotes the transmit antenna number, the superscript $(\cdot)^*$ denotes the complex conjugate.

Vector \mathbf{z} and matrix \mathbb{Q} are given by [16]

$$\mathbf{z} \triangleq \begin{bmatrix} \mathbf{z}_1 \\ \mathbf{z}_2 \end{bmatrix} \quad (4.4)$$

and

$$\mathbb{Q} \triangleq \begin{bmatrix} \mathbb{Q}_{11} & \mathbb{Q}_{21} \\ \mathbb{Q}_{12} & \mathbb{Q}_{22} \end{bmatrix}, \quad (4.5)$$

where column vector \mathbf{z}_j and matrix $\mathbb{Q}_{jj'}$ are defined by

$$\mathbf{z}_j \triangleq [z_j(0), z_j(1), \dots, z_j(L_0 - 1)] \quad (4.6)$$

and

$$\mathbb{Q}_{jj'} \triangleq \begin{bmatrix} q_{jj'}(0) & q_{jj'}(-1) & \cdots & q_{jj'}(-L_0 + 1) \\ q_{jj'}(1) & q_{jj'}(0) & \cdots & q_{jj'}(-L_0 + 2) \\ \vdots & \ddots & \ddots & \vdots \\ q_{jj'}(L_0 - 1) & q_{jj'}(L_0 - 2) & \cdots & q_{jj'}(0) \end{bmatrix}, \quad (4.7)$$

for the first L_0 taps of the observed CIR.

Hence, vector $\tilde{\mathbf{h}}$ can be estimated by means of the time domain Wiener-Hopf equation as follows

$$\tilde{\mathbf{h}} = \mathbb{Q}^{-1}\mathbf{z}, \quad (4.8)$$

where $\tilde{\mathbf{h}}$ is the stacked vector that can be expressed in terms of antenna j as follows

$$\tilde{\mathbf{h}} \triangleq \begin{bmatrix} \tilde{\mathbf{h}}_1 \\ \tilde{\mathbf{h}}_2 \end{bmatrix}, \quad (4.9)$$

for column vectors $\tilde{\mathbf{h}}$ that are defined by

$$\tilde{\mathbf{h}}_j \triangleq [\tilde{h}_j(0), \tilde{h}_j(1), \dots, \tilde{h}_j(L_0 - 1)]. \quad (4.10)$$

In the described channel estimation method, matrix \mathbb{Q}^{-1} has to be calculated for size $2L_0 \times 2L_0$ and vector \mathbf{z} for length $2L_0$ every time when pilot symbols are sent. However, in WLANs the the training block is known to the receiver and therefore \mathbb{Q}^{-1} can be precalculated in advance. Furthermore, the estimation approach given by Equation (4.8) can be further simplified, when only significant taps of the CIR are identified out the first L_0 samples. This is shown in Fig. 4.1 for a 64-subcarrier OFDM that operates in HIPERLAN/2 channel A. The plot in Fig. 4.1(a) shows the observed CIR. The plot in Fig. 4.1(b) turns to zero all but the 5 significant taps of the CIR.

A number of significant taps choice depends on both the computational complexity and the required performance of the estimator. In systems with high SNRs, the estimation error of \mathbf{h}_j can be made small, but the estimation error of \mathbf{H}_j can mainly be caused by the leakage. Hence, the number of significant taps should be larger to

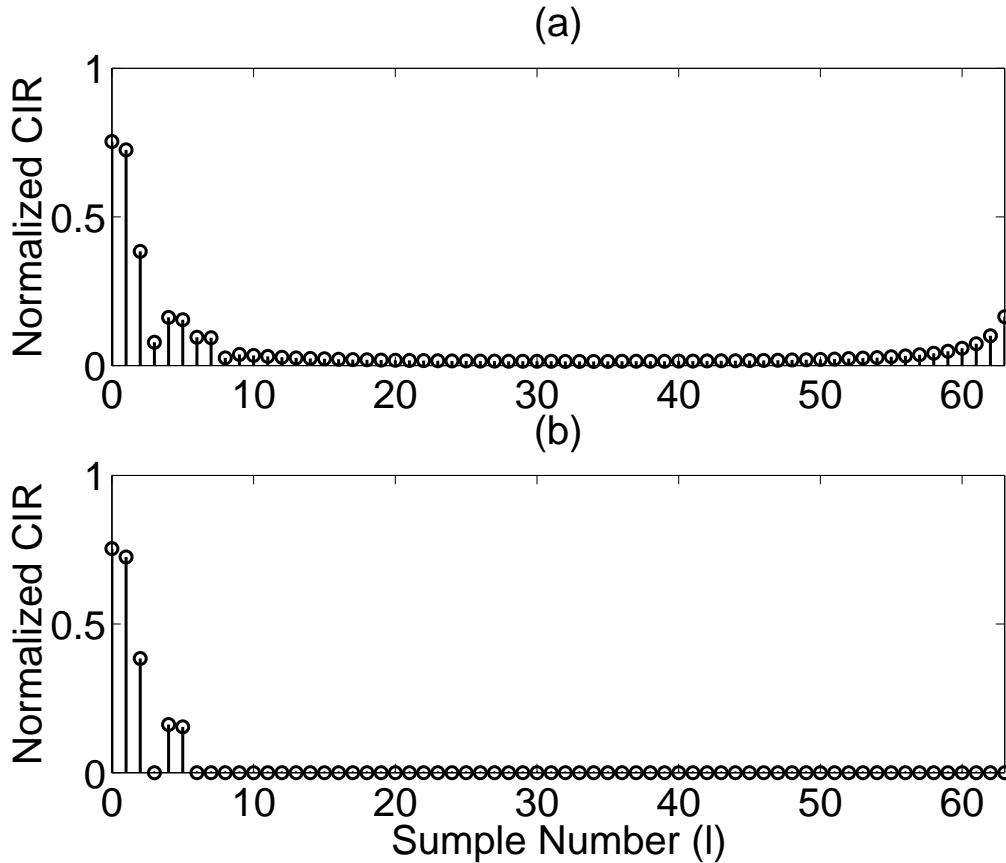


Figure 4.1: Significant tap catching technique in 64-subcarrier OFDM: (a) observed CIR of noiseless HIPERLAN/2 channel A; (b) 5 significant taps out the first L_0 .

reduce the leakage. On the contrary, for low SNRs, the relative estimation error for those taps with small amplitude, is very large; hence, the number of significant taps should be smaller [16].

Further improvement of channel estimation accuracy can be achieved in the temporal method by exploiting the time correlation of the channel (or in other words the correlation between different OFDM blocks i symbols apart), as proposed in [16].

4.1.2 Reduced Complexity Algorithm

The channel estimation algorithm evaluated in [19] is a reduced complexity algorithm of that described in the previous section, and based on the following assumption. The channel subcarrier responses are correlated. This is due to the limited delay spread of the channel and therefore subcarrier 2κ can be expressed in terms of subcarrier $(2\kappa + 1)$ such that [19]

$$H_j(2\kappa) = H_j(2\kappa + 1), \quad (4.11)$$

where $\kappa = 0, 1, \dots, K/2 - 1$.

The following variables are also defined such that

$$u_j(\kappa) \triangleq \frac{y(2\kappa)}{x_{3-j}(2\kappa)} - \frac{y(2\kappa + 1)}{x_{3-j}(2\kappa + 1)} \quad (4.12)$$

and

$$s_j(\kappa) \triangleq \frac{x_j(2\kappa)}{x_{3-j}(2\kappa)} - \frac{x_j(2\kappa + 1)}{x_{3-j}(2\kappa + 1)}. \quad (4.13)$$

With these, the elements of vector \mathbf{z}_j and matrix \mathbb{Q}_j are defined by

$$z_j(l) \triangleq \sum_{\kappa=0}^{K/2-1} u_j(\kappa) s_j^*(\kappa) W_{K/2}^{-2\kappa l}, \quad (4.14)$$

and

$$q_j(l) \triangleq \sum_{\kappa=0}^{K/2-1} |s_j(\kappa)|^2 W_{K/2}^{-2\kappa l}. \quad (4.15)$$

Hence, the CIR corresponding to antenna j can be estimated as follows [19]

$$\tilde{\mathbf{h}}_j = \mathbb{Q}_j^{-1} \mathbf{z}_j, \quad (4.16)$$

where matrix \mathbb{Q}_j^{-1} is of size $L_0 \times L_0$ and vector \mathbf{z}_j is of length L_0 , i.e. half the size of matrix \mathbb{Q}^{-1} and half the length of vector \mathbf{z} from Equation (4.8). Matrix \mathbb{Q}_j^{-1} is given by

$$\mathbb{Q}_j \triangleq \begin{bmatrix} q_j(0) & q_j(-1) & \cdots & q_j(-L_0 + 1) \\ q_j(1) & q_j(0) & \cdots & q_j(-L_0 + 2) \\ \vdots & \ddots & \ddots & \vdots \\ q_j(L_0 - 1) & q_j(L_0 - 2) & \cdots & q_j(0) \end{bmatrix}, \quad (4.17)$$

and vector \mathbf{z}_j is given by Equation (4.6). Therefore, the sizes of matrix inverse and FFTs required in the channel estimation given by Equation (4.16) are reduced by half [19].

Similar to the algorithm evaluated in [16], the complexity involved in the \mathbb{Q}_j^{-1} calculation can be further reduced by using only significant channel taps.

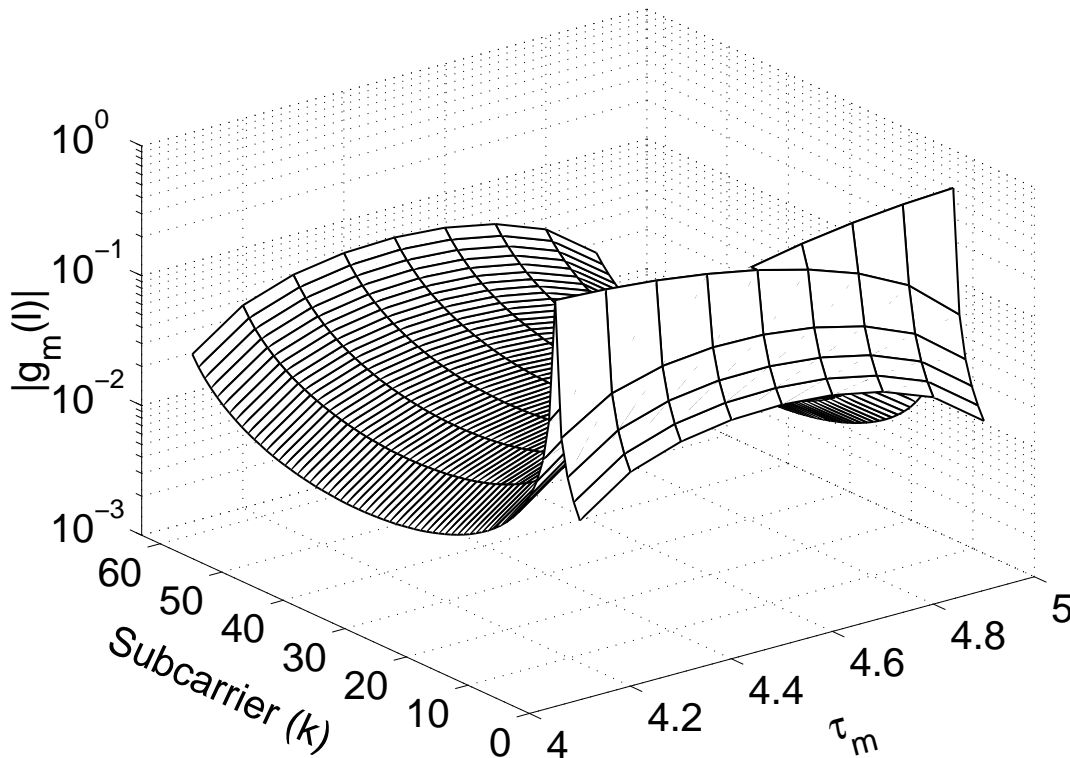


Figure 4.2: The leakage of a unity gain path zero due to non-sample spaced channel, $K = 64$ and $\beta = 4$.

In addition, in non-sample spaced channels a further improvement of the channel estimation accuracy has been achieved applying a pre-advancement of the timing point to the observed CIR for β samples [19]. The effect of pre-advancement for $\beta = 4$ samples is shown in Fig. 4.2 for a unity gain path zero that lies in delay interval ($0 < \tau_m < 1$).

This simple method results in less energy smearing of the total CIR energy outside the CP length compared with Fig. 2.2. Particularly, the use of $\beta = 4$ can reduce the total energy leakage from approximately -11 dB to -23 dB, depending on the actual delay interval, τ_m .

4.2 Frequency Domain Approach

The frequency domain channel estimation algorithm (that will be further analysed in Chapter 5) is also based on the correlation properties between the subchannels in OFDM that is because of the limited delay spread of the channel [57], [19]. Thus, interleaved OFDM pilot symbols in the frequency domain can be used for channel

estimation [72].

The pilot symbols in a 2×1 scheme for the frequency domain orthogonal preamble are defined by Equation (3.1) and shown in Fig. 2.7(a).

The corresponding frequency domain estimates of true, with no mismatch, $H_j(k)$ values are found by minimizing the following MSE cost function

$$\mathbb{C} \left(\left\{ \hat{H}_j(k); j = 1, 2 \right\} \right) = \sum_{j=1}^2 \sum_{k=0}^{K/2-1} \left| \hat{H}_j(2k + j - 1) - H_j(2k + j - 1) \right|^2. \quad (4.18)$$

Based on the initial LS estimation vector, $\tilde{\mathbf{P}}_j$, given by Equation (3.2), the fine channel estimation, $\hat{H}_j(k)$, is obtained by exploiting the frequency correlation of the channel parameters [17], [57]. This is accomplished by means of the LMMSE processing method, as the LMMSE performs both filtering and interpolation of the input LS estimation vector at once [85]-[87].

The LMMSE channel estimation vector, $\hat{H}_j(k)$, in OFDM using BPSK modulated subcarriers can be given by [4]

$$\hat{\mathbf{H}}_j \triangleq \mathbf{R}_{\mathbf{H}_j \tilde{\mathbf{P}}_j} \mathbf{R}_{\tilde{\mathbf{P}}_j \tilde{\mathbf{P}}_j}^{-1} \tilde{\mathbf{P}}_j = \left[\mathbf{R}_{\mathbf{H}_j \mathbf{P}_j} \left(\mathbf{R}_{\mathbf{P}_j \mathbf{P}_j} + \frac{1}{SNR} \mathbf{I} \right)^{-1} \right] \tilde{\mathbf{P}}_j, \quad (4.19)$$

where $\mathbf{R}_{\mathbf{H}_j \tilde{\mathbf{P}}_j} \triangleq \mathbf{R}_{\mathbf{H}_j \mathbf{P}_j}$ is the cross-correlation matrix between the channel attenuations, \mathbf{H}_j , and channel attenuations, \mathbf{P}_j , at the pilot positions. $\mathbf{R}_{\tilde{\mathbf{P}}_j \tilde{\mathbf{P}}_j} \triangleq \left(\mathbf{R}_{\mathbf{P}_j \mathbf{P}_j} + \frac{1}{SNR} \mathbf{I} \right)$ is the auto-correlation matrix of the channel attenuations, \mathbf{P}_j , at the pilot positions. \mathbf{I} is the identity matrix and SNR is the expected value of SNR [57].

In practice, the fixed weighting matrix, \mathbf{W}_j , in Equation (4.19) given by

$$\mathbf{W}_j \triangleq \mathbf{R}_{\mathbf{H}_j \tilde{\mathbf{P}}_j} \mathbf{R}_{\tilde{\mathbf{P}}_j \tilde{\mathbf{P}}_j}^{-1}, \quad (4.20)$$

needs to be calculated just once, based on expected values of SNR and τ_{rms} in channels with exponentially decaying power delay profile. Then, the coefficients of \mathbf{W}_j can be stored in a LUT [57]. In operation, the LMMSE channel estimation, $\hat{\mathbf{H}}_j$, can be obtained by simply multiplying the LUT's coefficient contents by the LS estimation vector, $\tilde{\mathbf{P}}_j$. Thus in a $Q \times 1$ diversity scheme, K/Q complex multiplications are required per one subchannel corresponding to transmit antenna j .

To further improve the channel estimation accuracy, the r.m.s. delay spread,

τ_{rms} , and SNR values can be estimated in real time, as it has been evaluated in Chapter 3. With these, more than one set of fixed weighting matrices can be pre-calculated in advance and stored in the LUTs. Then, after τ_{rms} and SNR estimation from the initial LS observation, the most appropriate fixed weighting matrix, \mathbf{W}_j , can be selected from a group of LUTs in order to obtain fine channel estimation using Equation (4.19).

The real time LMMSE channel estimation algorithm will be further analysed in Section 5.1.

4.3 Comparison of the Channel Estimation Methods

A frequency domain channel estimation method that solely optimises a CFR in the frequency domain can be thought of as a more relevant channel estimation approach in WLANs than a temporal method that optimises a CIR in the time domain. The latter approach requires the IDFT transformation of the observed CFR [57], [67]. The MSE cost function for the frequency domain and temporal channel estimation methods are given by Equations (4.18) and (4.1) respectively.

A frequency domain channel estimation method is a better choice in WLANs because of two limiting factors that affect a temporal method. These are the leakage problem in a non-sample spaced channel environment and null subcarriers that are generally used in OFDM-based WLANs. These are analysed below for a SISO OFDM as being common problems for any OFDM system with or without multiple antennas.

4.3.1 Leakage Problem

Consider a SISO OFDM system with no null subcarriers operating in a multipath channel with a CIR of unit power that is confined to the CP length. Then for a sample-spaced channel, a power relationship between the filtered CIR that is obtained by windowing out the first L_0 samples and the observed CIR before the windowing, can be written such that [20]

$$E \left\{ \sum_{l=0}^{L_0-1} |\tilde{h}(l)|^2 \right\} = E \left\{ \sum_{l=0}^{K-1} |\tilde{h}(l)|^2 \right\} = 1. \quad (4.21)$$

The observed CIR, $\tilde{h}(l)$, is obtained by the IDFT transformation of a noisy LS estimation vector $\tilde{\mathbf{H}}$. $\tilde{h}(l)$ in vector notation can be given by

$$\tilde{\mathbf{h}} = \frac{1}{K} \mathbf{F}^{-1} \tilde{\mathbf{H}}, \quad (4.22)$$

where the Fourier matrix, \mathbf{F} , is given by Equation (3.10) for $Q = 1$.

Windowing out the first L_0 channel impulse responses and transferring them back to the frequency domain will reduce the noise variance in the channel estimation to $N_0 \frac{L_0}{K}$ [66]. The windowing operation is given by

$$\tilde{h}(l) = \begin{cases} \tilde{h}(l) & 0 \leq l < L_0, \\ 0 & \text{elsewhere.} \end{cases} \quad (4.23)$$

On the other hand, the power relationship given by Equation (4.21) for a non-sample spaced channel becomes corrupted by leakage given by Equation (2.7), hence

$$E \left\{ \sum_{l=0}^{L_0-1} |\tilde{h}(l)|^2 \right\} < E \left\{ \sum_{l=0}^{K-1} |\tilde{h}(l)|^2 \right\}. \quad (4.24)$$

As a result of the windowing operation (Equation (4.23)), the lost CIR power in the right hand side of Equation (4.24) can cause degradation of the frequency domain channel estimation MSE. This is illustrated in Fig. 4.3.

As the CIR window size, L_0 , is increased, the leakage is reduced but the noise variance is raised. Thus, at high SNRs the non-sample spaced curves decrease MSE with the window size, while the sample-spaced curves increase MSE.

In Fig. 4.3, an equal power 2-ray multipath channel was simulated in the SISO OFDM system using 64 subcarriers (no null bins). The CIR lay within the CP length. One OFDM pilot symbol was sent through the channel and channel estimation was obtained by the DFT transformation of the measured (observed) CIR, $\tilde{h}(l)$, for various window sizes, L_0 . The simulator operated at fixed SNR values of 10 and 30 dB, at the sampling rate, $T_s = 50$ ns.

The frequency domain MSE performance is presented for both sample-spaced and

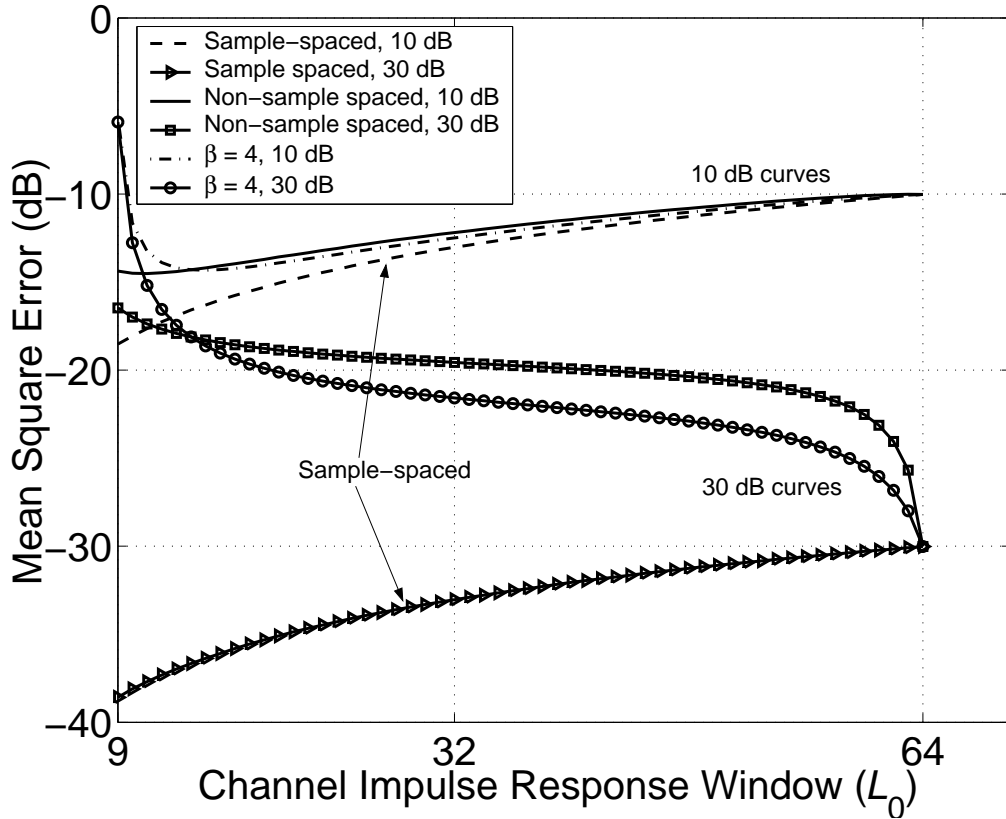


Figure 4.3: MSE vs CIR window size for a 2-ray channel in 64-subcarrier OFDM.

non-sample spaced channels with τ_{rms} of 100 ns and 112.5 ns respectively. In the non-sample spaced channel, the windowing operation leads to an irreducible estimation error, which dominates the performance for high SNRs (unless the window size, L_0 , is equal to the DFT length, $K = 64$, as shown in Fig. 4.3). In this case all the curves have the same performance (MSE = SNR of the channel).

The MSE performance can be improved in non-sample spaced channels, if a pre-advancement of the timing point, β , is used [19]. This is particularly effective at high SNRs as shown in Fig. 4.3 for $\beta = 4$.

It should be also noted that the leakage problem does not affect the estimation accuracy of the frequency domain channel estimation, as the frequency domain channel estimator is operating solely on the measured subcarriers in the frequency domain [57].

4.3.2 Null Subcarriers

Null subcarriers are often used in OFDM to meet the spectral regulations of a communication system, as for example in IEEE 802.11a and HIPERLAN/2 WLANs. 12 subcarriers including zero bin are set to zero in both standards out of 64 possible subchannels [38], [39]. These are summarised in Table 2.1.

When the total number of used subcarriers, K_{ts} , is less than the FFT length, K , then in general [67]

$$\text{trace} \left[E \left\{ \left(\tilde{\mathbf{H}} - \mathbf{H} \right) \left(\tilde{\mathbf{H}} - \mathbf{H} \right)^H \right\} \right] \neq \text{trace} \left[E \left\{ \left(\tilde{\mathbf{h}} - \mathbf{h} \right) \left(\tilde{\mathbf{h}} - \mathbf{h} \right)^H \right\} \right], \quad (4.25)$$

where $\tilde{\mathbf{H}}$ and $\tilde{\mathbf{h}}$ are defined in Equation (4.22) and \mathbf{h} denotes noiseless CIR.

Furthermore, the frequency domain channel estimation approach only operates on the K_{ts} subcarriers that will actually be used in the OFDM system, i.e. the null bins will not affect the estimation accuracy in a frequency domain method.

On the contrary, when a temporal estimation approach is used the null bins can lead to an accuracy loss of the CIR vector estimation, $\tilde{\mathbf{h}}$, which is obtained by the IDFT transformation of the measured CFR vector, $\tilde{\mathbf{H}}$.

To illustrate the performance degradation of a temporal channel estimation method caused by the null bins, the SISO OFDM input-output description can be rewritten in matrix notation as follows [20]

$$\mathbf{y} = \mathbf{X}\mathbf{F}\mathbf{h} + \mathbf{n}, \quad (4.26)$$

where \mathbf{X} is the diagonal matrix containing pilot symbols $x(k)$, given by

$$\mathbf{X} = \begin{bmatrix} x(0) & 0 & \dots & 0 \\ 0 & x(1) & \ddots & \vdots \\ \vdots & \ddots & \ddots & 0 \\ 0 & \dots & 0 & x(K-1) \end{bmatrix}, \quad (4.27)$$

and the Fourier matrix, \mathbf{F} , is given by Equation (3.10) (when $Q = 1$).

By analysing calculations of the received vector, \mathbf{y} , given by Equation (4.26), any zero value on the diagonal in Equation (4.27), will ‘erase’ a corresponding row entry in the CIR column vector, \mathbf{h} . Thus, $h(l)$ and $y(k)$ values corresponding to null

Table 4.1: Channel Estimation Complexity for a 2×1 Diversity Scheme

Method	Complex Multiplications
Full complexity temporal (Section 4.1.1)	$4L_0^2 + 4\text{FFT}_K$
Reduced complexity temporal (Section 4.1.2)	$2L_0^2 + 2\text{FFT}_{K/2} + 2\text{FFT}_K$
Frequency domain (Section 4.2)	K^2

bins cannot be seen by the receiver. This is particularly a problem in non-sample spaced channels, when after the sampling of the observed LS estimation vector, $\tilde{\mathbf{H}}$, the CIR energy leaks to all K taps. The CIR power smearing can further degrade the channel estimation accuracy when a temporal method is involved, requiring in fact the CIR measurement.

One way to improve the CIR estimation quality caused by the null-guard tones is a tone allocation on the null bins according to the average of measured subchannels that surround them. This is given by Equation (4.31). The tone allocation can reduce the transient effect when DFT processing is involved [30].

4.3.3 Complexity Analysis

For a packet type OFDM system the training symbols are known at the receiving end. Hence, the required matrix inversion can be precalculated in advance for all three channel estimation algorithms. The complexity involved in channel estimation computation will be presented in terms of required complex multiplications for BPSK modulated pilot signals. K -point FFT has a computation order of $(K/2) \log_2(K)$ [88]. As the exact complexity can vary depending on the FFT implementation, FFT_K will be used as the complexity expression rather than the number of complex multiplications. Also, the complexity of the frequency domain channel estimation algorithm will be presented for a single set of precalculated fixed weighting matrix coefficients. This is summarised in Table 4.1 for the three channel estimation algorithms in a 2×1 diversity scheme that employs two sets of channel estimation vectors $\hat{\mathbf{H}}_j$. It should be also noted that for both temporal channel estimation methods, a final K -point FFT is required for obtaining the frequency domain channel estimation vector, $\hat{\mathbf{H}}_j$, given by Equation (4.30) as equalisation is performed in the frequency domain.

For example, when using BPSK modulated pilot signals the required number of complex multiplications for $K = 64$ and $L_0 = 16$ is given as follows

$$4L_0^2 + 4\text{FFT}_K = 4 \cdot 16^2 + 4 \cdot (64/2) \cdot \log_2(64) = 1792,$$

$$2L_0^2 + 2\text{FFT}_{K/2} + 2\text{FFT}_K = 2 \cdot 16^2 + 2 \cdot (32/2) \cdot \log_2(32) + 2 \cdot (64/2) \cdot \log_2(64) = 1056,$$

$$K^2 = 64^2 = 4096.$$

In this example, it turns out that the frequency domain channel estimation algorithm is the most complex in terms of the required complex multiplications. A complexity reduction for the LMMSE channel estimator will be evaluated in the following chapters.

4.4 Numerical Results

The frequency domain channel estimation MSE performance for BPSK, averaged over 2000 OFDM pilot symbol blocks, was evaluated for three channel estimation algorithms described in Sections 4.1 and 4.2.

The simulations were carried out in HIPERLAN/2 non-sample spaced channels A and C for a 2×1 diversity scheme within the 802.11a framework, with OFDM parameters given in Table 2.1. Perfect SNR, maximum excess delay τ_x and r.m.s. delay spread τ_{rms} knowledge were assumed at the receiving end and the total transmit power was normalised to unity.

The frequency domain channel estimation MSE, $\hat{\mathbf{H}}_j$, corresponding to antenna j is given by [35]

$$MSE_j \triangleq \frac{1}{K} \text{trace}[\mathbf{\Psi}_j], \quad (4.28)$$

where $\mathbf{\Psi}_j$ is the auto-covariance matrix of the estimation error corresponding to antenna j , given by

$$\mathbf{\Psi}_j \triangleq E \left\{ \left(\hat{\mathbf{H}}_j - \mathbf{H}_j \right) \left(\hat{\mathbf{H}}_j - \mathbf{H}_j \right)^H \right\}. \quad (4.29)$$

For two temporal algorithms, vector $\hat{\mathbf{H}}_j$ was obtained by the DFT transformation of the CIR estimates given by Equations (4.9) and (4.16) respectively as follows

$$\hat{\mathbf{H}}_j = \mathbf{F}\tilde{\mathbf{h}}_j. \quad (4.30)$$

where the Fourier matrix, \mathbf{F} , is given by Equation (3.10) (when $Q = 1$) and vector \mathbf{h}_j was extended to length K using zero padding.

Two long OFDM pilot symbols were simultaneously sent from each of two transmit antennas through a fading multipath channel 1000 times. For each iteration, a new channel was randomly generated and remained constant over the length of the two consecutive symbols.

The *basic* pilot symbol structure, shown in Fig. 2.7(a), was used for the frequency domain channel estimation algorithm. The number of significant taps, L_0 , was chosen such that $L \geq L_0 \geq \tau_x$ in both algorithms using the temporal approach. In addition, the null-guard tones were set according to the average of adjacent measured subcarriers to reduce transient effect for both temporal methods, given by

$$y(k) = \begin{cases} (y(1) + y(63))/2 & k = 0; \\ (y(26) + y(38))/2 & k = 27, 28, \dots, 37. \end{cases} \quad (4.31)$$

Before processing, using one or another temporal channel estimation algorithms, the average of the two consecutive pilot symbols was obtained at the receiving end. The averaged received vector, $\tilde{\mathbf{y}}$, is given by

$$\tilde{\mathbf{y}} = \frac{1}{2}(\mathbf{y}(0) + \mathbf{y}(1)), \quad (4.32)$$

for $i = 0, 1$.

The LS estimation of the frequency domain channel estimation for the *basic* pilot scheme is given by Equation (3.2).

Fig. 4.4 presents simulation results for channel A revealing that the frequency domain channel estimation algorithm is a better performing channel estimation technique when the channel is non-sample spaced.

L_0 was set to 18 samples for both full and reduced complexity temporal methods as a trade-off between the noise reduction by a factor of L_0/K at low SNRs and

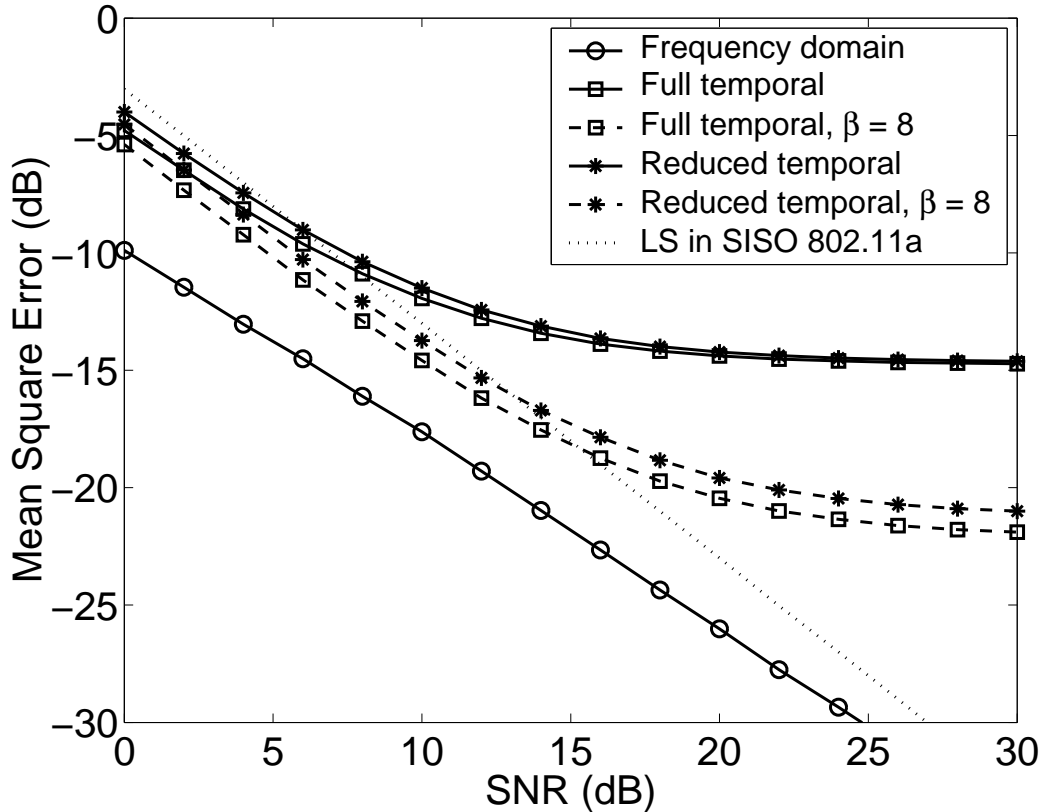


Figure 4.4: MSE performance of three channel estimation algorithms in HIPER-LAN/2 channel A.

estimation accuracy at high SNRs. Poorer performance of both methods is mainly because of the CIR power smearing. In addition, the presence of the null bins affects the estimation accuracy of the temporal algorithms. Pre-advancement of the timing point, $\beta = 8$, was also used to extend L_0 (refer to Fig. 3.3) that improved the MSE error floor for both temporal techniques. In particular, the improvement is almost 7 dB for the full complexity algorithm, as shown in Fig. 4.4. The extended L_0 for β samples also contributes to the channel estimation performance improvement at high SNRs.

Fig. 4.4 also presents the MSE performance for a simple LS estimation in SISO 802.11a using an average of the two consecutive pilot symbols (given by Equation (3.2) for $Q = 1$). As a result of averaging, the MSE of the channel estimation is 3 dB better than the expected MSE of data in SISO scheme. The ‘LS in SISO 802.11a’ curve is also plotted in Fig. 4.5 for a reference.

As the delay spread of a multipath channel increases, the coherence bandwidth of the channel decreases and the MSE irreducible error floor rises for the reduced com-

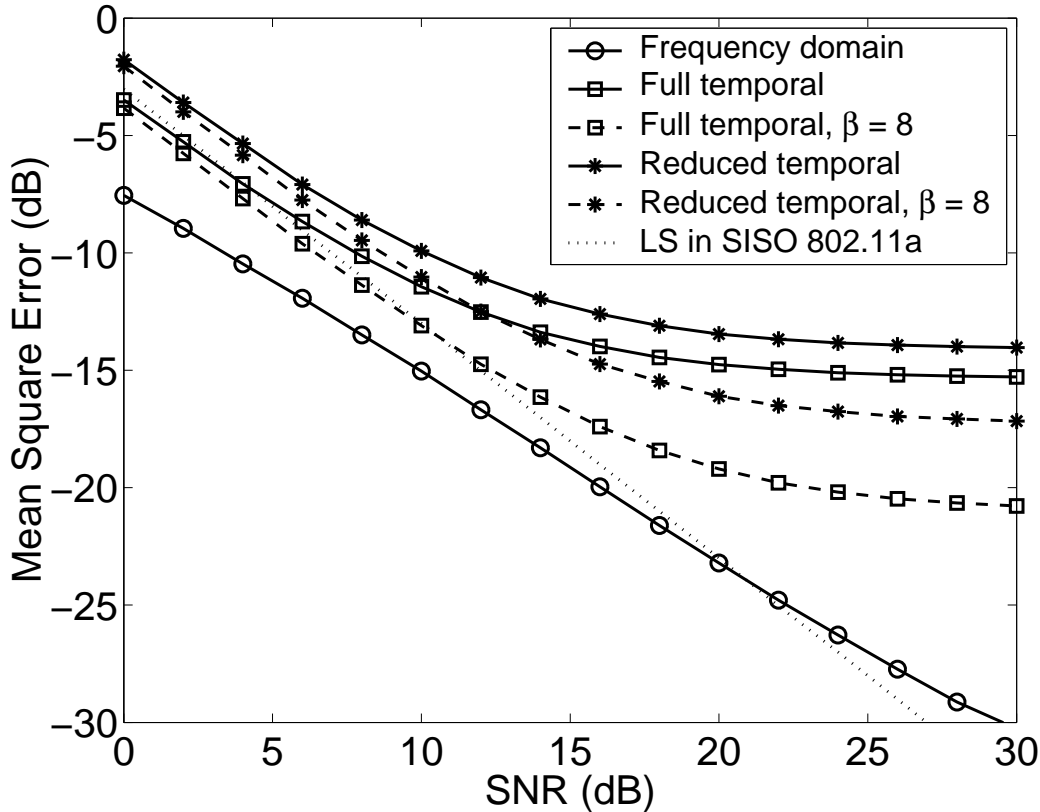


Figure 4.5: MSE performance of three channel estimation algorithms in HIPER-LAN/2 channel C.

plexity temporal algorithm and also for the frequency domain algorithm that uses interleaved subcarriers. Both algorithms become affected by the reduced correlation between the measured subcarriers in channel C as shown in Fig. 4.5.

Despite the increased L_0 to 24 samples for the temporal methods, the frequency domain algorithm is still a better performing channel estimation technique (and especially at high SNRs), as shown in Fig. 4.5. This would indicate that the gain over a temporal approach, which is due to the leakage problem and null-guard tones, outweighs the interpolation error that is due to the *basic* pilot symbol structure that uses interleaved subcarriers in the frequency domain.

A temporal approach does outperform the frequency domain method when energy leakage and null-guard tones are not present. This is shown in Fig. 4.6 by the MSE performance for BPSK OFDM, averaged over 1000 pilot blocks, with $K = 64$ and CP of $0.8 \mu\text{s}$. The simulations were carried out in a sample-spaced equal power 2-ray channel with $\tau_{rms} = 50 \text{ ns}$ ($L_0 = 3$).

As shown in Fig. 4.6, both temporal algorithms outperform the frequency do-

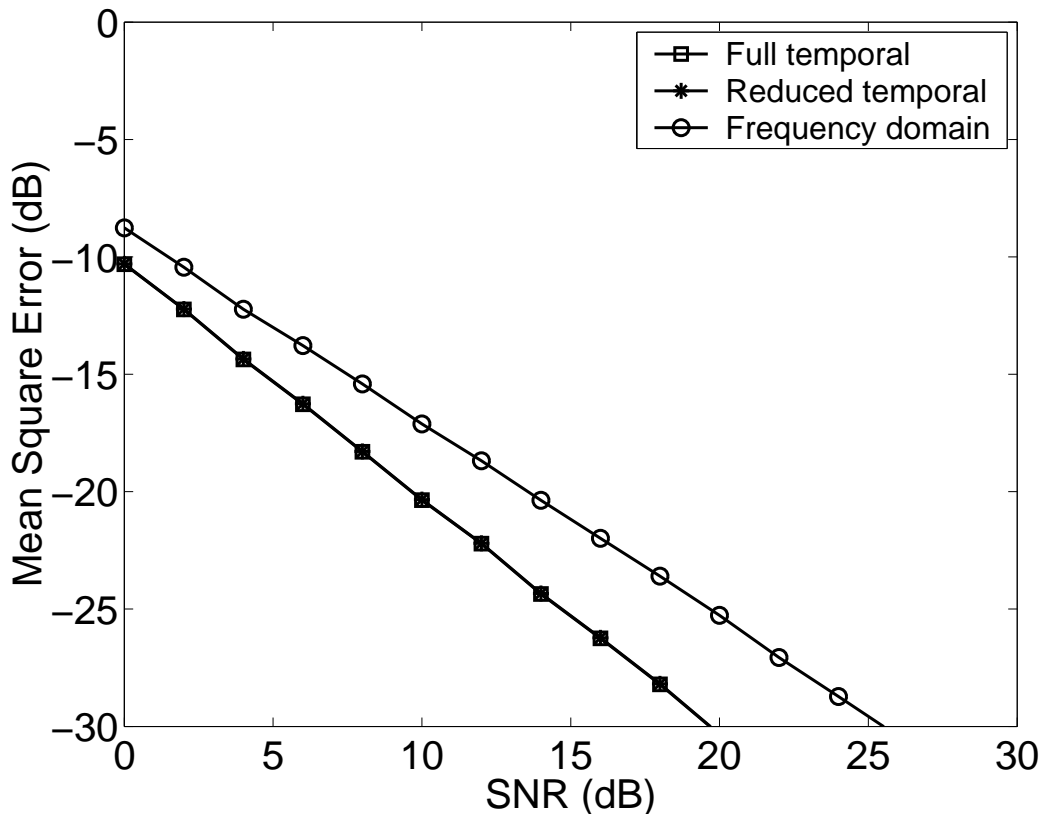


Figure 4.6: MSE performance of three channel estimation algorithms in a sample-spaced equal power 2-ray channel with $\tau_{rms} = 50$ ns.

main method, particularly at high SNRs that is mainly because of the noise reduction by a factor of L_0/K .

4.5 Summary

In this chapter, the frequency domain MSE of three channel estimation algorithms was analysed in WLANs with transmitter diversity for in an indoor, rich scattering channel environment. Two algorithms used a temporal approach (often called DFT-based) for channel estimation, whereas the third algorithm used a frequency domain approach. A temporal algorithm is a better performing estimation technique in sample-spaced channels, especially if a significant tap catching approach is employed. The latter reduces the CIR window size to a length of $L_0 \ll K$ and therefore the channel estimation noise variance by a factor of L_0/K . However, communication channels are generally non-sample spaced and this can cause CIR energy leakage outside of the first L_0 samples and across the entire K -point DFT length. Thus, the

CIR windowing leads to the CIR energy loss for a temporal estimation technique and hence causes an irreducible MSE error floor at high SNRs. In addition, WLANs generally use null-guard tones that can degrade the accuracy in CIR measurement by the IDFT transformation, which can further degrade the MSE performance of a temporal method. On the other hand, the frequency domain algorithm with interleaved subcarriers can be affected by interpolation errors in dispersive channels that can also cause MSE degradation. This is especially true for high diversity orders in multipath channels with large delay spreads.

In a 2×1 diversity scheme with 802.11a pilot symbol overhead, the frequency domain channel estimation algorithm appears to be a better choice for practical scenarios based on HIPERLAN/2 channel models. However, this algorithm is the most complex compared to two others in terms of the required complex multiplications. The complexity reduction for the LMMSE channel estimator will be evaluated in the following chapters.

Chapter 5

LMMSE Channel Estimation in WLANs with Transmitter Diversity

In the previous chapter, it has been shown that a frequency domain channel estimation method is a better choice in MISO WLANs than a temporal approach. This chapter further evaluates this idea and presents a simple way in which the LMMSE channel estimation can be adopted to cater for the changing channel environments and which avoids an auto-correlation matrix inversion [58]. LMMSE complexity forces practical systems to preprocess the fixed weighting matrix for a single set of fixed values of SNR and r.m.s. delay spread in channels with an exponentially decaying power delay profile [57]. In the following section near LMMSE performance of the channel estimation is obtained by measuring the SNR and τ_{rms} of the channel. Given SNR and τ_{rms} estimates, the most appropriate fixed weighting matrix can be selected from a group of LUTs precalculated in advance, based on combinations of expected values for SNR and τ_{rms} . Three LUTs are found to be sufficient for practical intents.

Furthermore, LMMSE channel estimation is analysed for the three pilot symbol structures introduced in Chapter 2. The channel estimation accuracy and complexity are compared to a reduced complexity LMMSE with a low rank approximation by SVD. This work has been published in the journal “*Wireless Personal Communications*”, Kluwer.

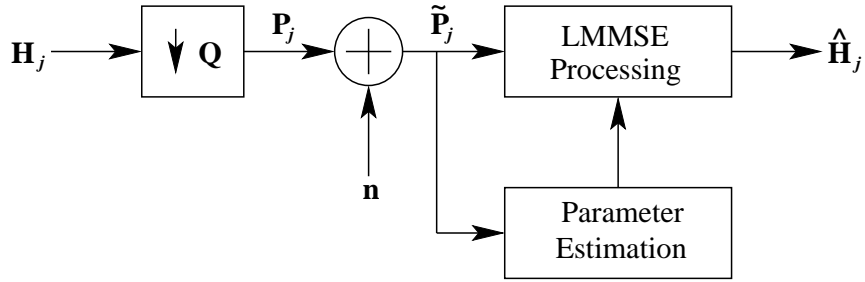


Figure 5.1: A simplified model for a real time LMMSE channel estimation in MISO OFDM.

5.1 Real Time LMMSE Channel Estimation

5.1.1 Processing Model

Recalling the previous chapter, LMMSE is a conditional mean estimator that requires prior statistical knowledge of channel parameters. The channel parameters are changing depending on environment and also due to the motion of people and objects in time. LMMSE complexity imposes a practical solution to precalculate a fixed weighting matrix, \mathbf{W}_j , given by Equation (4.20) in advance, based on the expected SNR and τ_{rms} values (for a channel with an exponential power delay profile). To further enhance the LMMSE channel estimation performance, the latter parameters can be estimated in real time for selection of an appropriate LUT that contains the precalculated coefficients of \mathbf{W}_j .

A simplified model for a real time LMMSE channel estimation in MISO OFDM that uses interleaved subcarriers in the frequency domain is shown in Fig. 5.1.

The LMMSE channel estimation vector, $\hat{\mathbf{H}}_j$, is expressed in terms of the ideal channel estimation vector, \mathbf{H}_j , given the LS estimation vector, $\tilde{\mathbf{P}}_j$, at the pilot positions. Mathematically it can be described by

$$\hat{\mathbf{H}}_j = E \left\{ \mathbf{H}_j | \tilde{\mathbf{P}}_j \right\}. \quad (5.1)$$

As shown in Fig. 5.1, vector \mathbf{P}_j is determined by vector \mathbf{H}_j decimated in the frequency domain by a factor of Q (which also represents the transmit diversity order in MISO OFDM). \mathbf{n} is the additive complex Gaussian noise with zero mean and variance N_0 that symbolises the channel noise.

The model illustrates the effect of the interleaving of the OFDM pilot symbols in

the frequency domain, representing the measured subsets, $\tilde{\mathbf{P}}_j$, each of length K/Q . LMMSE processing performs filtering and interpolation of the noisy LS observation, $\tilde{\mathbf{P}}_j$, to obtain the fine channel estimation vector, $\hat{\mathbf{H}}_j$, of length K corresponding to transmit antenna j .

An exact expression for the LMMSE processing in MISO OFDM is given by Equation (4.19). The statistical channel parameter estimation, shown in Fig. 5.1 by a block ‘Parameter Estimation’, are also obtained in real time based on the initial LS estimation vector, $\tilde{\mathbf{P}}_j$. These have been evaluated in Chapter 3.

5.1.2 An MSE Goal

For good channel estimation, it is necessary to reduce the MSE to a level where it has an insignificant effect on the BER performance of the system. That is, the error in the channel estimation should be significantly less than the MSE on the data symbols. The dashed line in Fig. 5.3 shows the expected MSE on a data symbol for a given SNR. The line also shows the expected MSE performance of an LS channel estimate (that uses a single pilot symbol). If the LS channel estimate was to be used to equalise the data symbol, then the resulting output would include both errors causing a 3 dB performance loss compared to theoretical coherent detection. The performance would be almost the same as differential detection. To justify coherent detection the channel estimation MSE should be below the expected SNR on data.

More generally

$$MSE(demodulation) = MSE(data) + MSE(\hat{\mathbf{H}}_j) \quad (5.2)$$

and

$$MSE(degradation) = \frac{MSE(demodulation)}{MSE(data)} = 1 + \frac{MSE(\hat{\mathbf{H}}_j)}{MSE(data)}. \quad (5.3)$$

Fig. 5.2 plots the degradation given by Equation (5.3) versus $\frac{MSE(data)}{MSE(\hat{\mathbf{H}}_j)}$ and shows that improving $MSE(\hat{\mathbf{H}}_j)$ gives a diminishing return in overall performance. This is doubly so when one considers complexity which goes up as $\frac{MSE(\hat{\mathbf{H}}_j)}{MSE(data)}$ gets

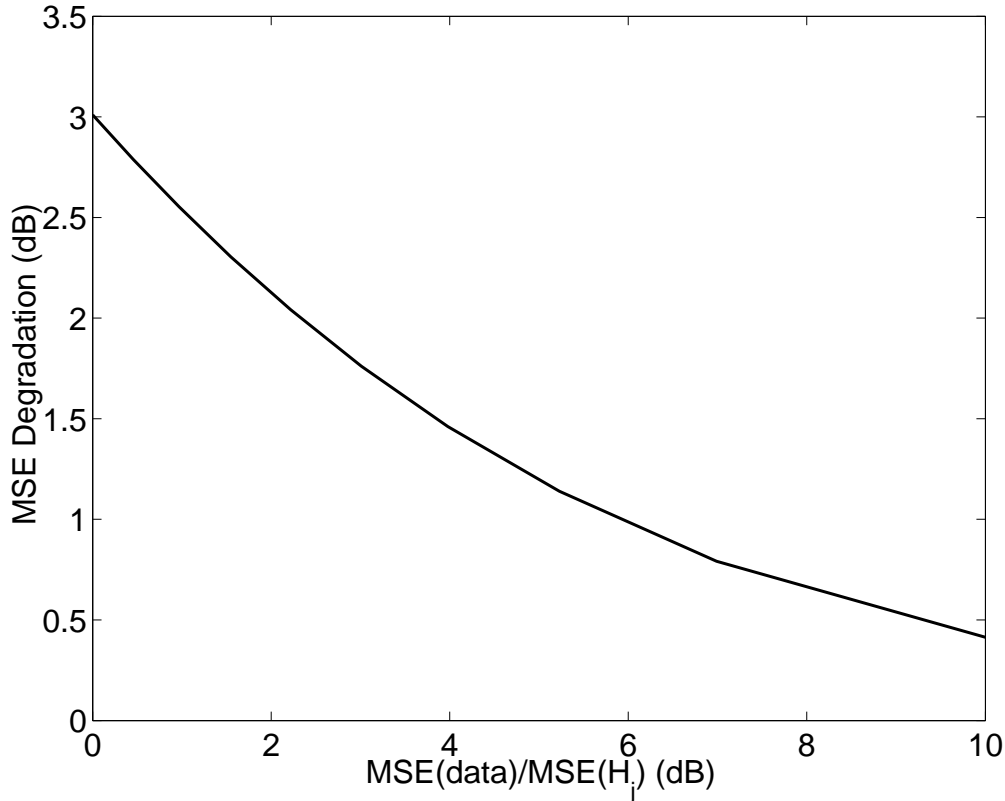


Figure 5.2: MSE degradation of data due to channel estimation error.

smaller.

An $\frac{MSE(\hat{\mathbf{H}}_j)}{MSE(data)}$ between -3 dB and -6 dB will respectively produce an overall performance within 1.8 dB to 1 dB of theoretical coherent detection. It will be shown later that this is quite a challenge for MISO systems operating at high SNRs. The fine dotted line in Fig. 5.3 shows the condition $\frac{MSE(\hat{\mathbf{H}}_j)}{MSE(data)} = -3$ dB. It also represents the LS performance of double length pilots in a SISO environment. This will be used later to define the boundary between acceptable and non-acceptable channel estimation performance.

5.1.3 Numerical Results

The real time LMMSE channel estimation in MISO OFDM was simulated in a 2×1 diversity scheme within the 802.11a framework. The performance was evaluated based on the channel estimation MSE given by Equation (4.28) and BER. The MSE performance was evaluated as follows.

Two long pilot symbols (refer to Fig. 2.3) were simultaneously sent on interleaved subcarriers from each of two transmit antennas using the *basic* pilot scheme shown

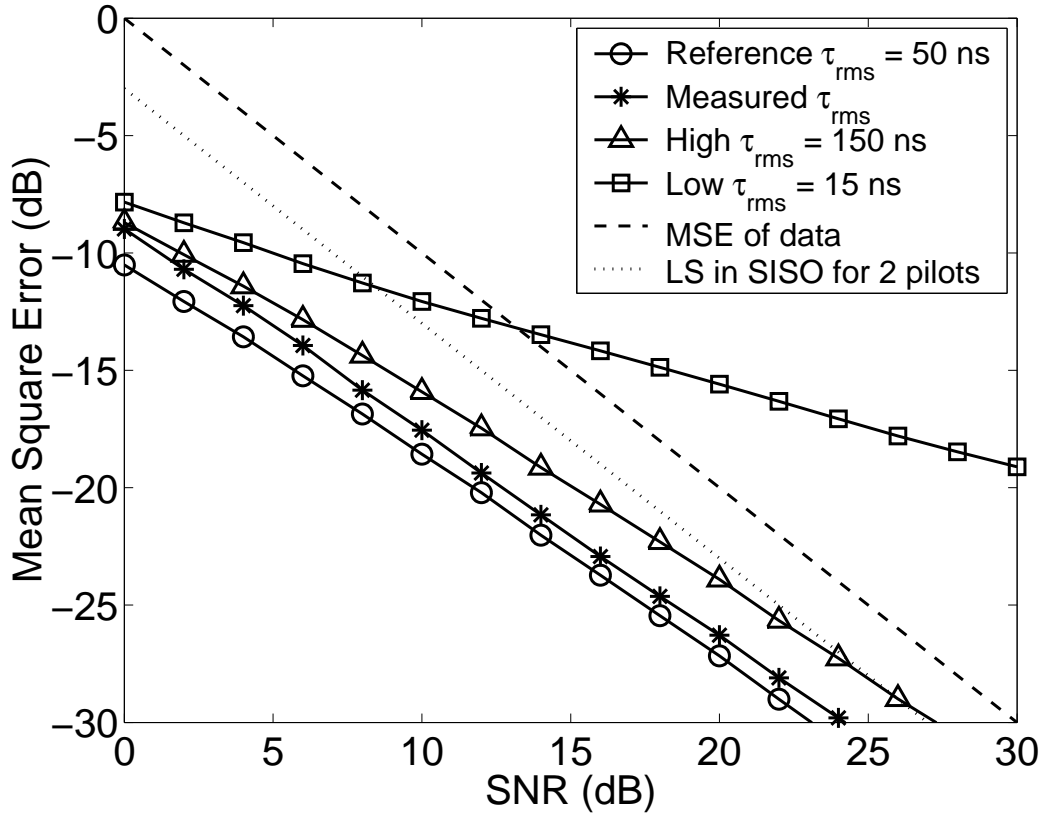


Figure 5.3: Effect of τ_{rms} selection on channel estimation error in HIPERLAN/2 channel A ($\tau_{rms} = 50$ ns) with 2×1 diversity scheme.

in Fig. 2.7(a). HIPERLAN/2 channels A and C (refer to Table 2.2) were used in simulations. τ_{rms} was measured using Equation (3.19) and SNR was measured using Equation (3.8). The initial LS estimation vector, $\tilde{\mathbf{P}}_j$, was obtained by means of Equation (3.2).

A perfect knowledge of SNR was available for the group of curves in Fig. 5.3 and Fig. 5.4 to enable performance comparison of LMMSE for r.m.s. delay spread measurement in real time. A perfect knowledge of r.m.s. delay spread of the power delay profile, τ_{rms} , was available for the group of curves in Fig. 5.5 and Fig. 5.6 to enable performance comparison of LMMSE for SNR measurement in real time.

In Fig. 5.3, the ‘Reference $\tau_{rms} = 50$ ns’ curve shows LMMSE channel estimation performance with perfect knowledge of both SNR and τ_{rms} in channel A.

LMMSE channel estimation, enhanced with IFFT measurement of τ_{rms} , has a performance close to the reference curve (with an MSE loss of ≈ 1 dB at SNR = 20 dB) except for low SNRs, where the τ_{rms} measurement becomes corrupted by the noise (refer to Fig. 3.8).

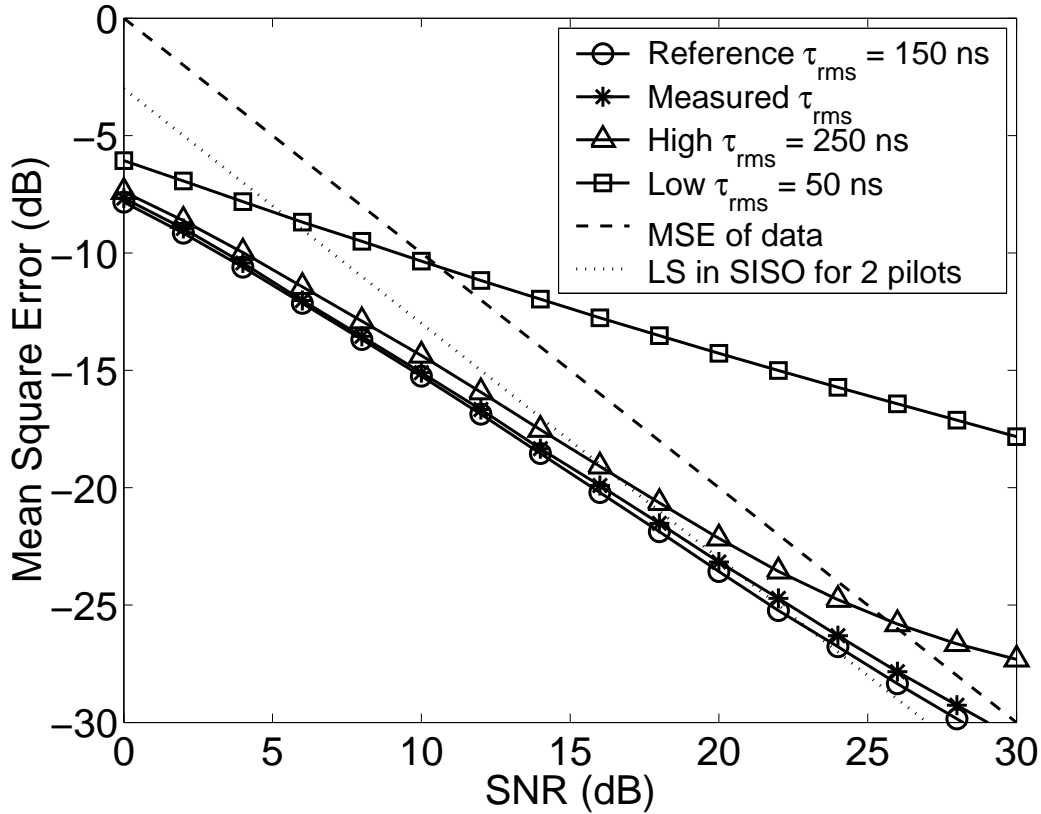


Figure 5.4: Effect of τ_{rms} selection on channel estimation error in HIPERLAN/2 channel C ($\tau_{rms} = 150$ ns) with 2×1 diversity scheme.

Using a fixed r.m.s. delay spread value, high or low, for all cases is clearly not optimum and this can degrade the channel estimation MSE, as shown in Fig. 5.3 by the ‘High $\tau_{rms} = 150$ ns’ and the ‘Low $\tau_{rms} = 15$ ns’ curves. MSE performance can be improved by the correct choice of the r.m.s. delay spread of the power delay profile. The figure indicates it is best to overestimate τ_{rms} than underestimate τ_{rms} .

The same conclusion also holds for channel C as shown in Fig. 5.4.

However, due to a longer delay spread in channel C (150 ns), the interpolation error is increased that causes rise of all MSE curves compared with the MSE performance for channel A (Fig. 5.3). This is because of the reduced coherence bandwidth of channel C. The increased interpolation error also explains the reduced MSE of the ‘Measured τ_{rms} ’ curve compared to the ‘Reference $\tau_{rms} = 150$ ns’ curve in Fig. 5.4, as the increased interpolation error dominates the performance. It should be noted that acceptable performance of $MSE(\hat{\mathbf{H}}_j) < -3$ dB is not achieved for SNRs higher than 24 dB even for the ideal reference curve. This is the limit of the LMMSE processing.

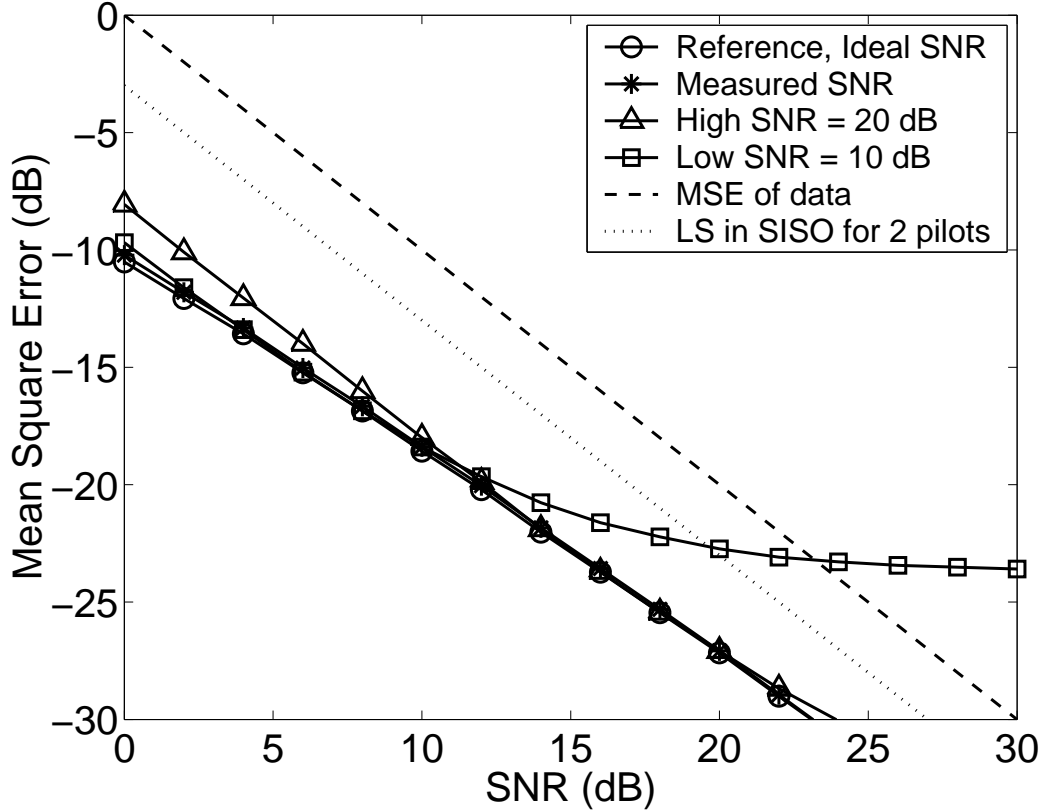


Figure 5.5: Effect of SNR selection on channel estimation error in HIPERLAN/2 channel A ($\tau_{rms} = 50$ ns) with 2×1 diversity scheme.

The IFFT measurement of the τ_{rms} is sufficiently accurate at high SNRs, as shown in Fig. 3.8 and Fig. 3.9, and to avoid complex matrix inversion a number of fixed weighting matrix coefficient tables can be precalculated for a set of the r.m.s. delay spreads. These tables can be switched by the measured τ_{rms} , when a close match occurs between the measured and one of expected τ_{rms} values from the set of LUTs. Furthermore, for low SNRs the τ_{rms} measurement becomes poor and thus, the τ_{rms} measurement should be avoided. Instead, an expected value of τ_{rms} can be used based on near worst case of the channel parameters.

It should be also noted from Fig. 5.3 and Fig. 5.4 that LMMSE processing produces larger MSE errors, when τ_{rms} is chosen too low compared to the actual r.m.s. delay spread in the channel. This is shown by ‘Low $\tau_{rms} = 15$ ns’ and ‘Low $\tau_{rms} = 50$ ns’ curves in Fig. 5.3 and Fig. 5.4 respectively. However, in non-sample spaced channels the observed CIR generally produces larger r.m.s. delay spread estimation than the actual (refer to Fig. 3.8 and Fig. 3.9) due to the CIR power smearing after the sampling of the CFR.

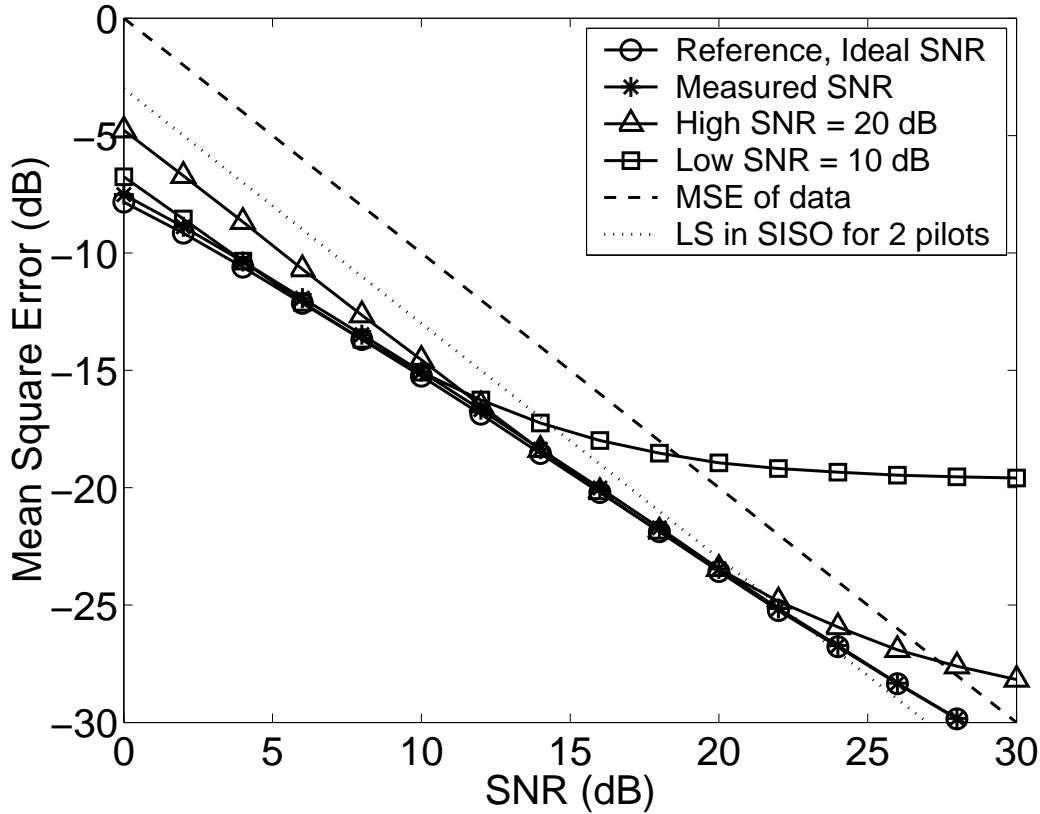


Figure 5.6: Effect of SNR selection on channel estimation error in HIPERLAN/2 channel C ($\tau_{rms} = 150$ ns) with 2×1 diversity scheme.

Thus, when the SNR condition of the channel is poor, a good choice for expected τ_{rms} would be a value which represents the medium to high (near worst case) expected r.m.s. delay spread. When the SNR is high, a choice of one low or one high expected τ_{rms} would be sufficient for practical intents (it will be shown later in this section), depending on measured r.m.s. delay spread in the channel.

Fig. 5.5 shows the effect of using fixed values for SNR and ideal r.m.s. delay spread knowledge in channel A. A choice of SNR = 20 dB is adequate for all SNRs that are above 10 dB. Below that a lower SNR value should be chosen, for example 10 dB as shown in Fig. 5.5. If the expected SNR is chosen too low, the MSE error floor can cause the performance degradation at high SNRs as shown in Fig. 5.5. On the contrary, if the SNR is chosen too high the MSE gain can be lost at low SNRs, although this is far less problematic.

The same conclusion also holds for channel C as shown in Fig. 5.6. Two values of SNR, 10 dB and 20 dB, can be sufficient to achieve an adequate performance of the estimator by switching between the corresponding coefficient LUTs (refer to

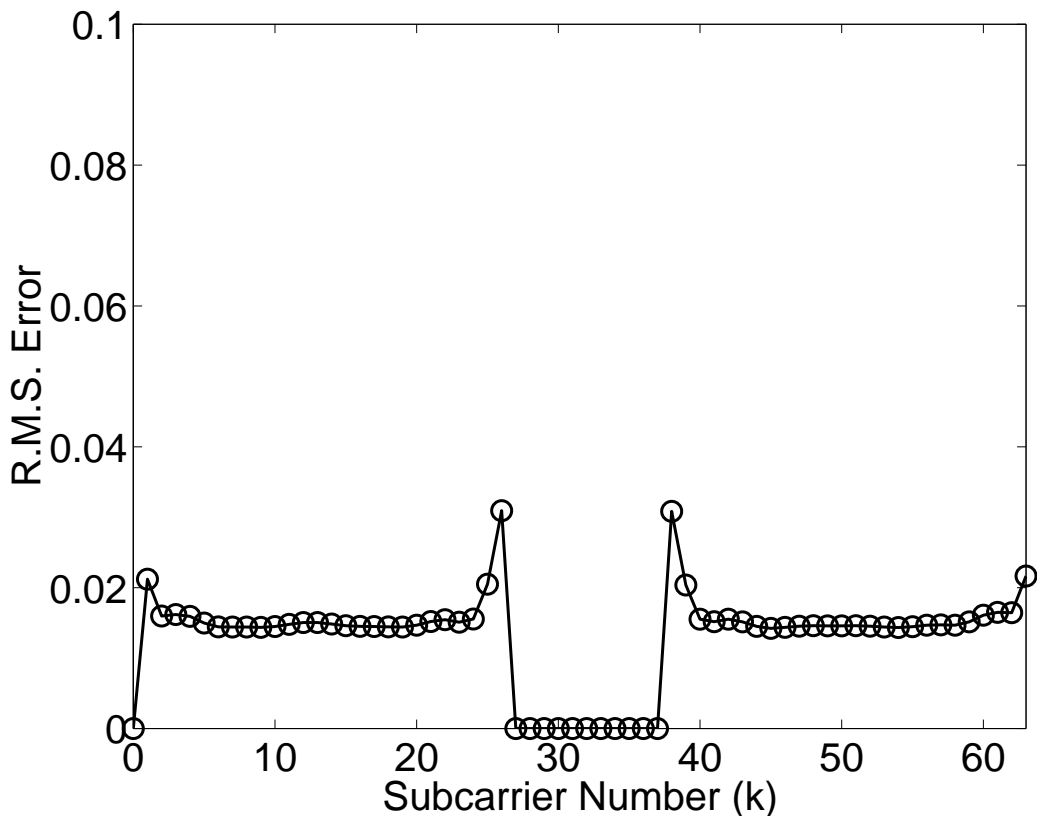


Figure 5.7: Effect of interpolation errors in channel A at SNR = 40 dB.

Fig. 5.10). It should be also noted that because of longer delay spreads in channel C, the interpolation error is increased causing a rise of all MSE curves in Fig. 5.6 compared with the MSE performance for channel A (Fig. 5.5).

Frequency domain filters such as the LMMSE do not give a uniform MSE performance across all frequency bins. Fig. 5.7 illustrates the effect of interpolation errors in channel A at a fixed value of SNR = 40 dB, when the ideal SNR and r.m.s. delay spread knowledge were assumed. The errors are shown for each of 52 active subcarriers, with the largest errors being in the outside bins. The latter is a typical phenomenon of this kind of interpolation as the edge frequency bins are not surrounded by the measured subchannels [4].

Fig. 5.8 also presents the effect of interpolation errors for channel C at a fixed value of SNR = 40 dB and ideal SNR and τ_{rms} knowledge. Because of the longer delay spread of channel C, the edge errors are more evident compared with channel A (Fig. 5.7), caused by the increased interpolation error in the channel with a reduced coherence bandwidth.

The edge errors are the dominant cause of the MSE error floor at high SNRs (for

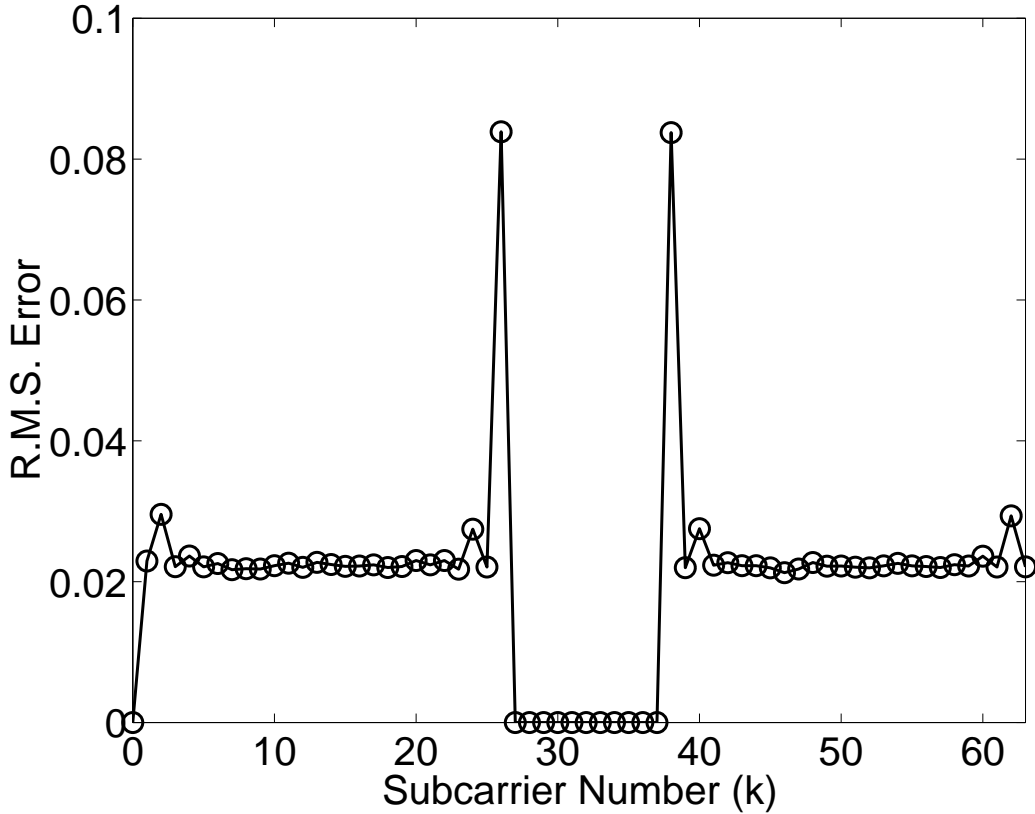


Figure 5.8: Effect of interpolation errors in channel C at SNR = 40 dB.

SNRs greater than 30 dB in the analysed scenario and therefore not seen in Fig. 5.3 – Fig. 5.6). The floor can be lowered by neglecting the edge bins (bin 26 and 38 in Fig. 5.7 and Fig. 5.8). Alternatively, lower constellation densities can be applied for these subchannels.

As shown in Fig. 5.3 – Fig. 5.6, the measurement of the r.m.s. delay spread and SNR in real time can further improve the LMMSE channel estimation accuracy. The accuracy depends on a number of LUTs used in the processor. From the simulation results for MISO 802.11a in HIPERLAN/2 channels, a minimum of three LUTs are required for achieving an adequate estimation accuracy for practical intents.

The system was tested in 3 environments (HIPERLAN/2 NLOS channels A, B

Table 5.1: Switching Parameters

SNR	τ_{rms}	Design parameters for LUT
< 10 dB	all	SNR = 10 dB; τ_{rms} = 125 ns
≥ 10 dB	< 75 ns	SNR = 20 dB; τ_{rms} = 50 ns
≥ 10 dB	≥ 75 ns	SNR = 20 dB; τ_{rms} = 125 ns

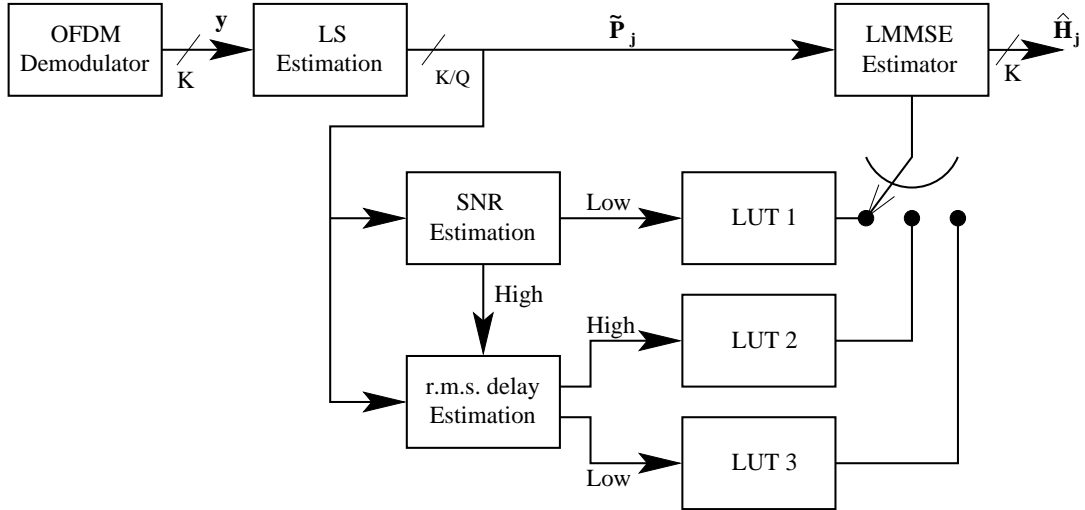


Figure 5.9: Real time LMMSE channel estimator.

and C) with CIR confined to the CP length. The switching parameters between the LUTs are summarized in Table 5.1, and chosen based on the simulation results shown in Fig. 5.10. A block diagram is shown in Fig. 5.9.

As shown in Fig. 5.10, an LMMSE processor based on the LUT selection under ideal condition (SNR and τ_{rms} are perfectly known) gives an adequate performance in all three channels for SNRs ranging from 0 dB to 22 dB in a 2×1 diversity scheme, compared with a SISO LS estimation that uses repeated pilot symbols. It should be also noted the evident LUT switching effect at SNR = 10 dB. The MSE performance in channel A is mainly driven by τ_{rms} switching because of a huge mismatch at low SNRs. On the contrary, the MSE performance in channels B and C is mainly driven by SNR mismatch as the fixed τ_{rms} value of 125 ns produces a close match to both channels B ($\tau_{rms} = 100$ ns) and C ($\tau_{rms} = 150$ ns).

When the measured SNR is high (≥ 10 dB), τ_{rms} of the channel needs to be estimated for the selection of one of two appropriate LUTs. When the measured SNR is low (< 10 dB), the third LUT is used and r.m.s. delay spread estimation is not required. In the latter case, the measurement of τ_{rms} becomes poor (refer to Fig. 3.8 and Fig. 3.9) and this will not improve the LMMSE channel estimation performance. Instead, a fixed τ_{rms} value should be used for the third LUT.

Fig. 5.11 shows the effect of LUT switching based on estimated SNR values using Equation (3.8) and estimated τ_{rms} values using Equation (3.19). L_0 and ρ parameters were set to 16 taps and -24 dB respectively (refer to Chapter 3). It should be noted from Fig. 5.11 that a switching effect between the tables is not as

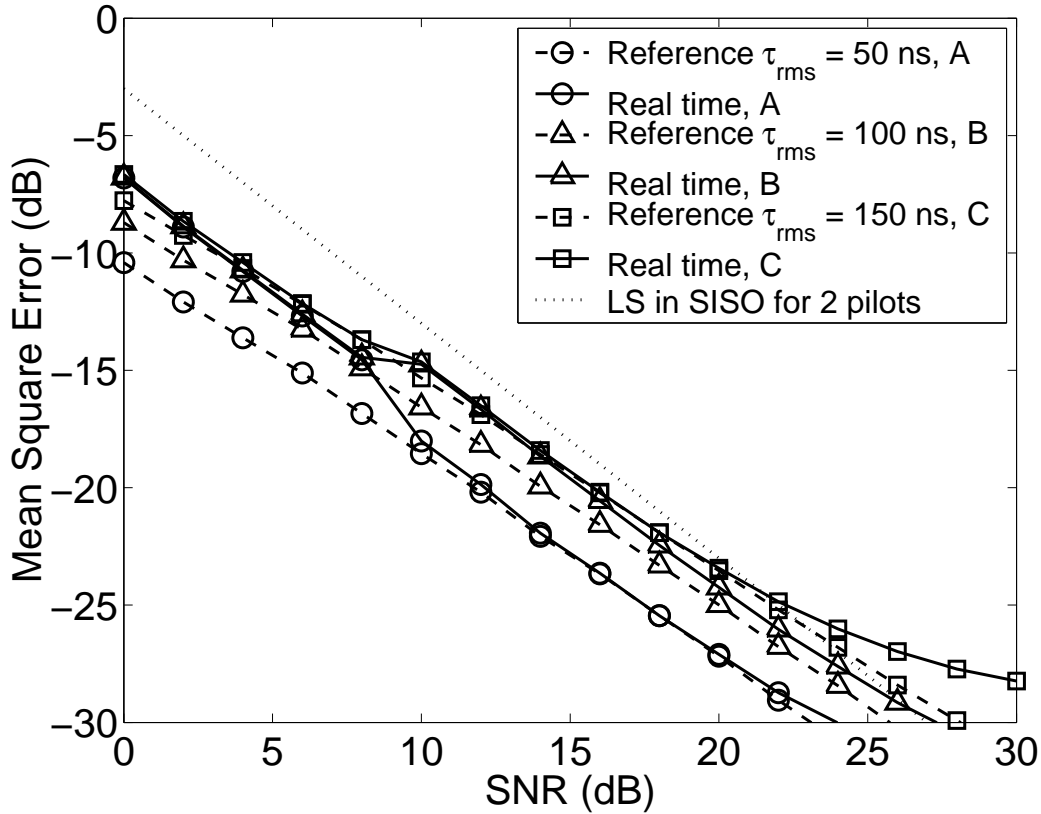


Figure 5.10: Real time LMMSE processor performance in a 2×1 802.11a for channels A, B and C. Perfect knowledge for SNR and τ_{rms} is assumed.

evident as it was in Fig. 5.10. This is due to imperfect estimation of the threshold levels by measurement for both SNR and τ_{rms} , when affected by the noise. Despite this, all three curves remain below the fine dotted line (MSE performance in SISO OFDM with the repeated pilot symbols) in SNR range from 0 to 22 dB, similar to Fig. 5.10. This indicates an adequate performance of the real time LMMSE channel estimator in the analysed environment.

Improved performance for SNRs above 22 dB would require additional LUTs. For many applications this is not worth it because other error sources start to dominate. For example, hardware errors in the 802.11a standard are specified at an $MSE = -26$ dB [38].

The BER performance was evaluated for a 2×1 Alamouti space-time coding (STC) scheme by transmitting 5,000 packets, each with 18 uncoded OFDM-BPSK data symbols [89]. The block diagram is shown in Fig. 5.12.

The data symbols were sent on K subcarriers as defined by Equation (2.21) from each of Q transmit antennas (i.e. KQ BPSK data symbols at a time). The duration

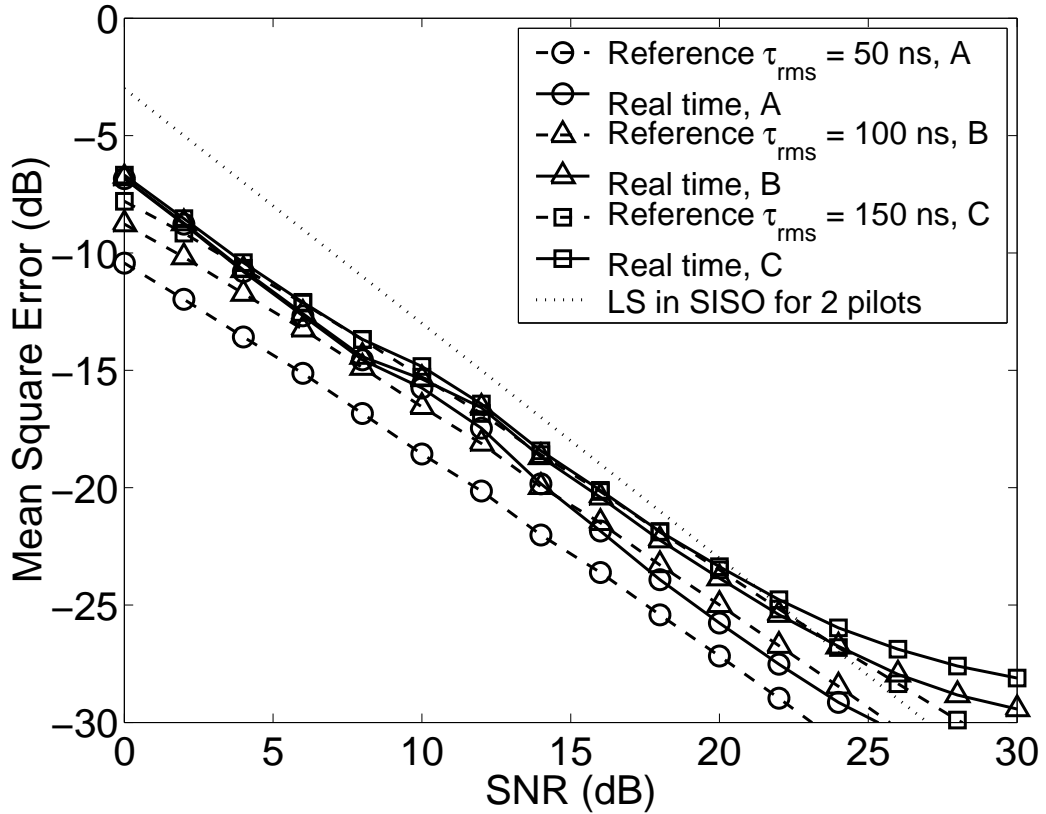


Figure 5.11: Real time LMMSE processor performance in a 2×1 802.11a for channels A, B and C. Measured threshold levels for SNR and τ_{rms} .

of the data symbols was $4 \mu s$ including the single-length CP of $0.8 \mu s$ (refer to Table 2.1). Two long pilot symbols were inserted at the start of every packet (10% pilot symbol overhead) using the *basic* pilot symbol structure. Channel B was randomly generated for each packet, but the channel remained constant over the packet. The real time LMMSE processor was operating based on the LUT selection criteria given in Table 5.1.

The BER performance is presented in Fig. 5.13 for both ideal and real time LMMSE processors. A reference curve for the perfect channel knowledge is also

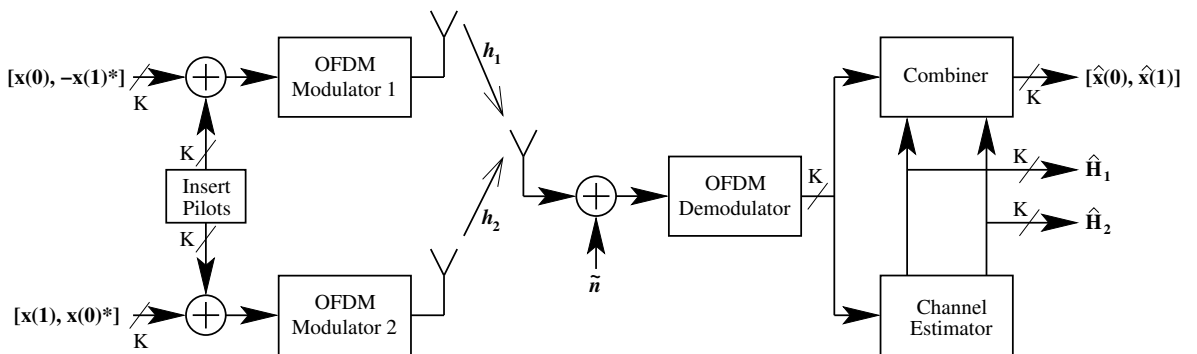


Figure 5.12: 2×1 Alamouti STC OFDM.

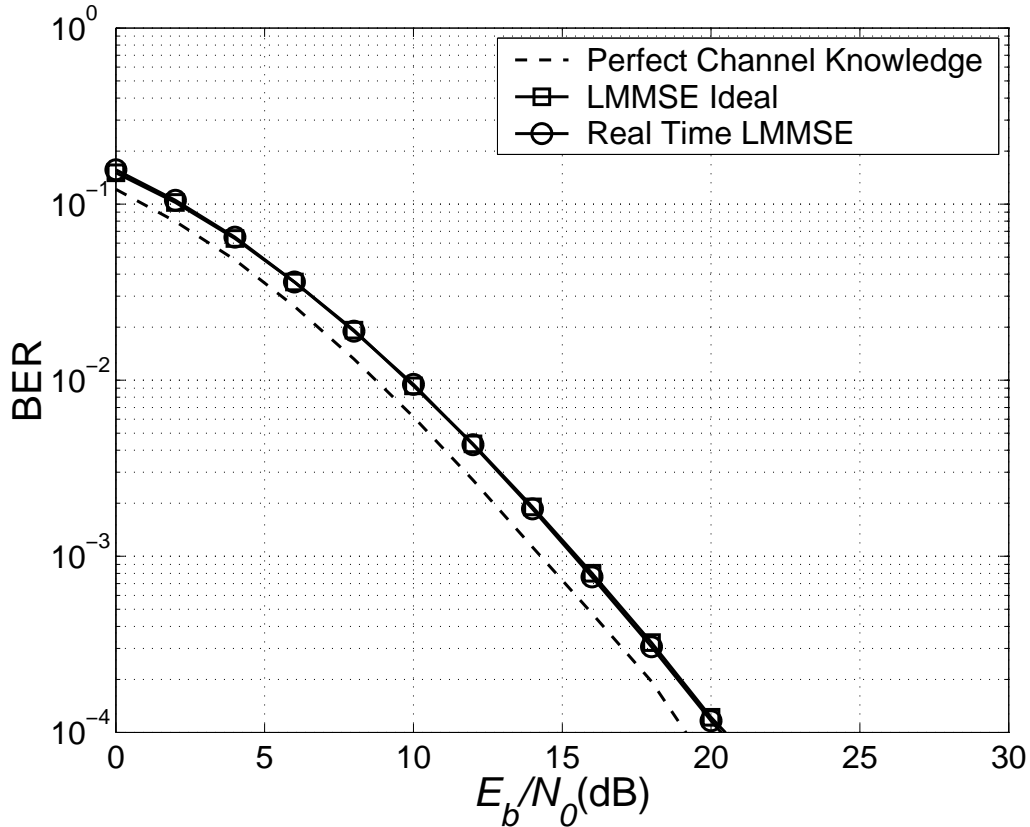


Figure 5.13: BER for a 2×1 Alamouti STC in channel B.

given. The BER curves actually illustrate, in addition to the MSE analysis, that the real time LMMSE channel estimation can reach a close performance match to the ideal LMMSE processor, in at least a given range of $E_b/N_0 \leq 20$ dB (where E_b denotes the energy per bit).

5.2 LMMSE Channel Estimation in MISO WLANs

LMMSE processing in MISO OFDM given by Equation (4.19) requires K/Q multiplications per tone in the *basic* pilot scheme, SK/Q multiplications in the *modified-1* pilot scheme and $2K/Q$ in the *modified-2* pilot scheme. Variable S denotes the number of independent pilot symbols (and also the time diversity order) each preceded by a CP. To further reduce the computational complexity of the full LMMSE processor, the low-rank approximation by SVD can be used [57], [90]. This is evaluated in the following section.

5.2.1 Low-Rank Approximations

The low-rank approximation of the LMMSE fixed weighting matrix, \mathbf{W}_j , is found from the correlation matrices $\mathbf{R}_{\mathbf{H}_j \tilde{\mathbf{P}}_j}$ and $\mathbf{R}_{\tilde{\mathbf{P}}_j \tilde{\mathbf{P}}_j}$ defined in Section 4.2 by Equation (4.19).

Equation (4.19) can be rewritten as follows

$$\hat{\mathbf{H}}_j = \mathbf{R}_{\mathbf{H}_j \mathbf{P}_j} \mathbf{R}_{\tilde{\mathbf{P}}_j \tilde{\mathbf{P}}_j}^{-1} \mathbf{R}_{\tilde{\mathbf{P}}_j \tilde{\mathbf{P}}_j}^{1/2} \mathbf{R}_{\tilde{\mathbf{P}}_j \tilde{\mathbf{P}}_j}^{-1/2} \tilde{\mathbf{P}}_j. \quad (5.4)$$

The best low-rank approximation of $\mathbf{R}_{\mathbf{H}_j \mathbf{P}_j} \mathbf{R}_{\tilde{\mathbf{P}}_j \tilde{\mathbf{P}}_j}^{-1} \mathbf{R}_{\tilde{\mathbf{P}}_j \tilde{\mathbf{P}}_j}^{1/2}$ is given by the SVD [85]

$$\mathbf{R}_{\mathbf{H}_j \mathbf{P}_j} \mathbf{R}_{\tilde{\mathbf{P}}_j \tilde{\mathbf{P}}_j}^{-1} \mathbf{R}_{\tilde{\mathbf{P}}_j \tilde{\mathbf{P}}_j}^{1/2} \triangleq \mathbf{U}_j \boldsymbol{\Sigma}_j \mathbf{V}_j^H, \quad (5.5)$$

where \mathbf{U}_j and \mathbf{V}_j^H are unitary matrices, and $\boldsymbol{\Sigma}_j$ is a diagonal matrix with the singular values corresponding to antenna j .

The rank- \mathbb{R} estimator is then defined by

$$\hat{\mathbf{H}}_j \triangleq \mathbf{U}_j \begin{bmatrix} \boldsymbol{\Sigma}_j^{\mathbb{R}} & 0 \\ 0 & 0 \end{bmatrix} \mathbf{V}_j^H \mathbf{R}_{\tilde{\mathbf{P}}_j \tilde{\mathbf{P}}_j}^{-1/2} \tilde{\mathbf{P}}_j, \quad (5.6)$$

where $\boldsymbol{\Sigma}_j^{\mathbb{R}}$ is the $\mathbb{R} \times \mathbb{R}$ upper left corner of $\boldsymbol{\Sigma}_j$, containing the strongest singular values. The superscript $(\cdot)^{\mathbb{R}}$ denotes rank- \mathbb{R} . The remaining elements of the diagonal matrix, $\boldsymbol{\Sigma}_j$, are set to zero.

The low rank- \mathbb{R} LMMSE by SVD reduces the required number of complex multiplications per tone from K/Q to $(\mathbb{R}/Q + \mathbb{R})$ in the *basic* pilot scheme, from SK/Q to $(S\mathbb{R}/Q + \mathbb{R})$ in the *modified-1* scheme and from $2K/Q$ to $2(\mathbb{R}/Q + \mathbb{R})$ in the *modified-2* scheme. This can be illustrated as follows, using for example the *basic* pilot scheme.

Equation (5.6) can be presented such that

$$\hat{\mathbf{H}}_j = \mathbf{W}_j^1 \mathbf{W}_j^2 \tilde{\mathbf{P}}_j, \quad (5.7)$$

where \mathbf{W}_j^1 of size $K \times \mathbb{R}$ is the product of matrices \mathbf{U}_j and $\boldsymbol{\Sigma}_j$, given by

$$\mathbf{W}_j^1 = \mathbf{U}_j \begin{bmatrix} \Sigma_j^{\mathbb{R}} & 0 \\ 0 & 0 \end{bmatrix}, \quad (5.8)$$

and \mathbf{W}_j^2 of size $\mathbb{R} \times K/Q$ is the product of matrices \mathbf{V}_j^H and $\mathbf{R}_{\tilde{\mathbf{P}}_j \tilde{\mathbf{P}}_j}^{-1/2}$, given by

$$\mathbf{W}_j^2 = \mathbf{V}_j^H \mathbf{R}_{\tilde{\mathbf{P}}_j \tilde{\mathbf{P}}_j}^{-1/2}, \quad (5.9)$$

where superscripts $(\cdot)^1$ and $(\cdot)^2$ symbolise the first and second set of coefficients corresponding to the approximated fixed weighting matrix, \mathbf{W}_j .

Initially, the low rank- \mathbb{R} LMMSE by SVD requires to multiply matrix \mathbf{W}_j^2 of size $\mathbb{R} \times K/Q$ by column vector $\tilde{\mathbf{P}}_j$ of length K/Q , such that

$$\mathbb{H}_j = \mathbf{W}_j^2 \tilde{\mathbf{P}}_j, \quad (5.10)$$

that uses of \mathbb{R}/Q multiplications per tone to produce the intermediate vector, \mathbb{H}_j , of length $\mathbb{R} \times 1$.

Then, the second half of the processing is accomplished by multiplying intermediate vector \mathbb{H}_j by matrix \mathbf{W}_j^1 of size $K \times \mathbb{R}$ as follows

$$\hat{\mathbf{H}}_j = \mathbf{W}_j^1 \mathbb{H}_j, \quad (5.11)$$

requiring \mathbb{R} multiplications per tone.

Thus, the LMMSE by SVD in the *basic* pilot symbol scheme with Q transmit antennas requires $(\mathbb{R}/Q + \mathbb{R})$ complex multiplications per one subchannel.

Similar to the full LMMSE channel estimation processing given by Equation (4.19), the approximated fixed weighting matrix from Equation (5.7) needs to be calculated only once and can be stored in a LUT, containing two sets of coefficients, \mathbf{W}_j^1 and \mathbf{W}_j^2 that given by Equation (5.8) and Equation (5.9) respectively.

The low rank- \mathbb{R} approximation causes an irreducible error floor [57]. To eliminate this error floor within a given SNR range, the rank- \mathbb{R} needs to be sufficiently large. Thus, the rank- \mathbb{R} choice is a trade off between the estimator complexity and estimator accuracy, particularly at high SNRs. An appropriate value for \mathbb{R} is obtained when it is within the CP range [57].

On the other hand, singular value spread depends on the channel power delay

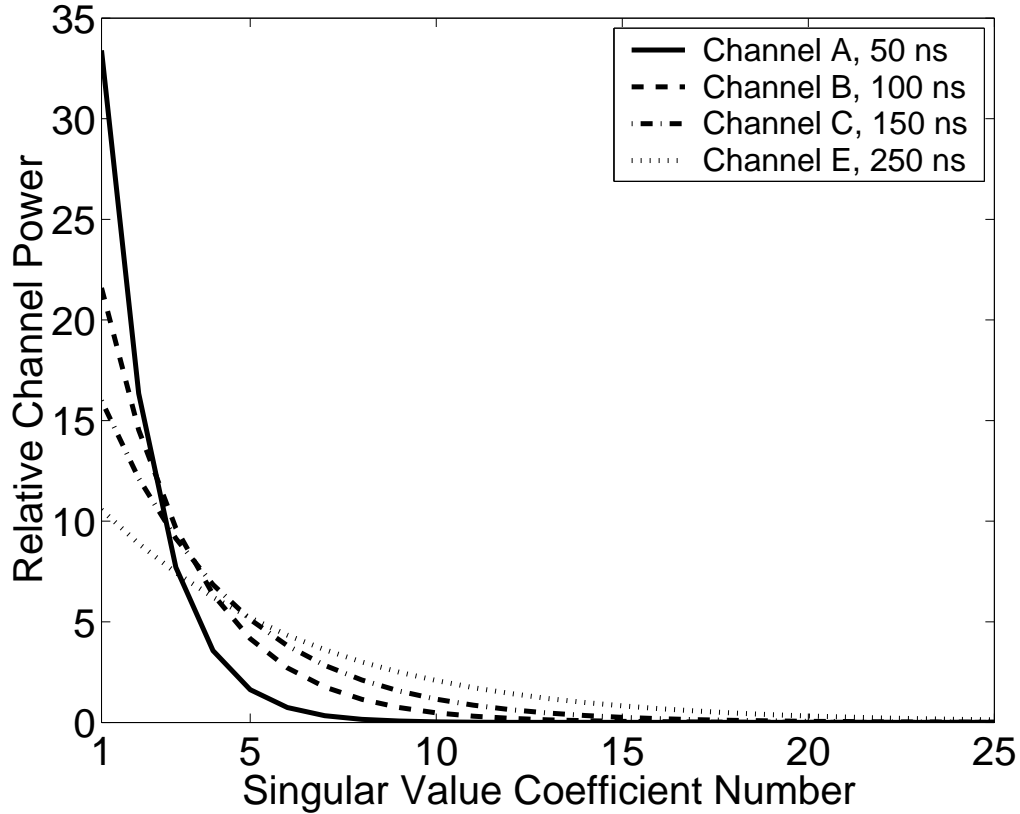


Figure 5.14: Relative channel power $\Sigma(k)/E\{|H(k)|^2\}$ of the singular value coefficients in an OFDM system with $K = 64$ and $L = 32$ for various τ_{rms} .

profile. Larger r.m.s. delay spreads in the channel, results in less singular value spread, which require a higher rank- \mathbb{R} , whilst smaller r.m.s. delay spreads in the channel produce larger singular value spreads, requiring a lower rank- \mathbb{R} [28].

This is illustrated in Fig. 5.14 for various r.m.s. delay spreads of the HIPER-LAN/2 channel models obtained from \mathbf{R}_{HH} . \mathbf{R}_{HH} was generated by means of Equation (2.19) for a SISO OFDM with $K = 64$ subcarriers and CP length of $L = 32$ samples.

By implementing the switched LUT approach described in the previous section, the appropriate rank- \mathbb{R} can be chosen based on a coarse estimate of τ_{rms} .

5.2.2 Complexity Analysis

The complexity involved in channel estimation computation using Equations (4.19) and (5.6) is presented in terms of the effective matrix size and the number of complex multiplications required for one antenna j . This is summarized in Table 5.2 for the three pilot symbol structures when transmit diversity order Q was ranging from 2

Table 5.2: LMMSE Complexity in MISO OFDM for one Transmit Antenna

Estimator	2×1		4×1		8×1	
	Matrix size	Multipl. per tone	Matrix size	Multipl. per tone	Matrix size	Multipl. per tone
LMMSE in <i>basic</i> scheme	$K/2 \times K/2$	$K/2 + 1/2$	$K/4 \times K/4$	$K/4 + 1/4$	$K/8 \times K/8$	$K/8 + 1/8$
LMMSE in <i>modified</i> schemes	$K \times K$	$K + 1$	$K/2 \times K/2$	$K/2 + 1/2$	$K/4 \times K/4$	$K/4 + 1/4$
LMMSE by SVD in <i>basic</i> scheme	$\mathbb{R} \times \mathbb{R}$	$3\mathbb{R}/2 + 1/2$	$\mathbb{R} \times \mathbb{R}$	$5\mathbb{R}/4 + 1/4$	$\mathbb{R} \times \mathbb{R}$	$9\mathbb{R}/8 + 1/8$
LMMSE by SVD in <i>modified-1</i>	$\mathbb{R} \times \mathbb{R}$	$2\mathbb{R} + 1$	$\mathbb{R} \times \mathbb{R}$	$3\mathbb{R}/2 + 1/2$	$\mathbb{R} \times \mathbb{R}$	$5\mathbb{R}/4 + 1/4$
LMMSE by SVD in <i>modified-2</i>	$\mathbb{R} \times \mathbb{R}$	$3\mathbb{R} + 1$	$\mathbb{R} \times \mathbb{R}$	$5\mathbb{R}/2 + 1/2$	$\mathbb{R} \times \mathbb{R}$	$9\mathbb{R}/4 + 1/4$

to 8. The pilot symbol overhead remained identical to an 802.11a system.

Recalling the previous section, the *basic* pilot scheme requires K/Q multiplications, the *modified-1* pilot scheme, SK/Q multiplications and the *modified-2* pilot scheme, $2K/Q$ multiplications for one antenna j . To illustrate the complexity contributed by the LS estimation, the required additional complex multiplications are also included in Table 5.2.

By analysing the entries in Table 5.2, it can be seen that the *basic* pilot scheme is less complex than the *modified* pilot schemes for a given diversity order Q , for both the LMMSE and optimal low rank- \mathbb{R} approximation by SVD. This is due to a different LS estimation approach used in the *modified-1* pilot scheme that produces the double number of measured subchannels (Equation (3.5)) and a twofold increase of subcarrier number in the *modified-2* pilot scheme. Both *modified* pilot schemes reduce the interpolation error (refer to Fig. 2.4), at the expense of processing complexity. The *modified* schemes require $(K/Q + 1/Q)$ more complex multiplications for LMMSE processing. While the low rank- \mathbb{R} approximation of the *modified* schemes requires $(r/Q + 1/Q)$ and $(3r/Q + 1/Q)$ more complex multiplications, for the *modified-1* and *modified-2* schemes respectively.

When the CIR of a multipath channel is confined to the single CP length, all three pilot structures remain ISI/ICI error free. For a 2×1 diversity system, the *modified-1* pilot scheme remains also interpolation error free. Given that $S = Q$, all K LS attenuations are available for both LMMSE (Equation (4.19)) and low rank- \mathbb{R}

approximation by SVD (Equation (5.6)) processing.

When the CIR exceeds the single CP length, the longer CP and closer spacing between the subcarriers of the *modified-2* pilot scheme can improve the estimator performance by eliminating the ISI/ICI error term, $e(i; k)$, (refer to Equation (2.10)) and by reducing the interpolation error. However, the *modified-2* scheme is the most complex pilot symbol structure when compared to the two preceding schemes, requiring $2K$ subchannels and twofold increase of FFT size.

5.2.3 Numerical Results

Both interpolation error and ISI/ICI error have the same effect on the channel estimation performance. They cause an MSE floor at high SNRs.

The MSE_j given by Equation (4.28) of the LMMSE estimation (Equation (4.19)) and optimal low rank- \mathbb{R} approximation by SVD (Equation (5.6)) were analysed by simulations.

The MSE channel estimation performance was evaluated by sending 2000 OFDM-BPSK pilot symbols in an 802.11a system. The *basic* and *modified-1* schemes used 52 interleaved subchannels (refer to Table 2.1), while the *modified-2* scheme used 104 interleaved subchannels (out of a possible $2K = 128$). HIPERLAN/2 NLOS channels A, B, C and E (refer to Table 2.2) were used and a transmit diversity of the order of 2, 4 and 8 analysed. It was assumed that perfect knowledge of the SNR and r.m.s. delay spread, τ_{rms} , were available for the calculation of the fixed weighting matrices from Equations (4.19) and (5.6).

The MSE performance of the three channel estimation schemes is presented in Fig. 5.15 and Fig. 5.16 for a 4×1 diversity scheme for the LMMSE estimator given by Equation (4.19).

The *modified* pilot schemes outperform the *basic* pilot scheme for all cases, at the expense of increased computational complexity. In the *modified* pilot schemes ($K/4+1/4$) more complex multiplications per tone are required. Also, the *modified-2* pilot scheme adds more complexity for $\mathbf{y}_j(i)$ calculation requiring a twofold increase of the FFT size. When the interpolation process is involved, the MSE error floor rises with the delay spread, as the channel's coherence bandwidth decreases (refer to Fig. 2.4). The *basic* scheme exhibits the most significant error floor, because

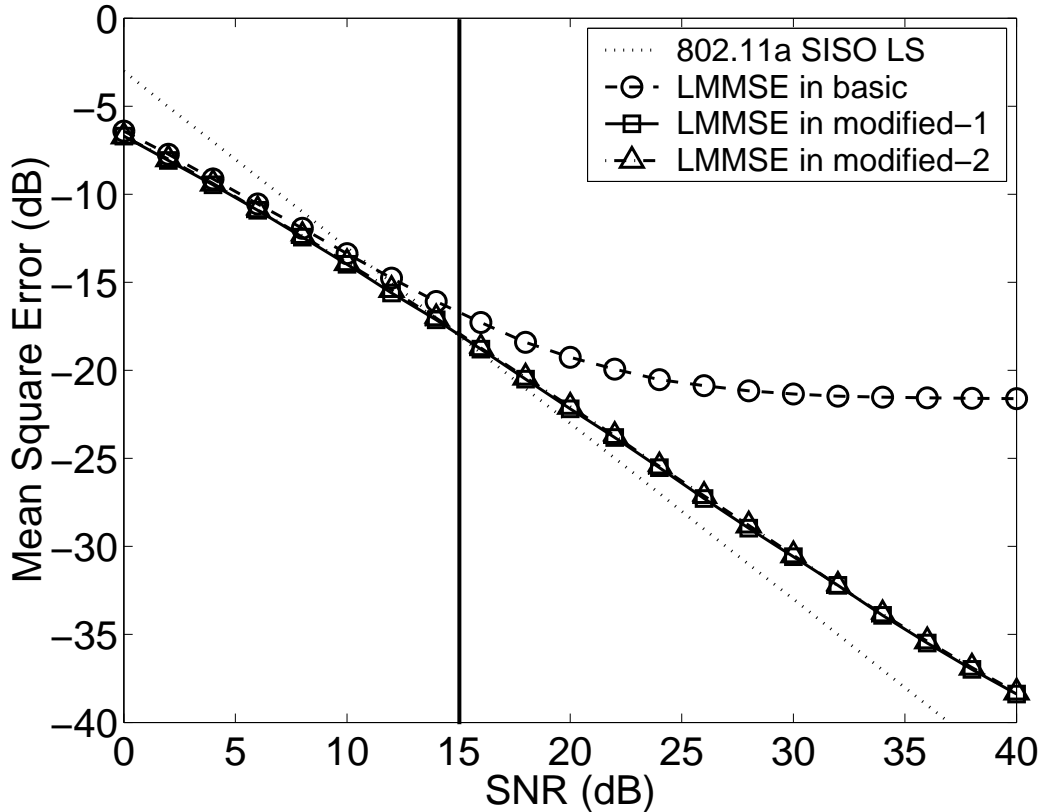


Figure 5.15: LMMSE channel estimation MSE in a 4×1 diversity scheme for HIPER-LAN/2 channel B ($\tau_{rms} = 100$ ns, $\tau_x = 730$ ns).

of the greater spacing between the measured pilot tones, with $K/Q = 13$ ($Q = 4$). The modified-1 scheme produces $2K/Q = 26$ measured subcarriers, resulting in better interpolation performance. The *modified-2* scheme makes the same frequency spacing between the measured subcarriers as the *modified-1* scheme and therefore has the same interpolation performance. This is shown by the bottom curve ('LMMSE in *modified-2*') in Fig. 5.16. It has an 18 dB lower error floor compared to the *basic* scheme showing the benefit of the closer frequency spacing.

On the contrary, the performance degradation of the *modified-1* scheme is solely due to the additional ISI/ICI error caused by the non-adequate CP length compared with the *modified-2* scheme. Consequently, the MSE error floor raises 12 dB for the former scheme and the interpolation error becomes insignificant compared to the interference error term.

It should be also noted that the data symbols, which follow the pilot symbol sequence, are only preceded by a single CP length [38]. Therefore, the data will inevitably be affected by ISI/ICI in channels with delay spreads longer than 800

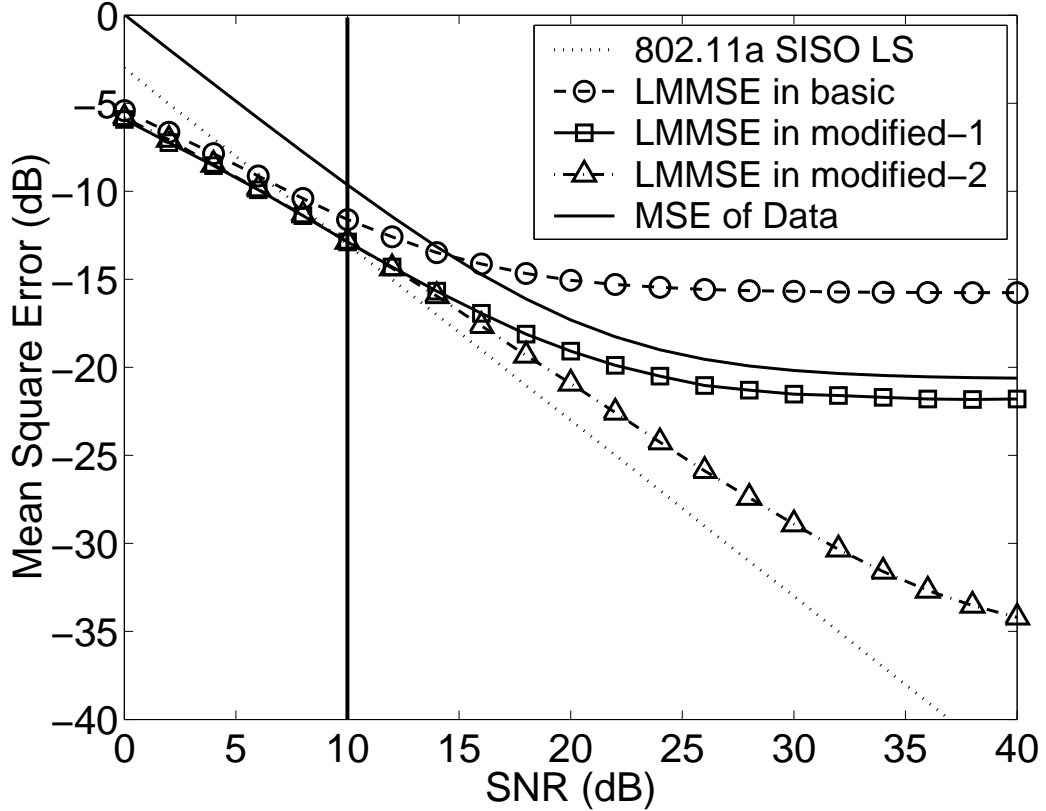


Figure 5.16: LMMSE channel estimation MSE in a 4×1 diversity scheme for HIPERLAN/2 channel C ($\tau_{rms} = 150$ ns, $\tau_x = 1050$ ns).

ns. The MSE of the data is also shown in Fig. 5.16 for comparison. The channel estimation MSE is lower than the data MSE for both *modified* schemes (which is partially due to the LMMSE filtering effect of the interpolation process). Conversely, the channel estimation MSE floor for the *basic* scheme is some 5 dB above the data MSE at high SNRs, which makes this scheme unsuitable in the analysed scenario.

The channel estimation systems need to operate effectively while maintaining an MSE that does not dominate the receiver noise performance to justify the coherent detection [4]. For MSE analysis, a simple SISO LS channel estimation is used, obtained from two long OFDM pilot symbols, as the bound for acceptable performance ($MSE = -(\text{SNR} + 3)$ dB (see Section 5.1.2)). The SNR boundary where the MSE is acceptable (requiring no additional pilot overhead as specified by 802.11a) for the LMMSE estimation described by Equation (4.19) is given in Table 5.3, for 2×1 , 4×1 and 8×1 diversity schemes, based on HIPERLAN/2 channels.

The ISI/ICI free channels A and B (considering the single CP length) require no additional pilots for all practical SNR values, when the diversity order is low

Table 5.3: Maximum SNR Range for the LMMSE with 802.11a Pilot Symbol Overhead

HIPERLAN/2 Channel	τ_{rms} (ns)	SNR (dB)		
		2×1	4×1	8×1
A	50	> 37 (A) ¹	27 (M1)	10.5 (M1)
B	100	> 37 (M1, M2)	15 (M1, M2)	5 (M1, M2)
C	150	25 (M2)	10 (M1, M2)	2.5 (M1, M2)
E	250	13.5 (M2)	4.5 (M1, M2)	1 (M1, M2)

(≤ 2). However, when the diversity order is increased the usable SNR range is reduced ($\text{SNR} \leq 5$ dB, for 8×1 system and channel B). The effect of longer delay spreads (channels C and E) further reduces the usable SNR dynamic range, making all diversity orders impractical for the 802.11a pilot symbol overhead in both *basic* and *modified* pilot schemes. It should be noted that the *modified-2* scheme does not necessarily improve the LS SISO bound ($\text{MSE} = -(\text{SNR} + 3)$) dB, even though it inherently has a lower error floor for the channels exceeding a single CP length. Additional pilot overhead (compared to 802.11a) or an alternative processing approach to the analysed schemes is required for diversity orders of four or above.

To illustrate the performance improvement attainable, Table 5.4¹ presents the SNR boundary for the LMMSE estimator given by Equation (4.19) when pilot symbol length is increased to $16 \mu\text{s}$ (twice the length of 802.11a).

Table 5.4: Maximum SNR Range for the LMMSE with Pilot Symbol Overhead of $16 \mu\text{s}$

HIPERLAN/2 Channel	τ_{rms} (ns)	SNR (dB)		
		2×1	4×1	8×1
A	50	> 37 (A)	> 37 (M1, M2)	27 (M1)
B	100	> 37 (M1, M2)	> 37 (M1, M2)	15 (M1, M2)
C	150	> 37 (M1, M2)	25 (M2)	10 (M1, M2)
E	250	24.5 (M1, M2)	13.5 (M2)	4.5 (M1, M2)

With the increased pilot symbol overhead, a 4×1 diversity system becomes feasible for both A and B channels, and a 2×1 system achievable for all HIPERLAN/2 channel models for the *modified* pilot schemes.

Fig. 5.17 presents the MSE performance for low rank- \mathbb{R} LMMSE by SVD estimation (Equation (4.19)) for the *modified-1* pilot symbol structure in a 2×1 diversity

¹A – any pilot symbol scheme; M1 – *modified-1* pilot symbol scheme; M2 – *modified-2* pilot symbol scheme.

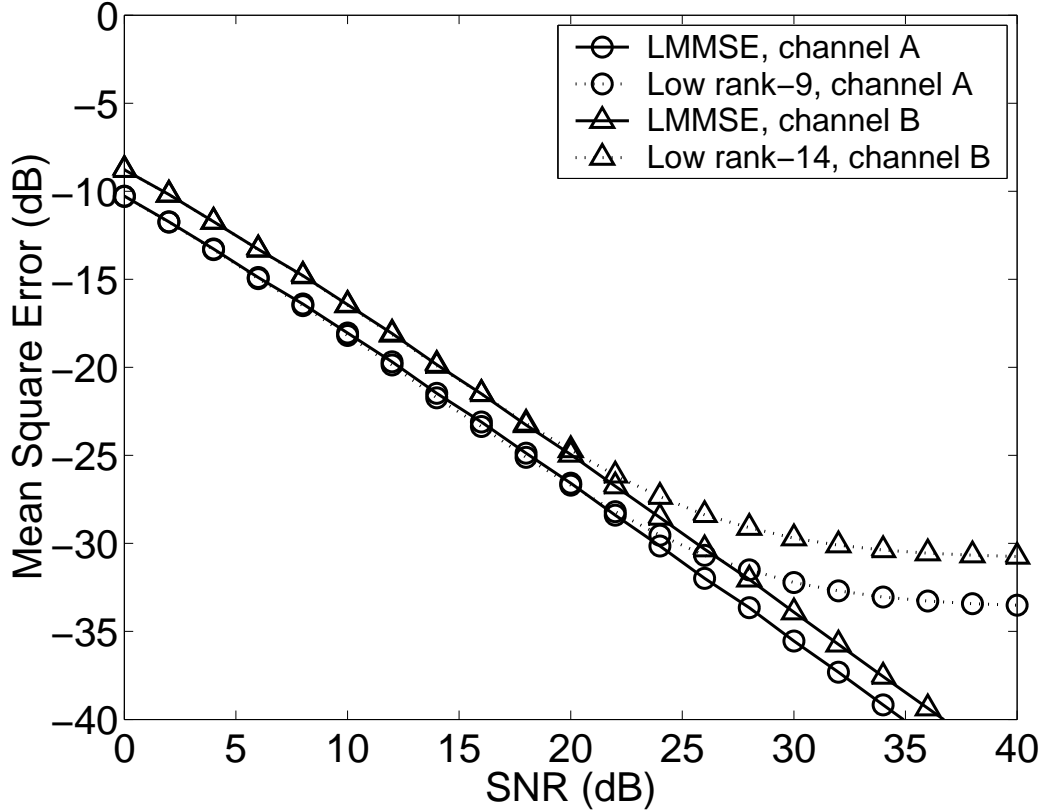


Figure 5.17: Low rank- \mathbb{R} and LMMSE channel estimation MSE of the *modified-1* scheme in a 2×1 diversity system for channels A ($\tau_{rms} = 50$ ns, $\tau_x = 390$ ns) and B ($\tau_{rms} = 100$ ns, $\tau_x = 730$ ns).

scheme, for HIPERLAN/2 channels A and B. LMMSE performance is also given for a reference. An 802.11a pilot symbol overhead is assumed.

The low rank- \mathbb{R} approximation produces an irreducible error floor. To eliminate this error floor for SNRs ≤ 30 dB (a reasonable dynamic range for practical intents [91]), the rank- \mathbb{R} is set to a value of $\mathbb{R} = 9$ for channel A and $\mathbb{R} = 14$ for channel B. The choice of \mathbb{R} is based on the r.m.s. delay spread of a channel (refer to Fig. 5.14). Although the *modified-1* scheme requires $(\mathbb{R}/2 + 1/2)$ more complex multiplications per tone compared to the *basic* pilot scheme (refer to Table 5.3), with $\mathbb{R} \ll K/Q$ the added complexity is reduced (weighted against the LMMSE processing). On the other hand, the *modified-2* pilot scheme requires $(3\mathbb{R}/2 + 1/2)$ additional complex multiplications per tone and twofold increase of FFT size for the received vector, $\mathbf{y}_j(i)$, computation, with respect to the *basic* pilot scheme. Therefore, in channels confined to the CP length, the low rank- \mathbb{R} *modified-1* pilot scheme is the best compromise in performance versus complexity for analysed channel estimation al-

ternatives, especially when the number of the pilot symbols is equal to the number of antennas. For example, a 4×1 diversity system would require 4 pilot symbols ($S = Q = 4$), this is twice the pilot symbol overhead of an 802.11a system. Adopting the switched LUT approach described in Section 5.1, the appropriate rank- \mathbb{R} can be selected, based on coarse estimates of τ_{rms} and SNR.

5.3 Summary

In this chapter, an enhanced LMMSE channel estimation algorithm was evaluated. The algorithm is based on the r.m.s. delay spread and SNR measurements in real time. Using a single fixed set of τ_{rms} and SNR values is clearly not optimum in the changing channel environments. This can degrade the LMMSE estimator MSE performance. The performance can be improved by introducing a number of LUTs and selecting the appropriate one. Selection of a LUT is based on combination of the coarse τ_{rms} and SNR estimates that can be evaluated from the LS estimation. The accuracy depends on the number of LUTs used in the processor. Three LUTs is minimum required for achieving adequate estimation accuracy for practical intents (based on study in HIPERLAN/2 channels with 802.11a OFDM system parameters).

In addition, LMMSE channel estimation performance was compared in an 802.11a MISO OFDM system for the three pilot structures. The *basic* scheme uses two long pilot symbols preceded with a CP length of 1600 ns and interleaves the tones in the frequency domain. The *modified-1* pilot scheme extends the *basic* scheme by interleaving the two pilot symbols in the time domain as well as the frequency domain. Each pilot symbol is preceded with a single CP length of 800 ns. The *modified-2* pilot scheme interleaves a single pilot symbol with a CP length of 1600 ns, over twice the number of subcarriers than the two preceding schemes. The *modified* pilot schemes always outperform the *basic* pilot scheme, since they reduce the interpolation error. No additional pilot overhead (compared to 802.11a) is necessary if the diversity order is low (≤ 2) and the maximum excess delay of the channel is confined to a CP length of 800 ns. From analysed channel estimation alternatives, the low rank- \mathbb{R} *modified-1* pilot scheme is the best compromise in performance versus complexity for the ISI/ICI free channels, especially when the number of the pilot

symbols is equal to the number of antennas.

Chapter 6

Sparse Approximations of the LMMSE Channel Estimation

The LMMSE channel estimation for OFDM systems requires a large number of complex multiplications. In this chapter, a simplified LMMSE channel estimation algorithm is evaluated in a transmit diversity environment. This is achieved by applying a significant weight catching (SWC) technique to the LMMSE fixed weighting matrix. The SWC technique itself is based on modifying the smoothing matrix by leaving the Γ largest values in each row and turning the rest to zeros. In the well known LMMSE by SVD technique the sparse approximation is accomplished by zeroing out all but the \mathbb{R} largest singular values.

The LMMSE by SWC can reduce the computational complexity of the full LMMSE processor by more than 50% and it outperforms the LMMSE by SVD over a wide range of channel delay spreads and SNRs.

6.1 Introduction

Other authors have evaluated sparse approximations of the DFT based channel estimators in [35]. However, DFT-based estimators have limited performance in non-sample spaced channels at high SNRs [57]. The low complexity LMMSE by SVD channel estimation technique has also been investigated in [57]. The low rank- \mathbb{R} LMMSE by SVD reduces the required number of complex multiplications per tone from K/Q to $(\mathbb{R}/Q + \mathbb{R})$ in a $Q \times 1$ diversity scheme, but the choice of \mathbb{R} depends

on the channel. Larger channel delay spreads, result in a reduced singular value spread, requiring a higher rank- \mathbb{R} estimator to eliminate the irreducible error floor up to a given SNR [28]. Modern WLANs must support 64-point QAM with packet error rates constraint of 1%–10%. The operating SNR can therefore go as high as 30 dB [91].

6.2 Sparse Approximations of the Fixed Weighting Matrix

In a transmit diversity environment the best low-rank approximation is given by Equation (5.6), based only on the neighbouring pilot tones. In channels with large delay spreads, the rank- \mathbb{R} needs to be sufficiently large to eliminate the MSE error floor up to a given SNR as shown in Fig. 5.14. When the rank- \mathbb{R} approaches a value of $K/(Q + 1)$, the low rank approximation no longer reduces the estimator complexity.

Based on these observations, an alternative sparse approximation technique of the fixed weighting matrix, namely LMMSE by SWC, is evaluated below.

6.2.1 LMMSE by SWC Channel Estimation

Recalling Section 4.2, the LMMSE channel estimation can be presented as follows

$$\hat{\mathbf{H}}_j = \mathbf{W}_j \tilde{\mathbf{P}}_j. \quad (6.1)$$

Obviously, some row entries in the fixed weighting matrix, \mathbf{W}_j , given by Equation (4.20) contain stronger weights, with the strongest values being on the diagonal. This is illustrated in Fig. 6.1 for four arbitrary chosen rows from \mathbf{W}_j .

\mathbf{W}_j was generated using Equation (2.19), for a 64-subcarrier OFDM system with $L = 16$ taps, operating at an SNR of 30 dB in a multipath channel with $\tau_{rms} = 50$ ns and with the sampling rate, $f_s = 20$ MHz.

Thus, the frequency domain matrix, \mathbf{W}_j , can be approximated by a sparse smoothing matrix containing the Γ strongest weights, $w_j(k, \gamma)$, in each row, where $\Gamma \leq K/Q$. The Γ weights are chosen to maximise the row energy, $E_j(k)$, given by

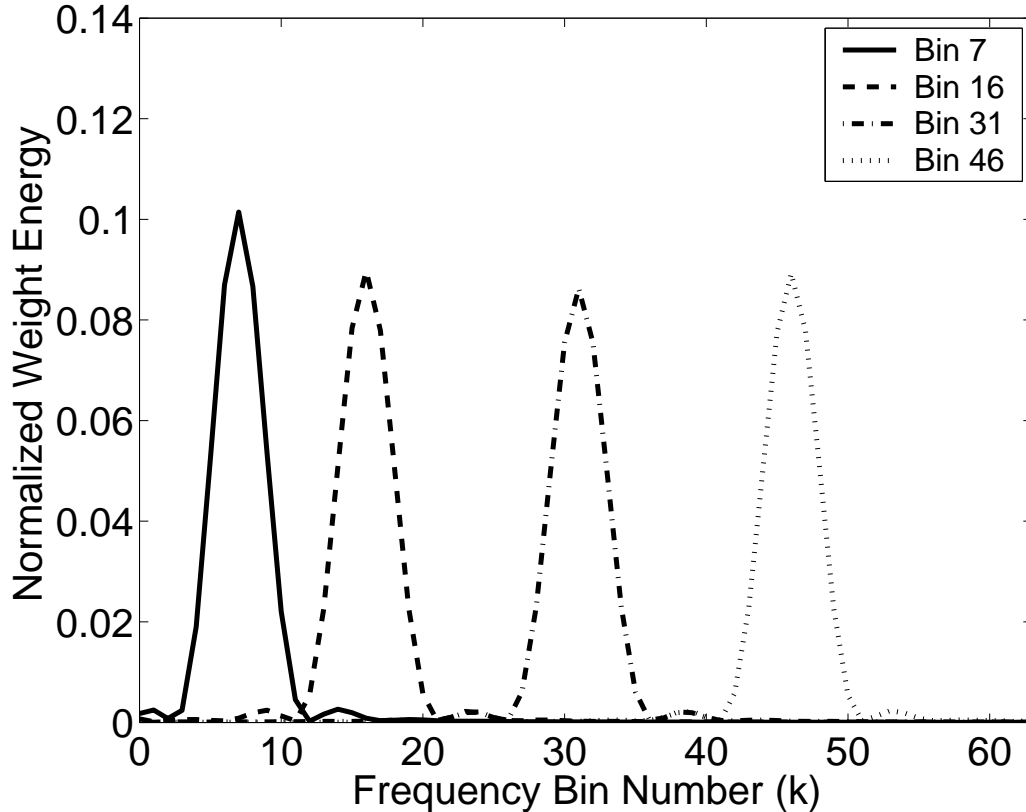


Figure 6.1: Normalized weight energy of arbitrary chosen rows from the LMMSE fixed weighting matrix generated for 64-subcarrier OFDM.

$$E_j(k) = \max_{w_j(k,\gamma) \in \mathbf{w}_j(k)} \sum_{\gamma=0}^{\Gamma-1} |w_j(k, \gamma)|^2, \quad (6.2)$$

where γ is the varying column number corresponding to the row vector, $\mathbf{w}_j(k)$, of matrix \mathbf{W}_j .

The sparse smoothing matrix, \mathbf{W}_j^Γ , is obtained by approximating \mathbf{W}_j by means of Equation (6.2) and can be given by

$$\mathbf{W}_j^\Gamma = \begin{bmatrix} w_j(0,0) & \dots & w_j(0,\Gamma-1) & 0 & \dots & 0 \\ w_j(1,0) & \dots & w_j(1,\Gamma-1) & 0 & \dots & 0 \\ \vdots & \ddots & \ddots & \ddots & \ddots & \vdots \\ 0 & \dots & w_j(K-1,0) & w_j(K-1,1) & \dots & w_j(K-1,\Gamma-1) \end{bmatrix}, \quad (6.3)$$

where the superscript $(\cdot)^\Gamma$ denotes the Γ strongest weights.

The size of the matrix, \mathbf{W}_j^Γ , is $K \times K/Q$ including $(K/Q - \Gamma)$ zeroed out column entries in each row. Clearly, multiplication operations by zero-valued weights are

unnecessary.

Thus, the LMMSE by SWC channel estimation in MISO OFDM is defined by

$$\hat{\mathbf{H}}_j^\Gamma \triangleq \mathbf{W}_j^\Gamma \tilde{\mathbf{P}}_j, \quad (6.4)$$

requiring $\Gamma \leq K/Q$ complex multiplications for each frequency bin in order to obtain the channel estimation vector, $\hat{\mathbf{H}}_j^\Gamma$, of length K for each antenna j .

6.2.2 LMMSE by SWC Complexity

The LMMSE by SWC channel estimation in MISO OFDM will produce an irreducible MSE floor when using pilot symbols with interleaved subcarriers in the frequency domain. This is because of the interpolation error caused by the dispersive wireless channels and because of the zeroing out weights in the smoothing matrix, \mathbf{W}_j^Γ , with the least significant power. To eliminate the error floor for a given Q , the number of significant weights, Γ , needs to be sufficiently large, which is in the controversy with the estimator complexity. The SWC technique allows reducing the number of required complex multiplications from K/Q to Γ in the *basic* pilot symbol structure compared with the full LMMSE estimator given by Equation (4.19).

6.2.3 MSE Mismatch

In practice, matrix \mathbf{W}^Γ for a number of expected τ_{rms} (in channels with exponential power delay profile) and SNR combinations can be precalculated in advance and stored in LUTs [58]. In operation, the corresponding LUT can be multiplied by the LS estimation vector, $\tilde{\mathbf{H}}$, that will produce the LMMSE by SWC channel estimation vector, $\hat{\mathbf{H}}$.

However, this approach can cause a mismatch between the actual multipath fading channel parameters and the expected SNR and r.m.s. delay spread values that were in fact used for the smoothing matrix coefficients calculation. This can further degrade the channel estimation MSE.

Given the true with no mismatch SNR and r.m.s. delay spread of the channel, \widetilde{SNR} and $\tilde{\tau}_{rms}$, the mismatch parameter values can be defined as follows

$$\Delta SNR \triangleq 10 \log \left(\frac{SNR}{\widetilde{SNR}} \right) \quad (6.5)$$

and

$$\Delta \tau_{rms} \triangleq 20 \log \left(\frac{\tau_{rms}}{\widetilde{\tau}_{rms}} \right), \quad (6.6)$$

where SNR and τ_{rms} are the expected parameters that were actually used to generate the smoothing matrix, \mathbf{W}^Γ .

A tolerable mismatch given by Equations (6.5) and (6.6) can be obtained based on the statistical knowledge of the channel and targeted channel estimation MSE performance for a given OFDM system. This would also indicate a number of required LUTs for achieving an adequate channel estimation accuracy. For example, for a 2×1 802.11a system operating in HIPERLAN/2 channel B, the SNR and r.m.s. delay spread mismatch can go as high as $\Delta SNR = \pm 5$ dB and $\Delta \tau_{rms} = \pm 5$ dB, for an additional MSE performance loss ≤ 3 dB. This will be shown in the next section.

6.3 Numerical Results

Simulations were carried out in an 802.11a system with Q transmitters and 1 receiver. The performance for the LMMSE, LMMSE by SVD and LMMSE by SWC was evaluated by the channel estimation MSE given by Equation (4.28) and by the BER.

Simulations were based on HIPERLAN/2 channels A ($\tau_{rms} = 50$ ns), B ($\tau_{rms} = 100$ ns) and C ($\tau_{rms} = 150$ ns), with the total transmit power normalized to unity. In Fig. 6.2 and Fig. 6.3, it was assumed that perfect knowledge of the SNR and τ_{rms} were available for calculation of \mathbf{W}_j to enable the performance comparison of the channel estimation algorithms under ideal conditions.

The MSE performance was evaluated by transmitting two long OFDM-BPSK pilot symbols 1000 times for each SNR value. The pilot symbols were simultaneously sent from Q transmit antennas on interleaved subcarriers in the frequency domain using the *basic* pilot symbol structure shown in Fig. 2.7(a). The initial LS channel

estimation vector, $\tilde{\mathbf{P}}_j$, was obtained by means of Equation (3.2). For each sparse approximation, the number of complex multipliers, N_{cm} , was restricted to $N_{cm} < K/Q$.

The BER performance was evaluated for a 2×1 Alamouti STC scheme by transmitting 5,000 packets, each with 18 uncoded OFDM-BPSK data symbols [89]. The block diagram is shown in Fig. 5.12.

The data symbols were sent on K subcarriers as defined by Equation (2.21) from each of Q transmit antennas (i.e. KQ BPSK data symbols at a time). The duration of the data symbols was $4 \mu\text{s}$ including the single-length CP of $0.8 \mu\text{s}$ (refer to Table 2.1). Two long pilot symbols were inserted at the start of every packet (10% pilot symbol overhead) using the *basic* pilot symbol structure for $Q = 2$. A new channel was randomly generated for each packet, but the channel remained constant over the packet.

As shown in Fig. 6.2(a), the LMMSE by SVD outperformed the LMMSE by SWC in channel A at SNR = 20 dB, when $Q = 2$ and $N_{cm} > 9$ ($\mathbb{R} > 6$). For $\mathbb{R} = 8$, its MSE error floor is well below -20 dB and the estimator requires $N_{cm} = 12$ complex multipliers. However, if the channel's delay spread is increased (channels B and C), the LMMSE by SWC has a better performance over a wide range of complexities (Fig. 6.2). The LMMSE by SWC only requires $N_{cm} = 12$ complex multipliers in order to reach an adequate accuracy for any channel and the estimator complexity is reduced by more than 50% compared with the full LMMSE. It is also worth mentioning that its performance remains almost unchanged in all the channels, especially when $N_{cm} \leq 12$.

Fig. 6.2(b) presents the MSE performance at SNR = 20 dB in channel B for different diversity orders. The available number of complex multipliers was ranging from 3 to 24 in a 2×1 scheme, from 4 to 16 in a 3×1 scheme and from 5 to 10 in a 4×1 scheme. When the diversity order is $Q > 2$, the LMMSE by SWC outperforms the LMMSE by SVD. The performance gain is 3.5 dB for $N_{cm} = 12$ when $Q = 3$, and for $N_{cm} = 10$ when $Q = 4$. However, the LMMSE by SVD is a marginally better choice in a 2×1 scheme, when $N_{cm} > 18$ ($\mathbb{R} > 12$).

Fig. 6.3 presents the MSE and BER performance in a 2×1 scheme for channel B. The number of complex multipliers, $N_{cm} = 3\mathbb{R}/2$, was set to fixed values 12 and

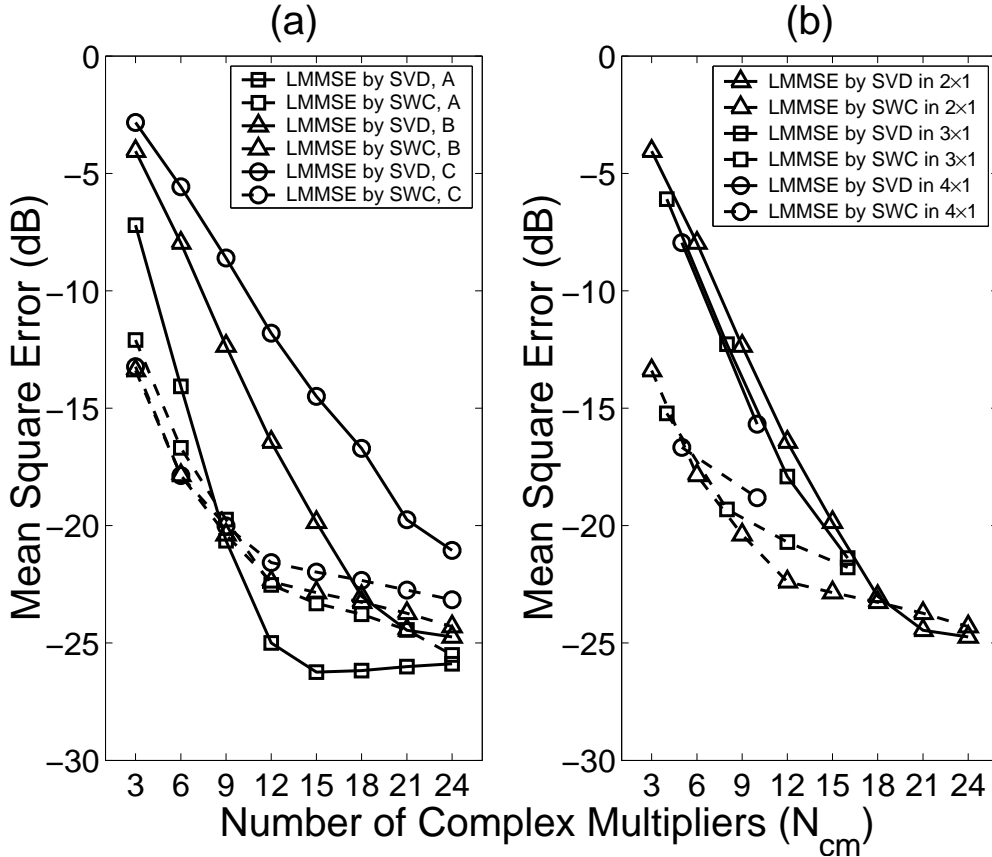


Figure 6.2: MSE performance of the sparse approximations at SNR = 20 dB for a different number of complex multiplications: (a) in a 2×1 scheme in channels A, B and C; (b) in a $Q \times 1$ scheme in channel B.

21. For $N_{cm} = 21$, the LMMSE by SVD is the better performing technique at high SNRs (Fig. 6.3(a)). However, for $N_{cm} = 12$, it is obvious that the LMMSE by SWC is the better choice (with a huge 8 dB MSE gain over the LMMSE by SVD at SNR = 26 dB, as shown in Fig. 6.3(a)). The same conclusion also holds for the BER performance (Fig. 6.3(b)). The channel estimation error of rank-8 LMMSE by SVD causes an irreducible BER error floor when $E_b/N_0 > 20$ dB. This can cause a system capacity loss, for example requiring lower constellation densities.

Fig. 6.4 presents the MSE performance for the LMMSE by SWC for a 2×1 802.11a in channel B when r.m.s. delay spread of the power delay profile and SNR were measured in real time using methods described in Chapter 5.

A perfect knowledge of SNR was available for a group of curves in Fig. 6.4(a). This enabled a performance evaluation for the LMMSE by SWC using measured r.m.s. delay spread values. Similarly, a perfect knowledge of r.m.s. delay spread of the power delay profile, τ_{rms} , was available for the curves in Fig. 6.4(b) to enable

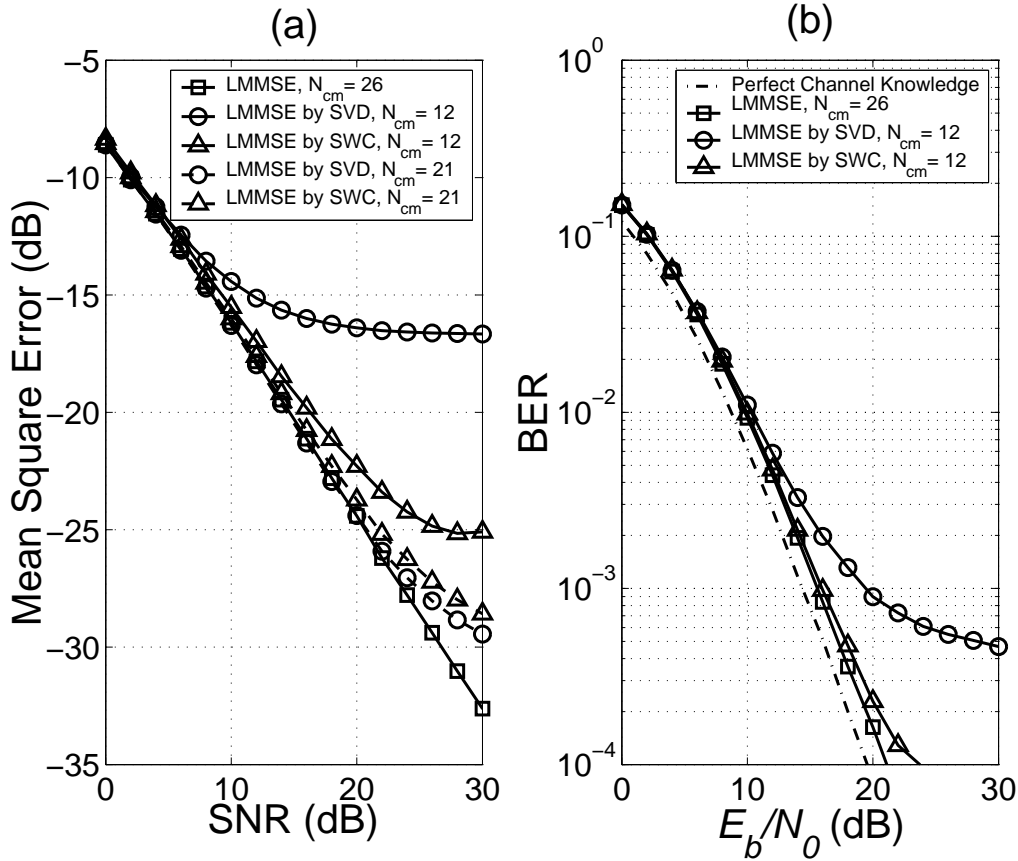


Figure 6.3: LMMSE and the sparse approximations for channel B: (a) MSE performance in a 2×1 scheme; (b) BER performance in a 2×1 Alamouti scheme for BPSK.

performance comparison for the LMMSE by SWC using a measured SNRs.

The number of complex multipliers, N_{cm} , was set to a fixed value 12. The r.m.s. delay spread of the power delay profile, τ_{rms} , was measured using Equation (3.19). The SNR was measured using Equation (3.8).

Similar to the conclusions drawn in Chapter 5, the measurement of the τ_{rms} and SNR is sufficiently accurate (especially at high SNRs). On the other hand, when introducing mismatch for both SNR and τ_{rms} the MSE performance of the estimator can degrade.

A tolerable mismatch between the actual and expected parameters depends on the channel, the OFDM system itself and the channel estimation MSE performance requirement. For example, for a 2×1 802.11a operating in channel B, the SNR and τ_{rms} mismatch can go as high as ± 5 dB, when the performance loss remains within 3 dB of the LMMSE by SWC under ideal condition. These are shown in Fig. 6.4(a) and Fig. 6.4(b) respectively. It should be noted that it is better to overestimate

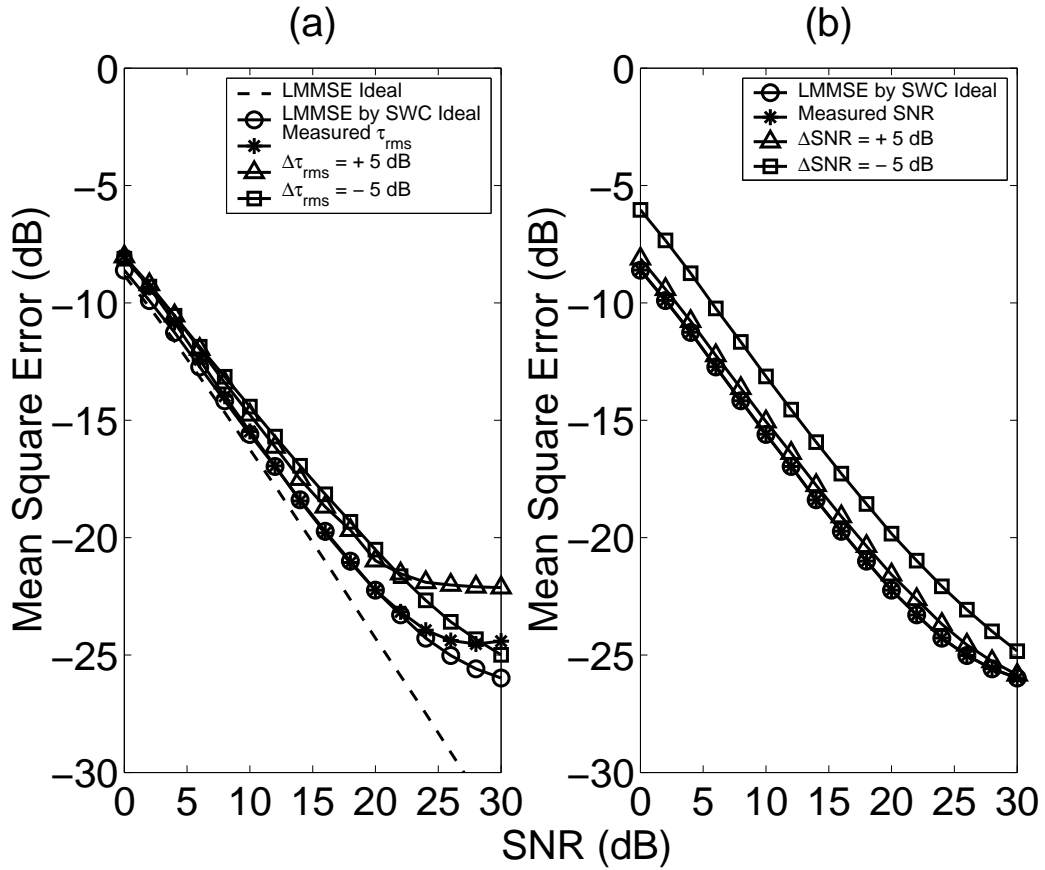


Figure 6.4: Real time LMMSE by SWC for a 2×1 802.11a in channel B.

the SNR value than underestimate. Also, the ' $\Delta\tau_{rms} = -5$ dB' curve in Fig. 6.4(a) gives better MSE performance compared to the 'Measured τ_{rms} ' curve at high SNRs. This is due to the CIR power smearing in non-sample spaced channels that causes the overestimation of the measured τ_{rms} .

6.4 Summary

In this chapter, a simplified LMMSE channel estimation algorithm was evaluated for OFDM systems with transmitter diversity. The LMMSE by SWC can reduce the computational complexity of the full LMMSE processor by more than 50%. It outperforms the LMMSE by SVD in all the situations, except when the channel delay spreads are low. The SVD method is preferred when the number of active singular values is small. In a 2×1 scenario based on the 802.11a framework, the LMMSE by SWC only requires $N_{cm} = 12$ complex multipliers, with a marginal E_b/N_0 loss for BER ranging up to 10^{-4} in HIPERLAN/2 channel B.

In practical applications, the LMMSE by SWC can be implemented using a number of LUTs containing the \mathbf{W}_j^Γ coefficients for a given Γ . The number of LUTs depends on the statistical knowledge of the channel parameters, OFDM system parameters and the MSE performance requirement. For example, for a 2×1 802.11a system operating in channel B, the SNR and τ_{rms} mismatch can go as high as ± 5 dB, when the performance degradation remains within 3 dB of the MSE loss. The LMMSE processor can be compensated for τ_{rms} overestimation and SNR underestimation by introducing a bias against the measured parameter errors, particularly at high SNRs.

Chapter 7

Low Complexity LMMSE Channel Estimation

The LMMSE channel estimation requires a large number of complex multiplications in OFDM systems that operate in channels with an exponentially decaying power delay profile. In this chapter, a low complexity LMMSE channel estimation algorithm is described for MISO OFDM systems. The low complexity LMMSE channel estimation algorithm reduces the complex fixed weighting matrix to all real values by approximating the power delay profile, generally exponential in wireless channels, as uniform followed by positioning the CIR symmetrically around the time origin using a cyclic shift. Although some additional processing is required to estimate the maximum excess delay of the power delay profile, the proposed algorithm reduces computational complexity of the optimal LMMSE processor (using exponential power delay profile) by 50% in terms of required multiplications. Simulation studies showed that the loss of estimation accuracy remains within 1 – 2 dB over a wide range of channel delay spreads and SNRs in a 2×1 diversity scheme.

7.1 Introduction

OFDM-based WLANs generally operate in fading channels with an exponentially decaying power delay profile [45]. To enable channel estimation in MISO OFDM with Q transmitters and 1 receiver, pilot symbols can be simultaneously sent from the Q transmit antennas on interleaved subcarriers in the frequency domain as

shown in Fig. 2.7(a). At the receiving end, the LMMSE channel estimator identifies the channel characteristics in the non-measured subchannels by interpolating the different sub-sets of measured subchannels from the specified antenna [58]. Thus, in a K -subcarrier OFDM system, K/Q complex multiplications are required per tone in the *basic* pilot scheme (Fig. 2.7(a)), as the fixed weighting matrix, \mathbf{W}_j , generated using Equation (4.20) is a complex valued matrix.

In the following, a low complexity LMMSE channel estimation algorithm is evaluated that reduces the computational complexity of the optimal LMMSE processor by 50% [82]. Despite this, the estimator accuracy remains sufficiently high over a wide range of channel delay spreads and SNRs. This is achieved as described below.

Initially, the channel power delay profile is approximated as uniform. Then, by choosing an appropriate CIR window size ($K/4$ or $K/2$), the fixed weighting matrix is generated that contains weights with equal and/or sparse real and imaginary parts. Although the required number of multiplications is reduced by half, this approach imposes a restriction on the CIR window size choice. In practice, this limitation may lead to the performance loss in a different fading channel environment. To overcome this, the maximum excess delay of the power delay profile, τ_x , can be estimated first, followed by positioning the CIR symmetrically around the time origin using a cyclic shift. As a result, the generated fixed weighting matrix becomes all real valued, preserving its high accuracy for any τ_x . Further complexity decrease, at the cost of performance loss, can be achieved by a sparse approximation of the LMMSE fixed weighting matrix, for example employing the optimal low rank reduction by SVD or SWC technique as described in Chapter 6.

7.2 Low Complexity LMMSE Channel Estimation

In the following, HIPERLAN/2 channel models are considered with an exponentially decaying power delay profile. The exponential power delay profile is given by Equation (2.17) and the corresponding correlation coefficient calculation is given by Equation (2.19).

7.2.1 Approximating the Exponential Power Delay Profile as Uniform

Due to the random nature of the multipath channel, its power delay profile, generally exponential in an indoor environment [45], can be approximated as uniform. Though the above statement can be argued, this simple assumption allows us to significantly improve the optimal LMMSE channel estimator complexity.

Resorting to this idea, the uniform power delay profile, $\theta_u(\tau_m)$, can be given by [92], [93]

$$\theta_u(\tau_m) = \begin{cases} 1/L_0 & \text{if } \tau_m \in [0, L_0], \\ 0 & \text{otherwise} \end{cases} \quad (7.1)$$

where the subscript $(\cdot)_u$ denotes uniform power delay profile and L_0 is the CIR window size of interest, where $L_0 \leq L$, containing the CIR taps with the most significant power.

After the integration over the given limits, $[0, L_0]$, by means of Equation (2.18) for $\theta(\tau_m) = \theta_u(\tau_m)$, the correlation coefficients $r_u(k' - k)$ with the uniform power delay profile can be expressed as

$$r_u(k' - k) = \text{sinc}(\pi L_0(k' - k)/K) e^{-j\pi L_0(k' - k)/K}. \quad (7.2)$$

Notice, that the frequency domain correlation for the uniform power delay profile in the above equation is a function of the excess delay, L_0 , rather than of the r.m.s. delay spread as for the exponentially decaying power delay profile given by Equation (2.19).

The frequency domain correlation versus L_0 (the length of the uniform power delay profile) is shown in Fig. 7.1 for the first 9 subcarriers. As L_0 increases the coherence bandwidth of the uniform power delay profile quickly decreases. The plot is presented for a 64-subcarrier OFDM that operates at the sampling rate of 20 MHz (similar to 802.11a) with L_0 ranging between 400 ns (8 samples) and 1600 ns (32 samples).

By setting L_0 to $K/4$ or $K/2$ (for $K = 2^b$ with b being an integer) in Equation (7.2), the modulus of real and imaginary parts of coefficients $r_u(k' - k)$, all become

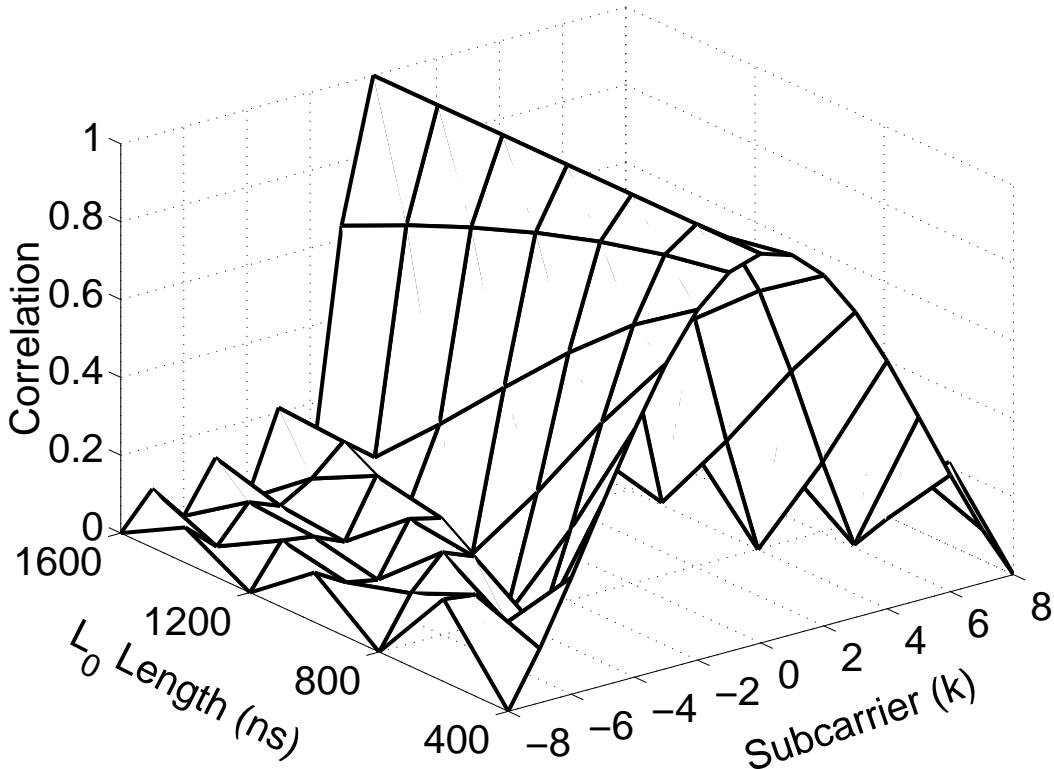


Figure 7.1: Frequency domain correlation in 802.11a using the uniform power delay profile.

equal and/or sparse values. This is also true for the fixed weighting matrix, \mathbf{W}_j . Thus, the number of required multiplications is reduced by half in Equation (4.19).

A drawback of this approach is that the CIR window size is restricted to a fixed value of $L_0 = K/4$ or $L_0 = K/2$, which is not always the true maximum excess delay of the power delay profile in a random multipath channel environment. Consequently, this can cause the performance degradation of the estimator. Clearly, the best choice for L_0 parameter would be the channel's true τ_x value. However, in practical applications τ_x can only be measured in real time and then can be used in a processing approach that is evaluated below.

We can consider the right hand side of Equation (7.2) as the Fourier transform of the uniform power delay profile, $\theta_u(\tau_m)$, using Equation (2.18). Then, applying the time shifting property of the Fourier transform to $\theta_u(\tau_m)$, the shifted CIR for $(-L_0/2)$ taps can be expressed such that [94]

$$\mathfrak{F}\{\theta_u(\tau_m + L_0/2)\} = e^{j\pi L_0(k'-k)/K} r_u(k' - k), \quad (7.3)$$

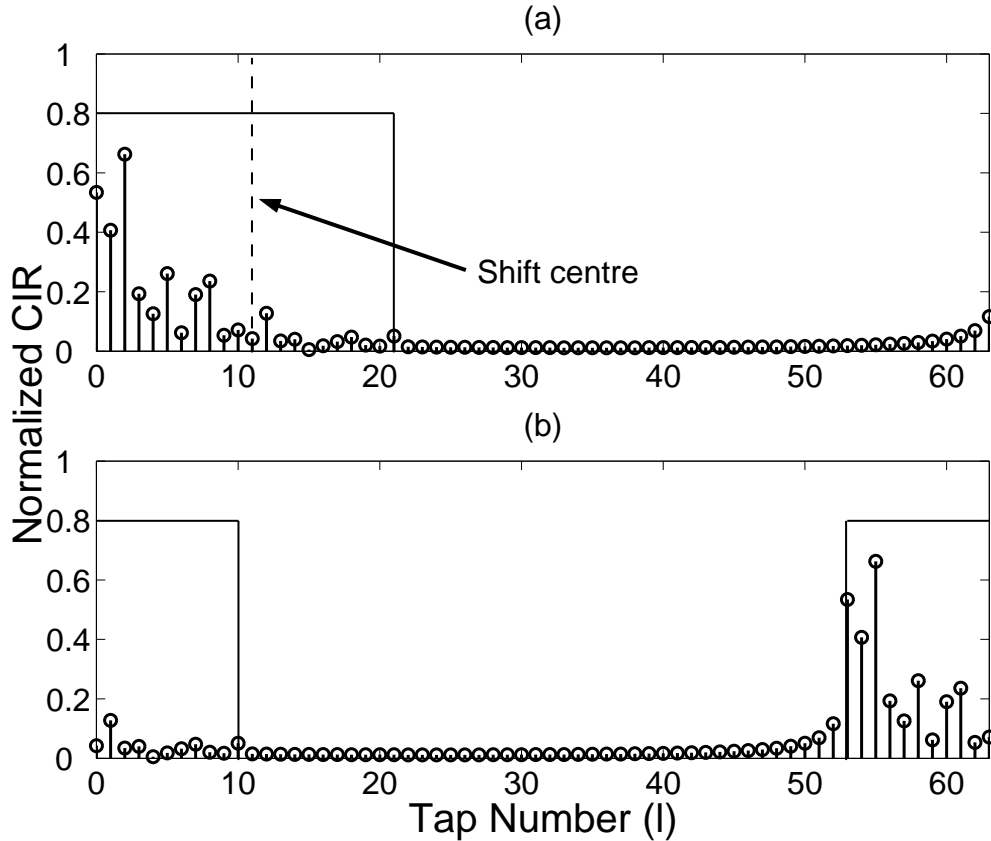


Figure 7.2: Observed CIR of HIPERLAN/2 channel C obtained by means of a 64-subcarrier IFFT: (a) a random noiseless realization; (b) the CIR positioned symmetrically around the time origin using a cyclic shift of $L_0/2 = 11$.

where $\mathfrak{F}\{\cdot\}$ denotes the Fourier transform by means of Equation (2.18).

An illustrative example is shown in Fig. 7.2 for a random noiseless realization of the observed CIR of HIPERLAN/2 channel C, cyclically shifted to the left for $L_0/2 = 11$ samples.

After the substitution of $r_u(k' - k)$ in Equation (7.3) with the right hand side of Equation (7.2), the correlation coefficients of the shifted uniform power delay profile, $r_s(k' - k)$, are reduced to all real values, given by

$$r_s(k' - k) = \text{sinc}(\pi L_0(k' - k)/K), \quad (7.4)$$

where the subscript $(\cdot)_s$ denotes the shifted uniform power delay profile.

Therefore, the fixed weighting matrix given by Equation (4.20) becomes all real valued, too.

After the rotation of LS estimation vector $\tilde{\mathbf{P}}_j$ defined by Equation (3.2) or Equa-

tion (3.6) through a phase shift of $(-L_0/2)$ such that

$$\check{P}_j(k) = \tilde{P}_j(k)e^{j2\pi k(L_0/2)/K}, \quad (7.5)$$

and after the substitution of vector $\tilde{\mathbf{P}}_j$ with vector $\check{\mathbf{P}}_j$ in Equation (4.19), the LMMSE estimation vector, $\hat{\mathbf{H}}_j$, can be obtained using all real fixed weighting matrix \mathbf{W}_j , generated by means of Equation (7.4).

Before passing the estimated values to the rest of the receiver, vector $\hat{\mathbf{H}}_j$ can be derotated back through a phase shift of $L_0/2$, given by

$$\check{H}_j(k) = \hat{H}_j(k)e^{-j2\pi k(L_0/2)/K}. \quad (7.6)$$

K/Q and K phase rotations are required in order to obtain vectors $\check{\mathbf{P}}_j$ and $\check{\mathbf{H}}_j$ respectively. Alternatively, derotation of channel estimation vector $\hat{\mathbf{H}}_j$ can be avoided applying the linear phase component, $L_0/2$, to the following data after the pilot symbol sequence.

The evaluated algorithm restricts, however, the shift operator in Equation (7.3) to always be about the centre of the maximum excess delay of the power delay profile. Therefore, the maximum excess delay, τ_x , needs to be estimated first before the actual LMMSE processing. A simple method for the τ_x estimation has been evaluated in Section 3.3 and given by Equation (3.16).

The maximum excess delay, τ_x^j , varies depending on the multipath channel. The average SNR varies depending on the separation between a terminal and base station. In practice, the switched LUT method can be used, when a number of tables containing the fixed weighting matrix coefficients can be precalculated in advance and stored in the LUTs [58]. Then, based on the estimated values for τ_x^j and SNR, the appropriate LUT can be selected for the LMMSE processing given by Equation (4.19).

The average SNR can be obtained from the LS estimation vector, $\tilde{\mathbf{P}}_j$, using a method described in Section 3.2 (refer to Equation (3.13)). A simplified flowchart of the evaluated algorithm is summarized in Fig. 7.3.

A modified block diagram for the MISO receiver is also shown in Fig. 7.4, where the linear phase component, $L_0/2$, is applied to data.

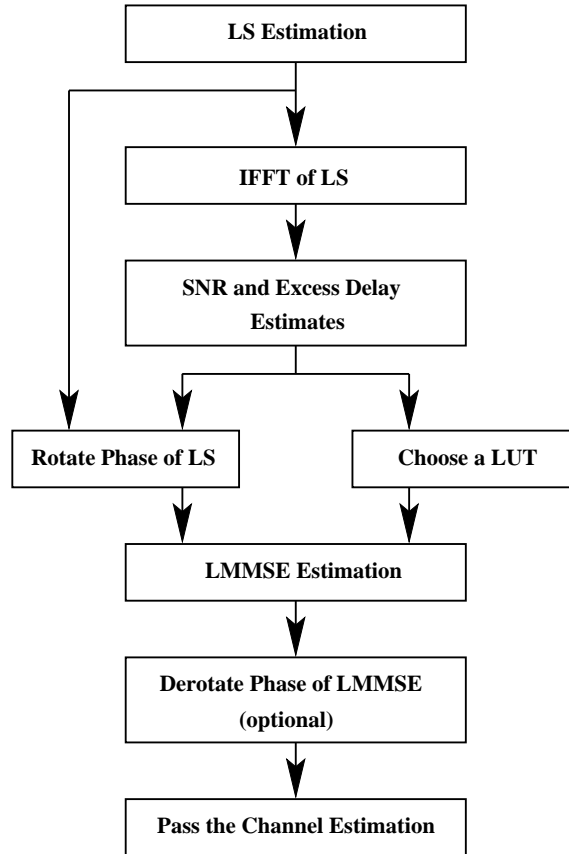


Figure 7.3: Flowchat of the LMMSE channel estimation with the shifted uniform power delay profile approximation.

7.2.2 Sparse Approximations

An LMMSE channel estimator in MISO OFDM described by Equation (4.19) still requires a large number of processing operations, despite using the real valued fixed weighting matrix. This is especially true when transmit diversity order Q is low (≤ 2) as ($\geq K/2$) multiplications per tone are necessary. This can become prohibitively complex especially in OFDM systems with a large number of subcarriers. To further reduce the estimator complexity, a sparse approximation of the fixed weighting matrix, \mathbf{W}_j , can be used.

The LMMSE by SVD requires higher rank- \mathbb{R} , and therefore more processing operations, in channels with large delay spreads to eliminate the MSE floor up to a given SNR, as has been already addressed in Chapter 5. Alternatively, the LMMSE by SWC can be used to overcome this limitation. The LMMSE by SWC algorithm has been evaluated in Chapter 6 and described by Equation (6.4).

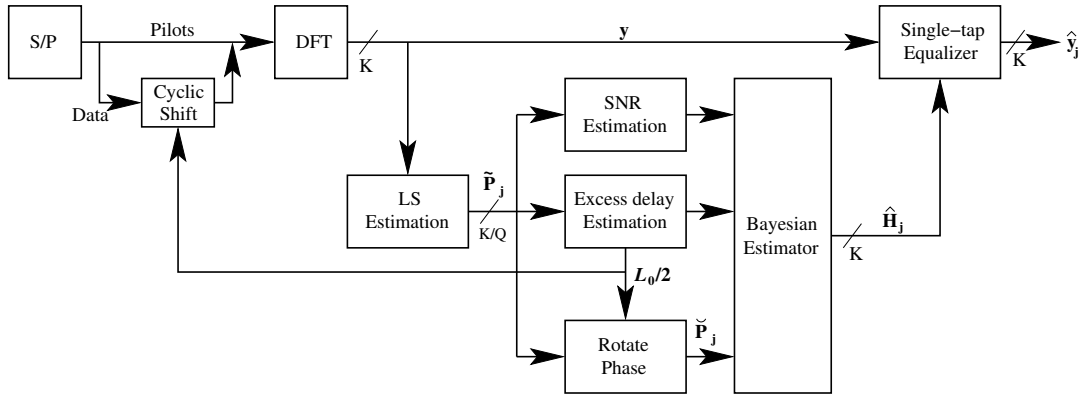


Figure 7.4: A modified block diagram of the MISO receiver using the shifted uniform power delay profile approximation.

7.3 Numerical Results

Simulations were carried out in an 802.11a system with Q transmitters and 1 receiver. The performance was evaluated based on the channel estimation MSE and BER. The MSE for antenna j is defined by Equation (4.28).

The MSE performance at each SNR value was evaluated using 1000 trials of randomly generated channels. Two long OFDM-BPSK pilot symbols were simultaneously sent from the Q transmit antennas on interleaved subcarriers in the frequency domain using the *basic* pilot symbol structure shown in Fig. 2.7(a).

The BER performance was evaluated for a 2×1 Alamouti STC scheme by transmitting 5,000 packets, each with 18 uncoded OFDM-BPSK data symbols [89]. The block diagram is shown in Fig. 5.12. The remaining BER simulation parameters are left unchanged compared to those described in Section 6.3.

HIPERLAN/2 non-sample spaced channels A ($\tau_{rms} = 50$ ns, $\tau_x = 390$ ns), B ($\tau_{rms} = 100$ ns, $\tau_x = 730$ ns) and C ($\tau_{rms} = 150$ ns, $\tau_x = 1050$ ns) were used (refer to Table 2.2). The total transmit power was normalized to unity and perfect knowledge of the SNR, τ_x and τ_{rms} was used for calculation of the fixed weighting matrix, \mathbf{W}_j , to enable channel estimation algorithm comparison under ideal condition. The CIR length, L_0 , was set to $K/4 = 16$ taps (800 ns) for the correlation matrix calculation in the scheme that uses Equation (7.2).

The optimal LMMSE (with the exponential power delay profile) requires twice the number of multiplications compared to the LMMSE with uniform (LMMSE/U) or shifted uniform (LMMSE/SU) approximations.

The MSE of the LMMSE/U and LMMSE/SU was compared to the optimal

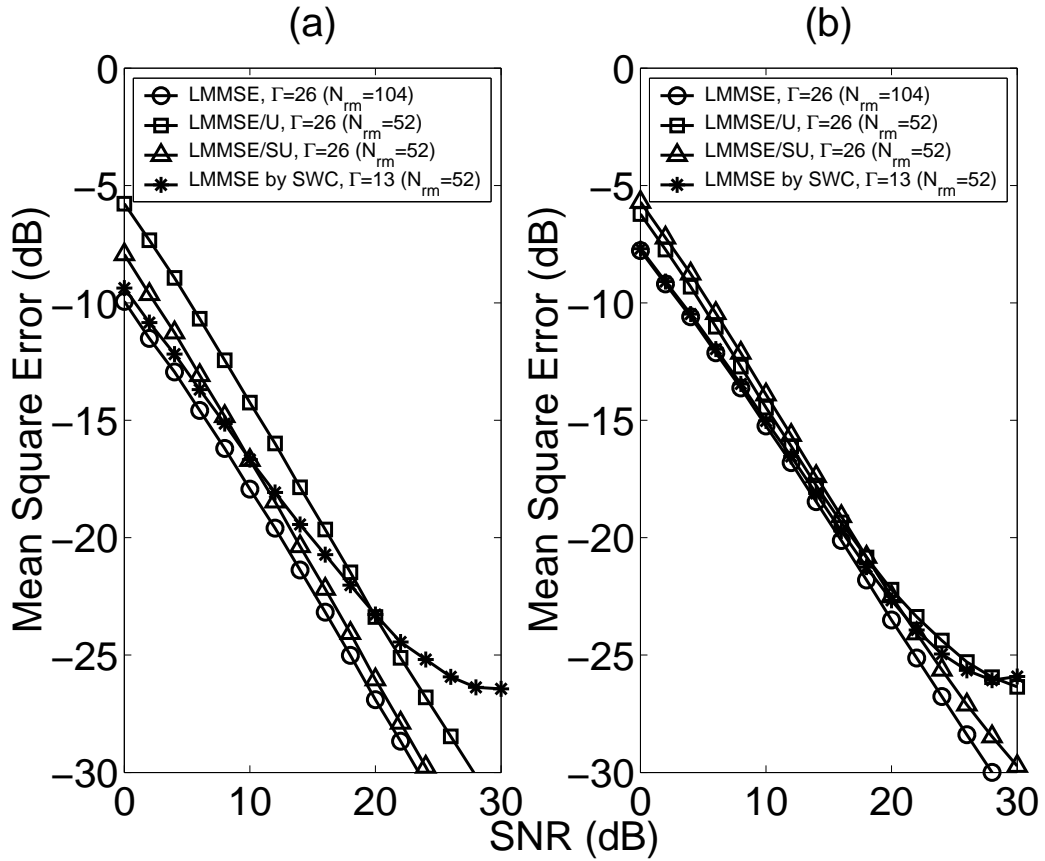


Figure 7.5: The MSE performance of the four different LMMSE processing methods in a 2×1 scheme for channels A and C.

LMMSE and also to the LMMSE by SWC, with an equal computational complexity of the latter technique to any of the two uniform approximations. All three approximations give 50% improvement in terms of the required number of real multiplications, N_{rm} , compared to the optimal LMMSE.

Of the reduced complexity methods, the LMMSE/U performed worst in a 2×1 scheme for $\text{SNR} < 20$ dB, as shown in Fig. 7.5(a). This is because of its inability to adjust the length, L_0 , to the actual τ_x in low delay spread channels, such as channel A. The problem is less evident in the longer delay spread channels, as presented in Fig. 7.5(b) for channel C, with $\tau_x = 1050$ ns. It is also apparent from Fig. 7.5 that the LMMSE by SWC is the preferred approximation technique at low SNRs in both channels A and C, as a result of its wider coherence bandwidth in the exponentially decaying power delay profile.

The same conclusion also holds for the MSE performance for channel B in a 2×1 scheme as shown in Fig. 7.6(a). The MSE of data is also presented in Fig. 7.6(a) to

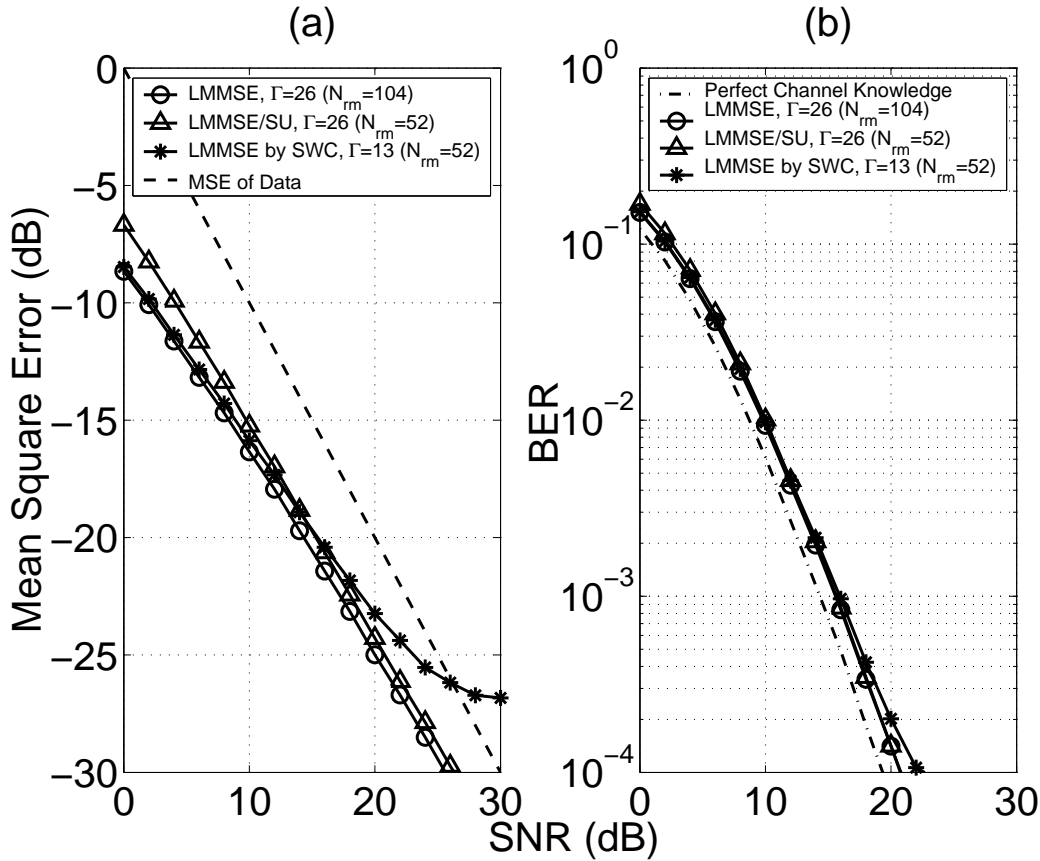


Figure 7.6: The MSE and BER performances of the LMMSE, LMMSE/SU and LMMSE by SWC in a 2×1 scheme for channel B.

justify the coherent detection for one or another channel estimation technique. Any of two approximation techniques (LMMSE/SU or LMMSE by SWC) can be used for coherent OFDM up to SNR of ≈ 24 dB. However, the LMMSE/SU becomes a preferred approximation technique for $\text{SNR} \geq 24$ dB in the analysed scenario.

The BER is also presented in Fig. 7.6(b) for channel B and shows that the LMMSE by SWC has a negligible gain over the LMMSE/SU at low SNRs, despite the 1.2 dB MSE improvement at $\text{SNR} = 6$ dB as shown in Fig. 7.6(a). This is because at low SNRs the MSE for all the channel estimation curves is significantly lower than the noise level experienced by the data (refer to Fig. 7.6(a)). On the contrary, the LMMSE/SU is the better performing technique at high SNRs, with 1.5 dB gain over the LMMSE by SWC for $\text{BER} = 10^{-4}$. This is an important result, since modern WLANs must support 64-point QAM with packet error rates constraint of 1%–10%. The operating SNR can therefore go as high as 30 dB [91].

Fig. 7.7 presents the MSE performance of the LMMSE/SU by SWC and LMMSE

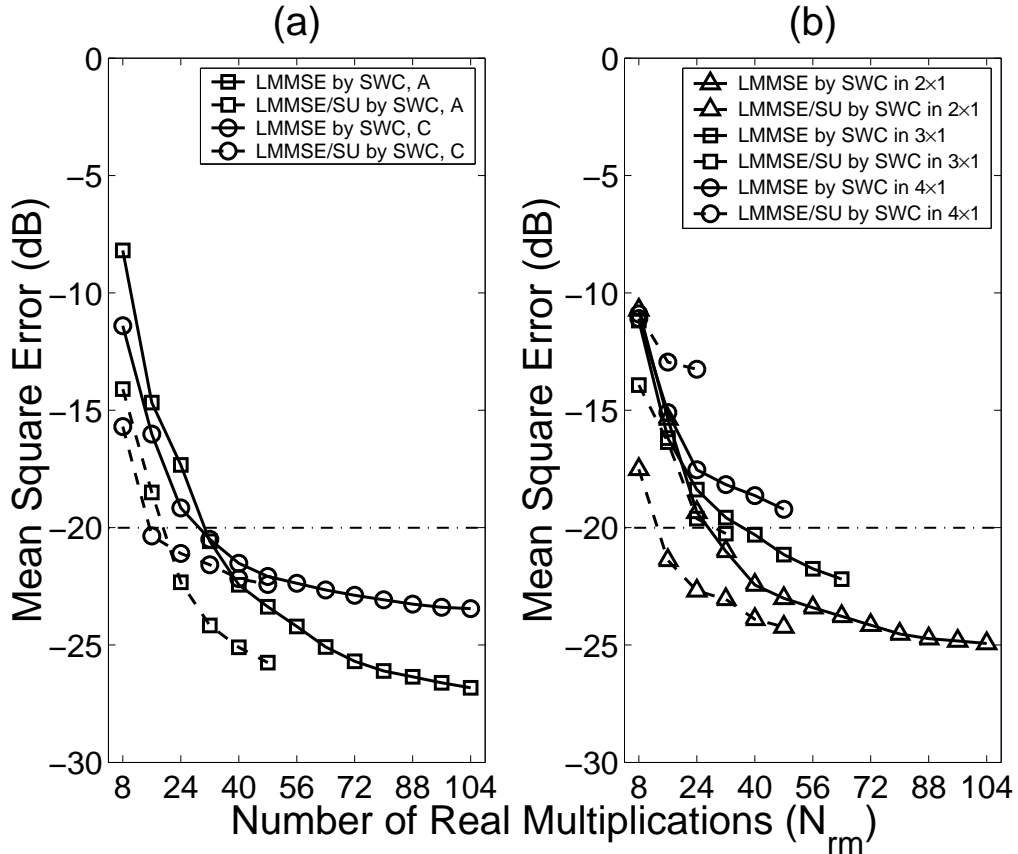


Figure 7.7: The MSE performance of the SWC technique applied to LMMSE and LMMSE/SU for a different number of required real multiplications at $\text{SNR} = 20$ dB: (a) in a 2×1 scheme for channels A and C; (b) in a $Q \times 1$ scheme for channel B.

by SWC for a different number of allowed real multiplications at a fixed value of $\text{SNR} = 20$ dB. The horizontal dotted line in Fig. 7.7 represents the MSE ($1/\text{SNR}$) of the data symbols. The channel estimation should be below this line and preferably at least 3 dB below in order to justify coherent performance. If the diversity order is low, $Q \leq 2$, the LMMSE/SU by SWC gives the better performance for a given complexity. 16 – 24 real multiplications are necessary to keep its MSE below the operating SNR value for all the channels. However, if the diversity order is increased and/or the coherence bandwidth of the channel used to generate \mathbf{W}_j (with uniform power delay profile) is too narrow (refer also to Fig. 7.1), the performance of the LMMSE/SU quickly degrades. This is shown in Fig. 7.7(b) for channel B when $Q = 4$.

7.4 Summary

In this chapter, a low complexity LMMSE channel estimation algorithm was evaluated for OFDM in a $Q \times 1$ diversity environment. The algorithm reduced the LMMSE complex fixed weighting matrix to all real values. This was achieved by approximating the power delay profile, generally exponential in wireless channels, as uniform followed by positioning the CIR symmetrically around the time origin using a cyclic shift.

At the cost of performance loss, the LMMSE/SU algorithm reduces the computational complexity of the optimal LMMSE processor (using exponential power delay profile in channels with the exponential power delay profile) by 50%. For example, in a 2×1 diversity scheme the channel estimation accuracy loss remains within 1 – 2 dB over a wide range of channel delay spreads ($\tau_{rms} \leq 150$ ns) and SNRs (6 – 26 dB).

Further complexity reduction (also at the cost of performance loss) can be achieved by the SWC technique. The LMMSE/SU by SWC can reduce the optimal LMMSE estimator complexity by more than 75%. However, a 3×1 scheme is a feasible implementation only when $\tau_x \leq 100$ ns. A 4×1 scheme is not realistic for any channel using the LMMSE/SU approximation for the analysed pilot symbol overhead and given system parameters.

Chapter 8

Conclusions

8.1 Thesis Summary

In this thesis, a deep and thorough study was carried out, based on the mathematical analysis and simulations in MATLAB, to find new and efficient channel estimation methods for MISO OFDM systems. As a result, three novel LMMSE based channel estimation algorithms were evaluated: real time LMMSE, LMMSE by SWC and low complexity LMMSE with power delay profile approximation as uniform. To further enhance the estimator performance, pilot symbol structures were investigated for a packet type MISO OFDM and methods for statistical parameter estimation in real time were also presented.

LMMSE complexity imposes a practical solution to precalculate a fixed weighting matrix in advance, based on the expected SNR and r.m.s. delay spread values (in channels with an exponentially decaying power delay profile). Using a single fixed set of r.m.s. delay spread and SNR values is clearly not optimum in the changing channel environments and it can degrade the LMMSE estimator MSE performance. It was obtained in this thesis near LMMSE performance using evaluated real time LMMSE channel estimation algorithm. The algorithm is based on r.m.s. delay spread and SNR measurements in real time. Given the measured parameters, the most appropriate fixed weighting matrix can be selected from a set of precalculated LUTs. The estimation accuracy depends on the number of LUTs used in the LMMSE processor. Based on an indoor HIPERLAN/2 channel environment, three LUTs are found to be sufficient for achieving adequate estimation accuracy in MISO

OFDM WLANs.

The LMMSE channel estimation for OFDM systems requires a large number of complex multiplications. A well known technique for reducing the computational complexity of the full LMMSE processor is a low rank approximation of the LMMSE fixed weighting matrix by SVD. In this thesis, the LMMSE by SVD was studied in various indoor multipath channel environments and it was observed that in channels with large delay spreads, the estimator rank needs to be sufficiently large to eliminate the MSE error floor up to a given SNR, still requiring a large number of processing operations. Based on these observations, an alternative sparse approximation technique, namely LMMSE by SWC, was evaluated. This was accomplished by applying the SWC technique to the LMMSE fixed weighting matrix. The LMMSE by SWC can reduce the computational complexity of the full LMMSE processor by more than 50% and it outperforms the LMMSE by SVD over a wide range of channel delay spreads and SNRs.

Both approximation techniques, LMMSE by SVD and LMMSE by SWC, produce an irreducible error floor at high SNRs. To overcome this limitation, a low complexity LMMSE channel estimation algorithm was developed in MISO OFDM. The low complexity algorithm reduces the LMMSE complex fixed weighting matrix to all real values. This was accomplished by approximating the power delay profile, generally exponential in wireless channels, as uniform followed by positioning the CIR symmetrically around the time origin using a cyclic shift. The novel algorithm reduces computational complexity of the optimal LMMSE processor (with exponential power delay profile) by 50% in terms of required multiplications. Despite this, the loss of estimation accuracy remains within 1 – 2 dB over a wide range of channel delay spreads and SNRs in a 2×1 diversity scheme.

Furthermore, temporal and frequency domain channel estimation methods were analysed in the thesis for OFDM-based WLANs in an indoor channel environment. It was shown that the temporal approach performs worse than the frequency domain approach, mainly because of two limiting factors. These are the leakage problem in non-sample spaced channels, which causes energy loss with the CIR windowing, and null-guard tones, often used in WLANs, which can lead to an accuracy loss in the CIR measurement when DFT processing is involved. The frequency domain

approach is inherently robust to these two effects, as the filtering of the initial channel estimation is solely performed in the frequency domain and the estimator operates on the subcarriers that are actually used in an OFDM system.

The combination of the real time LMMSE, low complexity LMMSE with a power delay profile approximated as uniform and SWC technique can significantly reduce the computational complexity of the full LMMSE processor (by more than 75% in a 2×1 diversity scheme). Despite this, the loss of accuracy remains within 1 – 2 dB over a wide range of channel delay spreads and SNRs.

8.2 Future Work

The MIMO channels are correlated, as it has been indicated in a number of recent research papers and reports [46], [95]-[101]. Although this is an obvious limiting factor for a MIMO capacity growth, these correlation properties can be exploited for further improvement of the channel estimation accuracy in OFDM using multiple antennas. This needs to be investigated and therefore more research work is required.

Channel estimation algorithms for coherent OFDM systems with training sequences are generally evaluated for pilot symbols that have identical OFDM parameters, such as the CP length and OFDM pilot symbol structure. Some practical constraints may impose a restriction to a number of used pilot symbols, forcing the use of a pilot symbol sequence with different OFDM parameters. Non-identical pilot symbol structures need to be further analysed and investigated in various multipath channel environments.

Also, in OFDM systems with a large number of subcarriers channel estimation algorithms can be evaluated using a cluster approach. What is an optimal OFDM cluster channel estimation methods, what is an optimal cluster size and what is an optimal OFDM parameter set itself in the cluster approach? These questions could also be addressed for a future work.

Bibliography

- [1] J.A.C. Bingham, “Multicarrier Modulation for Data Transmission: An Idea Whose Time Has Come”, *IEEE Commun. Mag.*, 28(5), pp. 5 – 14, 1990.
- [2] O. Edfors, M. Sandell, J.-J. van de Beek, D. Landström and F. Sjöberg, “An Introduction to Orthogonal Frequency-Division Multiplexing”, *Research Report TULEA*, Luleå University of Technology, Sweden, 1996.
- [3] M. Wahlqvist, C. Östberg, J.-J. van de Beek, O. Edfors and P.O. Börjesson, “A Conceptual Study of OFDM-based Multiple Access Schemes: Part 1 – Air Interface Requirements”, *Technical Report*, Luleå University of Technology, Sweden, 1996.
- [4] R. van Nee and R. Prasad, *OFDM for Wireless Multimedia Communications*, Artech House: USA, 2000.
- [5] L. Hanzo, W. Webb and T. Keller, *Single- and Multi-carrier Quadrature Amplitude Modulation: Principles and Applications for Personal Communications, WLANs and Broadcasting*, John Wiley & Sons: England, 2000.
- [6] H. Rohling, T. May, K. Brüninghaus and R. Grünheid, “Broad-Band OFDM Radio Transmission for Multimedia Applications”, *Proc. IEEE*, 87(10), pp. 1778 – 1789, 1999.
- [7] T. Keller and L. Hanzo, “Adaptive Multicarrier Modulation: A Convenient Framework for Time-Frequency Processing in Wireless Communications”, *Proc. IEEE*, 88(5), pp. 609 – 639, 2000.
- [8] J.G. Proakis, *Digital Communications*, 4th ed., McGraw-Hill Inc.: New York, 2001.

- [9] R.W. Chang, "Synthesis of Band-Limited Orthogonal Signals for Multichannel Data Transmission", *Bell Syst. Tech. J.*, 45, pp. 1775 – 1796, 1966.
- [10] S.B. Weinstein and P.M. Ebert, "Data Transmission by Frequency-Division Multiplexing Using the Discrete Fourier Transform", *IEEE Trans. Commun.*, COM-19(5), pp. 628 – 634, 1971.
- [11] A. Peled and A. Ruiz, "Frequency Domain Data Transmission Using Reduced Computational Complexity Algorithms", in *IEEE Int. Conf. on ICASSP*, 5, pp. 964 – 967, 1980.
- [12] http://standards.ieee.org/announcements/pr_p80211n.html
- [13] T.S. Rappaport, "*Wireless Communications: Principles & Practice*", Prentice Hall, Inc.: USA, 1999.
- [14] P. Hoeher, "A Statistical Discrete-Time Model for the WSSUS Multipath Channel", *IEEE Trans. Vehic. Technol.*, 41(4), pp. 461 – 468, 1992.
- [15] Y.G. Li, L.J. Cimini and N.R. Sollenberger, "Robust Channel Estimation for OFDM Systems with Rapid Dispersive Fading Channels", *IEEE Trans. Commun.*, 46(7), pp. 902 – 915, 1998.
- [16] Y.G. Li, N. Seshadri and S. Ariyavisitakul, "Channel Estimation for OFDM Systems with Transmitter Diversity in Mobile Wireless Channels", *IEEE J. Select. Areas Commun.*, 17(3), pp. 461 – 471, 1999.
- [17] J.-J. van de Beek, O. Edfors, M. Sandell, S.K. Wilson and P.O. Börjesson, "On Channel Estimation in OFDM Systems", in *Proc. IEEE VTC*, pp. 815 – 819, 1995.
- [18] C.W. Wong, C.L. Law and Y.L. Guan, "Channel Estimator for OFDM Systems with 2-Dimensional Filtering in the Transform Domain", in *Proc. IEEE VTC*, pp. 717 – 721, 2001.
- [19] H. Minn, D.I. Kim and V.K. Bhargava, "A Reduced Complexity Channel Estimation for OFDM Systems With Transmit Diversity in Mobile Wireless Channels", *IEEE Trans. Commun.*, 50(5), pp. 799 – 807, 2002.

- [20] I. Tolochko and M. Faulkner, "Channel Estimation Algorithm Analysis in Wireless LANs with Transmitter Diversity", in *Australian Telecommunications Networks and Applications Conference*, Melbourne, Australia, 2003.
- [21] E. Viterbo and K. Fazel, "How to Combat Long Echoes in OFDM Transmission Schemes: Sub-channel Equalization or More Powerful Channel Coding", in *Proc. IEEE GLOBECOM*, pp. 2069 – 2074, 1995.
- [22] P.J.W. Melsa, R.C. Younce and C.E. Rohrs, "Impulse Response Shortening for Discrete Multitone Transceivers", *IEEE Trans. Commun.*, 44(12), pp. 1662 – 1672, 1996.
- [23] J.L. Seoane, S.K. Wilson and S. Gelfand, "Analysis of Intertone and Interblock Interference in OFDM when the Length of the Cyclic Prefix is Shorter than the Length of the Impulse Response of the Channel", in *Proc. IEEE GLOBECOM*, pp. 32 – 36, 1997.
- [24] M. Faulkner, "The Effect of Filtering on the Performance of OFDM Systems", *IEEE Trans. Veh. Technol.*, 49(5), pp. 1877 – 1884, 2000.
- [25] S. Çelebi, "Interblock Interference (IBI) and Time of Reference (TOR) Computation in OFDM Systems", *IEEE Trans. Commun.*, 49(11), pp. 1895 – 1900, 2001.
- [26] R. Schur, "Impulse Compression for OFDM Transmission over Time-varying Multipath Channels", in *Proc. IEEE VTC*, pp. 1074 – 1076, 2002.
- [27] W. Henkel, G. Tauböck, P. Ödling, P.O. Börjesson and N. Petersson, "The Cyclic Prefix of OFDM/DMT – an Analysis", in *IEEE Seminar on Broadband Communications: Access, Transmission, Networking*, pp. 22-1 – 22-3, 2002.
- [28] I. Tolochko and M. Faulkner, "Channel Estimation in Wireless LANs with Transmitter Diversity", *J. Wireless Pers. Commun.*, 31(1-2), pp. 63 – 75, 2004.
- [29] S.G. Wilson, *Digital Modulation and Coding*, Prentice Hall, Inc.: USA, 1996.
- [30] M.C. Jeruchim, P. Balaban and K.S. Shanmugan, *Simulation of Communication Systems*, Plenum Press: USA, 1992.

- [31] R.F.H. Fischer, L.H.-J. Lampe and S.H. Müller-Weinfurtner, “Coded Modulation for Noncoherent Reception with Application to OFDM”, *IEEE Trans. Veh. Technol.*, 50(4), pp. 910 – 919, 2001.
- [32] H. Rohling and T. May, “OFDM Systems with Differential Modulation Schemes and Turbo Decoding Techniques”, in *Proc. IEEE on Broadband Communications*, pp. 251 – 255, 2000.
- [33] T. May and H. Rohling, “Turbo Decoding of Convolutional Codes in Differentially Modulated OFDM Transmission Systems”, in *Proc. 49th IEEE VTC*, pp. 1891 – 1895, 1999.
- [34] E. Haas and S. Kaiser, “Two-dimensional Differential Demodulation for OFDM”, *IEEE Trans. Commun.*, 51(4), pp. 580 – 586, 2003.
- [35] O. Edfors, M. Sandell, J.-J. van de Beek, S.K. Wilson and P.O. Börjesson, “Analysis of DFT-Based Channel Estimators for OFDM”, *J. Wireless Pers. Commun.*, 12(1), pp. 55 – 70, 2000.
- [36] ETSI Standard, “Radio Broadcasting Systems: Digital Audio Broadcasting to Mobile, Portable and Fixed Receivers”, European Telecommunication Standard, ETS 300–401, 1995.
- [37] ETSI Standard, “Digital Video Broadcasting: Framing Structure, Channel Coding, and Modulation for Digital Terrestrial Television”, European Telecommunication Standard, EN 300–744, 1997.
- [38] IEEE Std 802.11a/D7.0, “Part 11: Wireless LAN Medium Access Control (MAC) and Physical Layer (PHY) Specifications: High-Speed Physical Layer in the 5 GHz Band”, New York, USA, 1999.
- [39] Broadband Radio Access Networks (BRAN); HIPERLAN type 2; Physical (PHY) layer. TS 101 475 V1.1.1, ETSI – European Telecommunications Standards Institute, 2000.
- [40] A.J. Paulraj, D.A. Gore, R.U. Nabar and H. Bölcskei, “An Overview of MIMO Communications – A Key to Gigabit Wireless”, *Proc. of the IEEE*, 92(2), pp. 198 – 218, 2004.

- [41] A.D. Doufexi, S. Armour, M. Butler, A. Nix, D. Bull, J. McGeehan and P. Karlsson, “A Comparison of the HIPERLAN/2 and IEEE 802.11a Wireless LAN Standards”, *IEEE Comm. Mag.*, 40(5), pp. 172 – 180, 2002
- [42] R. van Nee, “A New OFDM Standard for High Rate Wireless LAN in the 5 GHz Band”, in *Proc. IEEE VTC*, pp. 258 – 262, 1999.
- [43] J. Khun-Jush, P. Schramm, G. Malmgren and J. Torsner, “HiperLAN2: Broad-band Wireless Communications at 5 GHz”, *IEEE Comm. Mag.*, 40(6), pp. 130 – 136, 2002.
- [44] J.-J. van de Beek, O. Edfors, P.O. Börjesson, M. Wahlqvist and C. Östberg, “A Conceptual Study of OFDM-based Multiple Access Schemes: Part 2 – Channel Estimation in the Uplink”, *Technical Report*, Luleå University of Technology, Sweden, 1996.
- [45] J. Medbo and P. Schramm, “Channel Models for HIPERLAN/2 in Different Indoor Scenarios”, ETSI BRAN doc. No. 3ER1085B, 1998.
- [46] V. Erceg et al, “IEEE P802.11 Wireless LANs: TGn Channel Models”, doc.: 802.11-03/940r1, 2003.
- [47] A.A.M. Saleh and R.A. Valenzuela, “A Statistical Model for Indoor Multipath Propagation”, *IEEE J. Select. Areas Commun.*, 5, pp. 128 – 137, 1987.
- [48] Q.H. Spencer, B.D. Jeffs, M.A. Jensen and A.L. Swindlehurst, “Modeling the Statistical Time and Angle of Arrival Characteristics of an Indoor Multipath Channel”, *IEEE J. Select. Areas Commun.*, 18(3), pp. 347 – 360, 2000.
- [49] G. German, Q. Spencer, L. Swindlehurst and R. Valenzuela, “Wireless Indoor Channel Modeling: Statistical Agreement of Ray Tracing Simulations and Channel Sounding Measurements”, in *Proc. IEEE ICASSP*, pp. 2501 – 2504, 2001.
- [50] Chia-Chin Chong, Chor-Min Tan, D.I. Laurenson, S. McLaughlin, M.A. Beach and A.R. Nix, “A New Statistical Wideband Spatio-Temporal Channel Model for 5-GHz Band WLAN Systems”, *IEEE J. Select. Areas Commun.*, 21(2), pp. 139 – 150, 2003.

- [51] A.S.Y. Poon and M. Ho, “Indoor Multiple-Antenna Channel Characterization from 2 to 8 GHz”, in *Proc. IEEE ICC*, pp. 3519 – 3523, 2003.
- [52] B. Sklar, “Rayleigh Fading Channels in Mobile Digital Communication Systems Part I: Characterization”, *IEEE Commun. Mag.*, 35(7), pp. 136 – 146, 1997.
- [53] B. Sklar, “Rayleigh Fading Channels in Mobile Digital Communication Systems Part II: Mitigation”, *IEEE Commun. Mag.*, 35(7), pp. 148 – 155, 1997.
- [54] H. Steendam and M. Moeneclaey, “Analysis and Optimization of the Performance of OFDM on Frequency-selective Time-selective Fading Channels”, *IEEE Trans. Commun.*, 47(12), pp. 1811 – 1819, 1999.
- [55] P. Hoeher, S. Kaiser and P. Robertson, “Two-Dimensional Pilot-Symbol-Aided Channel Estimation by Wiener Filtering”, in *Proc. IEEE ICASSP*, pp. 1845 – 1848, 1997.
- [56] H. Schober and F. Jondral, “Velocity Estimation for OFDM Based Communication Systems”, in *Proc. 56th IEEE VTC*, pp. 715 – 718, 2002.
- [57] O. Edfors, M. Sandell, J.-J. van de Beek, S.K. Wilson and P.O. Börjesson, “OFDM Channel Estimation by Singular Value Decomposition”, *IEEE Trans. Commun.*, 46(7), pp. 931 – 939, 1998.
- [58] I. Tolochko and M. Faulkner, “Real Time LMMSE Channel Estimation for Wireless OFDM Systems with Transmitter Diversity”, in *Proc. 56th IEEE VTC*, pp. 1555 – 1559, 2002.
- [59] G.J. Foschini, “Layered Space-Time Architecture for Wireless Communication in a Fading Environment When Using Multi-Element Antennas”, *AT&T Tech. J.*, 1, 1996.
- [60] V. Tarokh, N. Seshadri and A.R. Calderbank, “Space-Time Codes for High Data Rate Wireless Communication: Performance Criterion and code Construction”, *IEEE Trans. Inform. Theory*, 44(2), pp. 744 – 765, 1998.
- [61] A.F. Naguib, N. Seshadri and A.R. Calderbank, “Increasing data rate over wireless channels”, *IEEE Sign. Process. Mag.*, 17(3), pp. 76 – 92, 2000.

- [62] G.G. Raleigh and J.M. Cioffi, "Spatio-Temporal Coding for Wireless Communication", *IEEE Trans. Commun.*, 46(3), pp. 357 – 366, 1998.
- [63] L.J. Cimini, Jr., Babak Daneshrad and N.R. Sollenberger, "Clustered OFDM with Transmitter Diversity and Coding", in *Proc. IEEE GLOBECOM*, pp. 703 – 707, 1996.
- [64] Ye Li, J.C. Chuang and N.R. Sollenberger, "Transmitter Diversity for OFDM Systems and its Impact on High-Rate Data Wireless Networks", *IEEE J. Select. Areas Commun.*, 17(7), pp. 1233 – 1243, 1999.
- [65] A.J. Paulraj and C.B. Papadias, "Space-Time Processing for Wireless Communications", *IEEE Sign. Process. Mag.*, 14(6), pp. 49 – 83, 1997.
- [66] A.N. Mody and G.L. Stüber, "Parameter Estimation for OFDM with Transmit Receive Diversity", in *Proc. 53rd IEEE VTC*, pp. 820 – 824, 2001.
- [67] E.G. Larsson and J. Li, "Preamble Design for Multiple-Antenna OFDM-based WLANs with Null Subcarriers", *IEEE Signal Processing Lett.*, 8(11), pp. 285 – 288, 2001.
- [68] S.B. Slimane, "Channel Estimation for HIPERLAN/2 with Transmitter Diversity", in *Proc. IEEE ICC*, 1(28), pp. 26 – 30, 2002.
- [69] Wookwon Lee, "On Channel Estimation for OFDM Systems in Multipath Environments with Relatively Large Delay Spread", in *Proc. IEEE VTC*, pp. 1303 – 1307, 2003.
- [70] Young-Hwan You, Hyeok-Koo Jung, Won-Gi Jeon and Hyung-Rae Cho, "Impact of Imperfect Channel Estimation in OFDM-based Spatial Multiplexing Systems", *Electron. Lett.*, 38(24), pp. 1589 – 1591, 2002.
- [71] A. van Zelst and T.C.W. Schenk, "Implementation of a MIMO OFDM based Wireless LAN System", *IEEE Trans. on Signal Processing*, 52(2), pp. 483 – 494, 2004.

- [72] Won Gi Jeon, Kyung Hyun Paik and Yong Soo Cho, “An Efficient Channel Estimation Technique for OFDM Systems with Transmitter Diversity”, in *Proc. 11th IEEE PIMRC*, pp. 1246 – 1250, 2000.
- [73] N.C. Beaulieu, A.S. Toms and D.R. Pauluzzi, “Comparison of Four SNR Estimators for QPSK Modulations”, *IEEE Commun. Lett.*, 4(2), pp. 43 – 45, 2000.
- [74] D.R. Pauluzzi and N.C. Beaulieu, “A Comparison of SNR Estimation Techniques for the AWGN Channel”, *IEEE Trans. Commun.*, 48(10), pp. 1681 – 1691, 2000.
- [75] N.S. Alagha, “Cramer-Rao Bounds of SNR Estimates for BPSK and QPSK Modulated Signals”, *IEEE Commun. Lett.*, 5(1), pp. 10 – 12, 2001.
- [76] A. Wiesel, J. Goldberg and H. Messer, “Data-Aided Signal-to-Noise-Ratio Estimation in Time Selective Fading Channels”, in *Proc. IEEE ICASSP*, pp. III-2197 – III-2200, 2002.
- [77] C.H. Aldana, A.A. Salvekar, J. Tallado and J. Cioffi, “Accurate Noise Estimates in Multicarrier Systems”, in *Proc. 52nd IEEE VTC*, pp. 434 – 438, 2000.
- [78] I. Tolochko, M. Pereira and M. Faulkner, “SNR Estimation in Wireless LANs with Transmitter Diversity”, in the *3rd ATcrc Telecommunications and Networking Conference*, Melbourne, Australia, 2003.
- [79] S. He and M. Torkelson, “Effective SNR Estimation in OFDM System Simulation”, in *Proc. IEEE GLOBECOM*, pp. 945 – 950, 1998.
- [80] G. Strang, *Introduction to Linear Algebra*, Wellesley-Cambridge Press: USA, 1993.
- [81] P.A. Lynn and W. Fuerst, *Introductory Digital Signal Processing with Computer Applications*, John Wiley & Sons: USA, 1996.
- [82] I. Tolochko and M. Faulkner, “Low Complexity LMMSE Channel Estimation in OFDM Systems with Transmitter Diversity”, In preparation.

- [83] K. Ramasubramanian and K. Baum, “An OFDM Timing Recovery Scheme with Inherent Delay-Spread Estimation”, in *Proc. IEEE GLOBECOM*, pp. 3111 – 3115, 2001.
- [84] C.R.N. Athaudage and A.D.S. Jayalath, “Delay-Spread Estimation Using Cyclic-Prefix in Wireless OFDM Systems”, in *Proc. IEEE ICASSP*, pp. IV-668 – IV-671, 2003.
- [85] L.L. Scharf, *Statistical Signal Processing: Detection, Estimation, and Time Series Analysis*, Addison-Wesley, Inc.: USA, 1991.
- [86] S. Haykin, *Adaptive Filter Theory*, 3rd ed., Prentice-Hall: USA, 1996.
- [87] Y. Bar-Shalom and Xiao-Rong Li, *Estimation and Tracking: Principles, Techniques, and Software*, Artech House: USA, 1993.
- [88] E.C. Ifeachor and B.W. Jervis, *Digital Signal Processing: A Practical Approach*, 2nd ed., Prentice Hall: USA, 2002.
- [89] S.M. Alamouti, “A Simple Transmit Diversity Technique for Wireless Communications”, *IEEE J. Select. Areas Commun.*, 16(8), pp. 1451 – 1458, 1998.
- [90] O. Edfors, “Low-Complexity Algorithms in Digital Receivers”, Ph.D. thesis, Luleå University of Technology, Sweden, 1996.
- [91] A. Doufexi, S. Armour, M. Butler, A. Nix and D. Bull, “A Study of the Performance of HIPERLAN/2 and IEEE 802.11a Physical Layers”, in *Proc. IEEE VTC*, pp. 668 – 672, 2001.
- [92] S. Haykin, *Communication Systems*, 2nd ed., John Wiley & Sons: USA, 1983.
- [93] A. Croft, R. Davison and M. Hargreaves, *Engineering Mathematics: A Modern Foundation for Electronic, Electrical and Control Engineers*, Addison-Wesley: Great Britain, 1992.
- [94] A.V. Oppenheim and R.W. Schaffer, *Discrete-Time Signal Processing*, Prentice-Hall: Englewood Cliffs, NJ, 1989.

- [95] Da-Shan Shiu, G.J. Foschini, M.J. Gans and J.M. Kahn, “Fading Correlation and Its Effect on the Capacity of Multielement Antenna Systems”, *IEEE Trans. Commun.*, 48(3), pp. 502 – 513, 2000.
- [96] S.L. Loyka, “Channel Capacity of MIMO Architecture Using the Exponential Correlation Matrix”, *IEEE Commun. Lett.*, 5(9), pp. 369 – 371, 2001.
- [97] S. Loyka and G. Tsoulos, “Estimating MIMO System Performance Using the Correlation Matrix Approach”, *IEEE Commun. Lett.*, 6(1), pp. 19 – 21, 2002.
- [98] S. Loyka and A. Kouki, “On MIMO Channel Capacity, Correlations, and Keyholes: Analysis of Degenerate Channels”, *IEEE Trans. Commun.*, 50(12), pp. 1886 – 1888, 2002.
- [99] R.P. Torres, S. Loredó, L. Valle and M. Domingo, “An Accurate and Efficient Method Based on Ray-Tracing for the Prediction of Local Flat-Fading Statistics in Picocell Radio Channels”, *IEEE J. Select. Areas Commun.*, 19(2), pp. 170 – 178, 2001.
- [100] L. Schumacher and B. Dijkstra, “Description of a MATLAB Implementation of the Indoor MIMO WLAN Channel Model Proposed by the IEEE 802.11 TGn Channel Model Special Committee”, implementation note ver. 3.0, Dec. 2003.
- [101] D. Gesbert, M. Shafi, Da-shan Shiu; P.J. Smith and A. Naguib, “From Theory to Practice: An Overview of MIMO Space-Time Coded Wireless Systems”, *IEEE J. Select. Areas Commun.*, 21(3), pp. 281 – 302, 2003.
- [102] M. Goossens, F. Mittelbach and A. Samarin, *The LATEX Companion*, Addison-Wesley: USA, 2002.